The Abdus Salam
International Centre for Theoretical Physics

United Nations
Educational, Scientific
and Cultural Organization

International Atomic
Energy Agency

SMR/1758-1

"Workshop on Ion Beam Studies of Nanomaterials:
Synthesis, Modification and Characterization"

26 June - 1 July 2006

Potentialities of Ion Implantaton for the Synthesis & Modification of Metal Nanoclusters

P. Mazzoldi & G. Mattei

University of Pavia
Department of Physics
Padova, Italy

RIVISTA DEL NUOVO CIMENTO Vol. 28, N. 7 2005
DOI 10.1393/ncr/i2006-10005-5

Potentialities of ion implantation for the synthesis and modification of metal nanoclusters

P. Mazzoldi and G. Mattei(*)
Dipartimento di Fisica, Università di Pavia - via Marzolo 8, I-35131 Padova, Italy

(ricevuto il 22 Marzo 2006)

Summary. — This work reviews the basic features of ion implantation as a tool for synthesizing and manipulating nanostructured materials with particular emphasis to nanocomposites made by dielectric matrices embedding metallic nanoparticles. After a brief introduction on the physics of ion implantation, two operating modes of ion implantation will be presented: the first is related to the direct synthesis of nanoclusters as resulting from the precipitation of the supersaturated solid solution produced by the implanted ions; the second is related to the modification induced by the ion beam on already formed nanostructures and is therefore referred to as indirect synthesis. Throughout the paper also various possible technological applications of the different kind of nanoclusters (mono-elemental or bimetallic) obtained by both approaches are presented: examples are given in the field of nonlinear optics, nanophotonics, magnetism and gas sensing.

PACS 61.72.Ww – Ion implantation.
PACS 61.46.Df – Nanoparticles.
PACS 81.05.Pj – Glass composites.

2 1. A brief history of ion implantation
3 2. The basic physics of ion implantation
3 2˙1. Energy loss and stopping power
8 2˙2. Defects produced during implantation
9 2˙3. Simulating ion implantation
11 2˙4. Chemical and physical interaction: models for predicting the cluster formation
13 3. A survey on nanocluster-based glassy composited materials
16 4. Ion beam direct synthesis: monoatomic clusters
17 4˙1. Basic equations of clustering
17 4˙1.1. Nucleation
17 4˙1.2. Diffusion-limited growth
18 4˙1.3. Coarsening

(*) E-mail: giovanni.mattei@unipd.it

19 4·2. Linear absorption of embedded metal clusters: the Mie theory
21 4·3. Experimental
22 4·4. Au cluster growth during isochronal annealing
24 4·5. Clustering of Au atoms under correlated diffusion
25 4·6. Au nucleation as a function of the annealing time
29 4·7. Au implantation in polymers
32 5. Ion beam direct synthesis: bimetallic clusters
34 5·1. Au-Cu alloy
37 5·2. Au-Ag alloy
40 5·3. Nonlinear optical properties of Au-based alloys
44 5·4. Pd-Ag and Pd-Cu alloys
49 5·5. Co-Ni alloy
49 5·6. Ag-S core-shell system
50 5·7. Cu-Ni alloy
51 5·8. Co-Cu alloy
52 5·9. Conclusions
52 6. Ion beam processing
52 6·1. Ion-beam–induced cluster precipitation
55 6·2. Ion-beam–induced cluster modification
56 6·2.1. Au-Cu alloy clusters
60 6·2.2. Au-Ag alloy clusters
63 7. General conclusions

1. – A brief history of ion implantation

Ion implantation is nowadays a well-established technique to modify the near-surface region of a material by the introduction of energetic ions accelerated through a potential difference in the keV–MeV region. Its use is today widespread in different areas, spanning from the microelectronic industrial production to the synthesis of new materials to end up with academic and fundamental investigations on ion-solid interaction. In particular, the first experimental studies on this last topic trace back to the 1960s following the theoretical ones aimed at the calculation of the energy lost by the bombarding ions through elastic and inelastic processes. After that in the 1970s ion implantation became a standard in the microelectronic industry, for instance, to selectively dope semiconductors substrates in a non-thermal way, therefore avoiding all those by-products like diffusion of dopants which are detrimental for a proper operation of the devices. The required amount of dopants in the semiconductor industry is quite low being in the range of 10^{18}–10^{19} atoms/cm^3. On the other hand, much higher ion doses were required as soon as, in the 1980s, the interest in a more aggressive modification of the materials switched the focus of the research also on insulating or metallic substrates: the amount of ions to form alloys or extended new phases in the implanted substrate should be comparable with the atomic concentration of the host atoms (10^{21}–10^{22} atoms/cm^3, *i.e.* reaching the atomic percent). A prototypical example of this activity is for instance the modification of the surface of surgically implanted parts in the human body, so as to avoid possible delamination characteristic of surface coatings.

Beside modifying the composition of the materials, ion implantation has been also used to modify the mechanical properties of their near-surface region, such as their tribological behavior or their wettability.

Since its first developments, ion implantation showed besides great potentialities like patterning or selective areal doping of materials, also intrinsic limitations like the maximum thickness which can be modified or the simple planar geometry allowed to homogeneously modify the target. These prompted for an active development and research in the scientific community which led to new tools for materials modification. For instance, to overcome the obvious limitation of ion implantation to modify only simple geometries like planar surface, a new mode of implantation achieved by a pulsed plasma ion source was developed extending the range of applicability of ion implantation also to complex shapes. On the other side, hybrid deposition techniques were developed to reduce the drawback of the thickness involved, like ion beam assisted deposition (IBAD), which combined vapor deposition with ion implantation to growth and simultaneously dope the substrates without thickness limitations.

The aim of this review is to present the main features of ion implantation as a tool for modifying and enhancing in a very controlled way the surface-related properties of materials. Particular emphasis will be given to the most advanced applications of ion implantation in the emerging field of nanomaterials, for which some practical examples will be presented, keeping in mind that the huge amount of possible developments in the contemporary nanotechnological world make an exhaustive presentation of the topic a very demanding task. For this reason we will focus on a specific class of nanomaterials for which ion implantation revealed a very powerful tool for the synthesis and the modification of the materials [1-3]. In particular we will focus on the nucleation, growth and modification of nanoclusters inside dielectric matrices like silica or silica glasses with interesting aspects in photonics, magnetism and sensors.

2. – The basic physics of ion implantation

The passage of energetic charged particles in matter has attracted enormous theoretical and experimental research for almost a century. The ion beam applications involve either modifications /engineering of the material surface or its analysis and are correlated to the interactions of the energetic ions with the electrons or nuclei of the target material. The interaction processes occur on a time scale of picoseconds and length scales as low as nanometers. In the following, some of the basic physical concepts involved in ion implantation are briefly recalled.

2˙1. *Energy loss and stopping power*. – Energetic particles lose their energy as they traverse the medium, via two energy loss mechanisms:

- *nuclear energy loss*: it is due to the elastic collisions with the nuclei of the target atoms. It increases with higher mass projectile/substrate combinations and is the dominant energy loss mechanism at low energies.

- *Electronic energy loss*: it is due to the inelastic collisions with the electrons of target atoms. It involves excitation and ionization of target electrons and increases with increasing ion velocity (*i.e.* with higher energy and lower mass projectiles).

Therefore one can define a rate of energy loss inside the target as

$$\frac{\mathrm{d}E}{\mathrm{d}x} \equiv \left.\frac{\mathrm{d}E}{\mathrm{d}x}\right|_n + \left.\frac{\mathrm{d}E}{\mathrm{d}x}\right|_e , \tag{1}$$

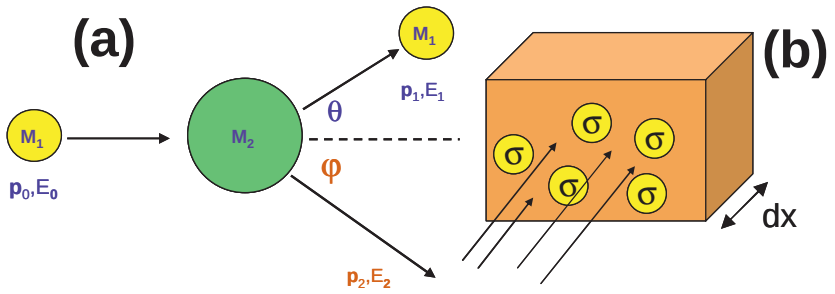

Fig. 1. – (a) Sketch of a binary collision between the incoming implanted ion of mass M_1 and the target atom of mass M_2. (b) Interaction between incoming ions and the scattering centers (represented by their interaction cross-section $\sigma(E)$) in a target volume of thickness dx.

where the subscripts n and e indicate *nuclear* and *electronic* energy loss, respectively. By normalizing the energy loss for the atomic target density N (atoms/cm^3), one obtains the stopping power S as the sum of the nuclear S_n and electronic S_e contributions:

$$S \equiv \frac{1}{N}\frac{\mathrm{d}E}{\mathrm{d}x} = S_n + S_e\,. \tag{2}$$

In the binary collision picture (see fig. 1(a)), the interaction between an incoming ion of mass M_1, atomic number Z_1, energy E_0 and momentum $\vec{p_0}$ and a target atom of mass M_2 and atomic number Z_2 at rest at distance r can be described by the scattering between two positively charged nuclei screened by the electronic clouds as

$$V(r) = k\frac{Z_1 Z_2 e^2}{r}\chi(r)\,, \tag{3}$$

where $\chi(r)$ is a screening function which reads

$$\chi(r) = \begin{cases} 0 & r \to \infty\,, \\ 1 & r \to 0\,. \end{cases} \tag{4}$$

The energy transferred during the interaction is T:

$$T = 4\frac{M_1 M_2}{(M_1+M_2)^2}E_0 \sin^2\frac{\theta}{2} = \gamma E_0 \sin^2\frac{\theta}{2}\,, \tag{5}$$

where θ is the scattering angle (fig. 1). Considering the nuclear interaction cross-section $\sigma(E)$ of the implanted ion with the target atom (see fig. 1(b)), one can write for the nuclear stopping power:

$$S_n(E) = \int_{T_{\min}}^{T_{\max}} T\frac{\mathrm{d}\sigma(E)}{\mathrm{d}T}\mathrm{d}T\,, \tag{6}$$

with $T_{\min} = E_d$, the displacement energy ([1]) and $T_{\max} = \gamma E$. A number of approximations exists for the cross-section derivative: one of the most used is based on the model of Ziegler, Biersack and Littmark (ZBL), which introduces three universal adimensional parameters $\lambda = 5.012$, $m = 0.203$ and $q = 0.413$ as

$$\frac{\mathrm{d}\sigma(E)}{\mathrm{d}T} = C\frac{f(t^{1/2})}{t^{3/2}}\,, \tag{7}$$

$$f(t^{1/2}) = \frac{\lambda t^{1/2-m}}{[1 + (2\lambda t^{1-m})^q]^{1/q}} \tag{8}$$

with $t = KE^2T$ an adimensional parameter and K a constant depending on the masses and atomic numbers of the colliding atoms.

Also for the electronic part, different theories have been developed: we quote the Lindhard-Scharff approximation which has two asymptotic forms as

$$S_e(E) = \begin{cases} C_L E^{1/2} & E \to 0, \\ C_H \frac{\ln E}{E} & E \to \infty, \end{cases} \tag{9}$$

with C_L and C_H two constants valid in the low- and high-energy regime, respectively. The two branches can be joined by the following expression:

$$S_e(E) = \left(\frac{1}{C_L E^{1/2}} + \frac{E}{C_H \ln E}\right)^{-1}. \tag{10}$$

In fig. 2 the nuclear and electronic part of the energy loss function is plotted for Au and He implantation in SiO_2: it is clear that for typical implantation energies of few hundreds of keV in the case of Au the nuclear component dominates over the electronic one, whereas in the He implantation the energy loss is practically completely due to electronic excitation. The relative contribution of the electronic S_e or nuclear S_n stopping power normalized to the total $S_{\mathrm{tot}} = S_e + S_n$ is shown in fig. 2c,d) for Au and He, respectively.

As the ion enters the target, it starts to lose energy via multiple collision with the target atoms, describing a path which is quite complicated. A useful quantity that

---

([1]) *Displacement Energy* E_d. The minimum energy required to knock a target atom far enough away from its lattice site so that it will not immediately return. This minimum energy produces a Frenkel Pair, *i.e.* a single vacancy and a nearby interstitial atom, which is the most fundamental type of damage caused by an ion. Typical values are about 20–50 eV. It is related to the *binding energy* (see below) and for crystalline targets it depends on the displacement direction in the lattice. Other special energies considered in ion implantation are: i) *Lattice Binding Energy* E_b. The minimum energy needed to remove an atom from a lattice site (proportional to the sublimation enthalpy ΔH_s). It takes energy to break electronic bonds and displace an atom from a lattice site. The lattice binding energy must be smaller than the displacement energy ($E_b < E_d$) with typical values of 3–10 eV; ii) *Surface Binding Energy* E_s. An atom at the target surface is not confined on one side, so the energy required to remove it from its lattice site is less than if it was inside the solid and surrounded by other atoms. A surface atom has fewer electronic bonds which must to broken. This energy is very important for sputtering (*i.e.* removal of surface atoms).

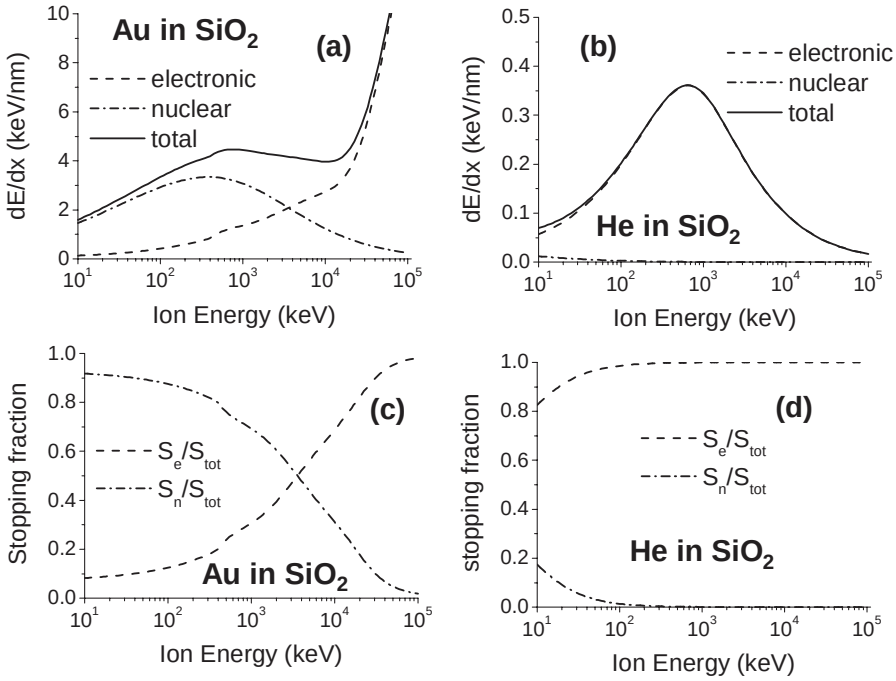

Fig. 2. – Electronic and nuclear energy loss function of (a) Au implanted in SiO_2 and (b) He implanted in SiO_2. The fraction of the electronic S_e or nuclear S_n stopping power with respect to the total ($S_{\rm tot} = S_e + S_n$) for Au (c) and He (d).

determines how deep in the substrate an ion with initial energy E_0 can penetrate before stopping is the range R defined as

$$R \equiv \int_{E_0}^{0} \left(\frac{\mathrm{d}E}{\mathrm{d}x}\right)^{-1} \mathrm{d}E\,, \tag{11}$$

or better its projected value, R_P, on the perpendicular to the sample surface as in fig. 3a.

The statistical distribution of the ions implanted can be described by a peak function, which can be roughly approximated by a Gaussian function centered at the average projected range R_P, with a half width ΔR_P called the straggling, as in fig. 3b, which shows a plot of the in-depth Au concentration profile for three different energies at constant fluence (called also dose, *i.e.* the integral of the concentration profile). In fig. 3c,d the range and straggling for Au and He implantation in SiO_2 are compared: it is clear that the range increases by decreasing the implanted ion mass or increasing the implantation energy. In general, the shape of the implanted profile depends strongly on the energy and on the couple ion/target, and significant deviation from Gaussian-like profile can be obtained.

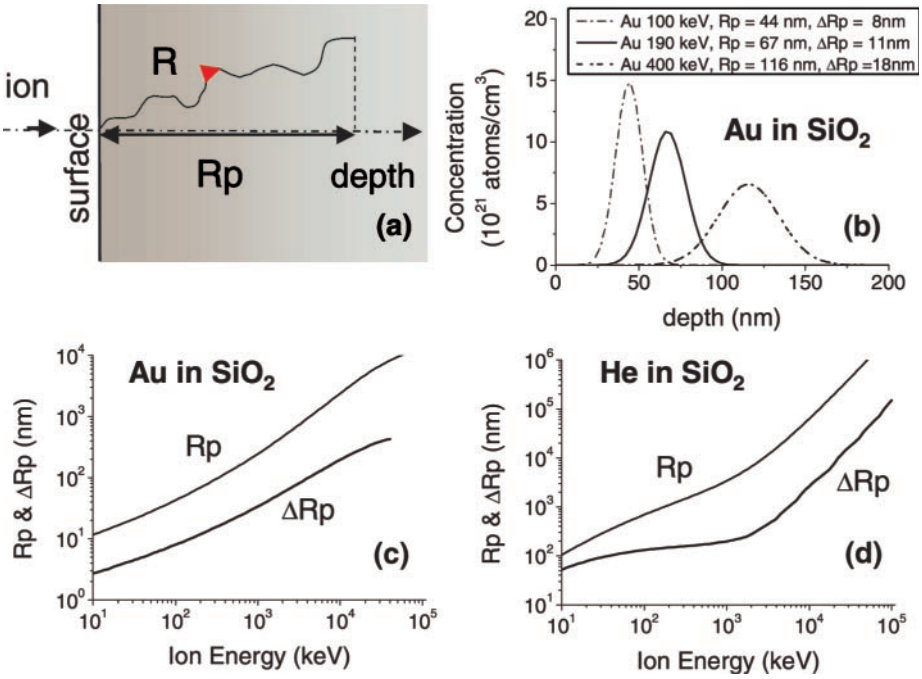

Fig. 3. – (a) Range R and projected range R_P along the implantation direction perpendicular to the sample surface. (b) In-depth Au concentration profile in silica for three different implantation energies (100 keV, 190 keV, 400 keV) at constant fluence. (c) Projected range R_P and straggling ΔR_P for Au implantation in SiO_2; (d) projected range R_P and straggling ΔR_P for He implantation in SiO_2.

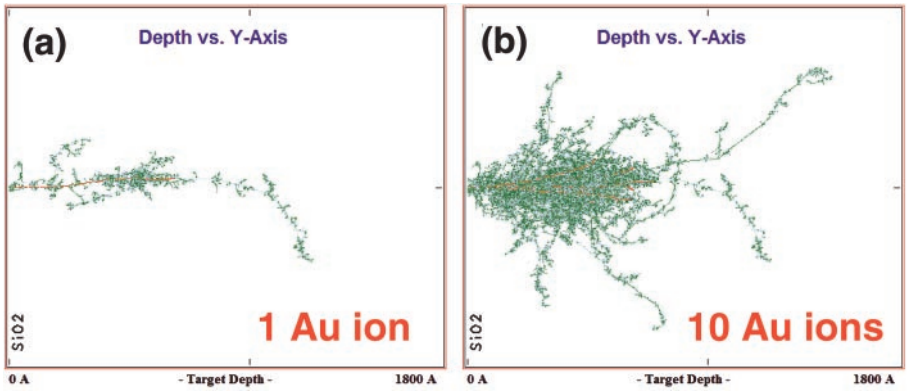

Fig. 4. – Monte Carlo simulated track of 1 Au ion (a) and 10 Au ions (b) implanted at 190 keV in SiO_2.

2˙2. *Defects produced during implantation.* – During the slowing down period, each ion will undergo multiple collisions, producing a trail of lattice atoms displaced([2]) from their equilibrium sites. The first target atom displaced by the incident ion is called the PKA, *i.e.* primary knock-on atom. The PKA starts the so-called collisional cascade in which the average number of target atoms displaced by a PKA of energy E is given by $\langle N_d(E)\rangle$, the displacement damage function.

In fig. 4 the Monte Carlo simulated track of 1 Au ion (a) and 10 Au ions (b) implanted at 190 keV in SiO_2 is shown: also the trajectories of the target displaced atoms in the collisional cascade are represented, indicating that the damage induced by the implanted ion extends well beyond its range.

In the frame of binary collision approximation the cascade and therefore the damage produced in the target can be described according to a stochastic redistribution of energy between colliding atoms triggered by the characteristic energies like displacement or binding energies as follows and by the kinematics of collision. Let Z_1, E and E_1 the atomic number and energies of the incoming atom before and after the collision with a target atom described by Z_2, displacement energy E_d, binding energy E_b and E_2, its energy after the collision. We can have different results or configurations according to the relative values of the energies considered and, in particular,

- if $E_2 > E_d$ a *displacement* occurs, *i.e.* the hit atom is given enough energy to leave the site.
- A *vacancy* occurs if both $E_1 > E_d$ and $E_2 > E_d$, *i.e.* both atoms have enough energy to leave the site, then becoming moving atoms of the cascade. The energy E_2 of atom Z_2 is reduced by the value E_b before it experienced another collision.
- If $E_1 > E_d$ but $E_2 < E_d$, then the struck atom does not have enough energy and it will vibrate back to its original site releasing E_2 as phonons, *i.e.* thermal energy which produces the target heating.
- If $E_1 < E_d$ and $E_2 > E_d$ and $Z_1 = Z_2$, then the incoming atom will remain at the site and the collision is called a *replacement collision* with E_1 released as phonons. The atom in the lattice site remains the same atom by exchange. This type of collision is common in single element targets with large recoil cascades.
- If $E_1 < E_d$ and $E_2 > E_d$ and $Z_1 \neq Z_2$, then Z_1 becomes a stopped interstitial atom.
- Finally, if $E_1 < E_d$ and $E_2 < E_d$, then Z_1 becomes an interstitial and $E_1 + E_2$ is released as phonons.

All these considerations can be generalized to poly-atomic targets: indeed, if the target has several different elements in it, and each has a different displacement and

([2]) For the sake of clarity we recall some basic definitions involved in the damage induced by implantation: i) *Displacement*: the process where an energetic incident atom knocks a lattice atom off its site; ii) *Vacancy*: a lattice site without an atoms. Originally all lattice sites are occupied, and displacements cause vacancies; iii) *Interstitial Atoms*: atoms which were knocked out of their original site, and come to a stop in the solid. Also the incident ions, when they stop, are considered interstitial atoms; iv) *Replacement Collisions*: atom sites with new atoms, identical to their original atom. This is a mechanism in which a vacancy may be re-occupied.

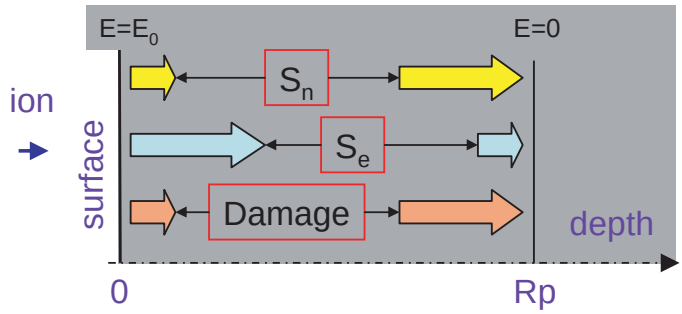

Fig. 5. – Relationship between implantation damage and the nuclear *vs.* electronic component of the stopping.

binding energy, then it is sufficient to consider a different value E_d and E_b for each atom of the cascade hitting different target atoms.

The elastic collisions produce either highly damaged lattices following implantation or a net of damaged structures whose density depends on lattice reordering (*i.e.* annealing) during the implantation process. In insulating materials, radiation damage is induced also in the electronic stopping power regime, due to the break of interatomic bonds. Various models like thermal spike model and Coulomb explosion model has been introduced in order to describe the phenomena in different materials. For a general review on this topic particularly focused on implantation in insulators see ref. [4].

Heavy ions dissipate energy through nuclear collisions. Damage occurs from the surface to where ions and the displaced target atoms stop. Light ions dissipate energy by electronic interactions, which cause a reduced damage, depending on the chemical properties of target material. Most of the damage occurs near the end of the trajectory where nuclear collisions dominate. In fig. 5 the damage distribution as a function of depth is schematically reported.

2˙3. *Simulating ion implantation.* – It is possible to simulate the kinetics of ion implantation by means of several computer codes: one of the most popular is SRIM ([3]) (*i.e.* Stopping and Range of Ions in Matter) [5]. It is a Monte Carlo calculation which follows the ion into the target, making detailed calculations of the energy transferred to every target atom collision. All the quantities like projected range, ion damage, target ionization and so on are simulated by averaging over a suitable number of ion trajectories: the higher the number the better the precision of the calculation. SRIM code traces back to the original work by J. P. Biersack on range algorithms (see J. P. Biersack and L. Haggmark, *Nucl. Instrum. and Methods*, Vol. **174** (1980) 257) and the work by J. F. Ziegler on stopping theory (see *The Stopping and Range of Ions in Matter*, Vol. **2-6** (Pergamon Press) 1977-1985). SRIM is able to simulate complex targets made of compound materials with also layered structures of different materials. It will calculate both the final 3D distribution of the ions and also all kinetic phenomena associated with the ion's energy loss: target damage, sputtering, ionization, and phonon production. All target atom cascades in the target are followed in detail. For instance the simulations in fig. 4 have been made with SRIM. This program is particularly suitable to simulate

([3]) available at the website `www.srim.org`

ion implantation in amorphous matrices as it does not take into account crystallographic direction which are required for simulating other technologically relevant implantation conditions like channelling in which ions are implanted along one high symmetry crystal direction so as the penetration depth of the ions is greatly increased due to the reduced scattering inside the crystal channels. One main limitation of SRIM calculation is that it does not take into account the accumulated damage, *i.e.* each simulated ion travels inside an undamaged target. This implies that phenomena like radiation enhanced diffusion (RED) which can play a role during high-dose ion implantation (like those for synthesizing nanoclusters in the present work) cannot be simulated. Other Monte Carlo codes which are able to a good level of approximation to follow the accumulated damage (*i.e.* to make a so-called *dynamical* calculation) have been developed, like for instance the TRIDYN [6] or DYNA codes [7, 8].

When setting up an actual ion implantation in a target, after choosing the ion and the target, the most important parameters which have to be optimized are

- *implantation energy*: it controls the penetration depth inside the target. Typical values are in the keV–MeV energy range.
- *Implantation dose* or *fluence*: it controls the amount of dopant (its local concentration) introduced in the target. It is measured in ions/cm^2 and it is the integral over the depth of the concentration profile. Typical values in the nanocluster synthesis are 10^{15}–10^{17} ions/cm^2.
- *Current density* or *flux*: is the number of ions introduced per unit time and unit surface area of the target. It is generally measured in μA/cm^2 and it affects the power density released to the target. Therefore, when dealing with insulating targets like glasses, the flux is of paramount importance to avoid (or to control) the sample heating during implantation. Typical fluxes used in high-fluence implantations are 0.1–10 μA/cm^2, taking into account that above 2–5 μA/cm^2 thermal heating in insulators should be considered.
- *Target temperature*: it can affect the dynamics of damage self-recovery or of the damage formation. Implantation at cryogen temperatures can be used to freeze the damage by reducing the diffusion of the atoms. On the other hand, by increasing the temperature, the amorphized regions of the target can be recrystallized or in the case of insulators, by implanting at high temperature (400–900 °C) the recovery of the network can be favored together with the diffusivity of the implanted species.

Among these four parameters, SRIM calculations obviously consider only the implantation energy, as the last three quantities deal with the dynamics of the damage, which is beyond the capabilities of the code.

By ion implantation, very large dopant concentration values can be obtained in the ion irradiated region, with a modification of chemical and physical material properties. A proper choice of implantation energies and fluencies allows the implanted ions to predetermine the composition, the depth and the spatial shape of the modified layer. A fundamental feature of ion implantation is that the implantation process is not a thermodynamic equilibrium process. Consequently the usual solubility limits of the implanted ions in the host can be largely overcome, achieving impurity local concentrations inaccessible by conventional synthesis routes. The ion distribution is controlled by the experimental parameters of the implantation process (energy, current, fluence), but also by the diffusion coefficients of the different species (implanted ions and displaced matrix

atoms), enhanced by the production of defects due to irradiation. The change of diffusion rates into the solid can favor either the aggregation of the dopant or their diffusion inside the target. Depending on the choice of the implanted atom and the dielectric target, implantation of "metal" ions in dielectric substrate gives rise to the formation of new compounds and/or metallic nanoparticles.

2˙4. *Chemical and physical interaction: models for predicting the cluster formation.* – The processes governing the chemical and physical interaction between the implanted ions and the host matrix atoms, very crucial for the final system configuration, are not completely understood in particular in terms of the relative roles of electronic and nuclear energy release [9]. Some models have been so far developed. Perez *et al.* [10, 11] first studied the state of implanted atoms using a simple statistical model and describing the role of a crystalline host matrix structure in the determination of the final compounds upon ion irradiation. Yet useful for getting a rough picture, Perez's statistical model is actually reliable only (and not always [12]) for ion implantation in crystalline substrates. Hosono [13] proposed a criterion to predict the formation of small clusters by ion implantation in SiO_2 glass, based on physical and chemical considerations. The main defects produced during ion implantation in silica are oxygen-deficient centers, namely, Si-Si homobonds and neutral oxygen monovacancies. The concentration of Si-Si bonds results highly ion-specific, *i.e.* critically depending on the chemical interaction among the implanted element and the silicon and oxygen atoms of the glass matrix. In the case of strong chemical interaction, implanted ions (M) tend to form M-O bonds, so leaving Si-Si bonds, whereas, for weak chemical interaction, a large part of the implanted atoms do not react with oxygen atoms, with a very low resulting concentration of Si-Si bonds. Implanted metal (M) and silicon ions compete for bonding oxygen, and cluster formation will occur when the chemical affinity of M ions for oxygen is smaller than that of Si^{4+}. Hosono model takes the free energy for the oxide formation as the quantity giving the measure of the chemical interaction. Clustering is expected to occur whenever the Gibbs free energy for an oxide formation with the implanted element M is greater than that for SiO_2. The chemistry considered here is the formation of the M_xO_2 oxide starting from the element M in the metallic form and the molecular gaseous oxygen, at the estimated effective temperature of $T = 3000$ K, as a consequence of the thermal spike phenomenon. A more general approach accounting for the different compounds observed to form in silica upon ion implantation is found in refs. [14, 15]. It starts from considering the concentration of the main implantation-induced defects in silica, pointing out the importance of the chemical interaction among implanted and host matrix atoms as a determining factor that gives rise to the observed defects. In particular, it is assumed that the primary factor controlling the chemical interaction of the implanted ions M with the matrix structure is the electronegativity (EN) of the implanted element. Three different categories are so defined, depending on the behavior of the element when implanted in fused silica. For elements with EN$<$ 2.5, the extraction of oxygen atoms from the silica network and the formation of M-O bond take place, while implants of elements for which EN$>$ 3.5 give rise to knock-on of oxygen atoms from the silica network, so forming Si-M bonds. The third kind of implants is that of noble metals, which do not exhibit significant chemical reactions.

Research Groups from Universities of Padova and Venice have proposed a model [16], originating from the investigation of Kelly [17] on the compositional modification induced by ion implantation on alloys, oxides and other substances. He first pointed out the important role of the chemistry in the ion-beam mixing process, even though, during

TABLE I. – *Comparison among the three models presented for predicting nanocluster synthesis and experimental results (⊗) for some metallic systems (in brackets the corresponding electronegativity): TS—two-step model* [16]*, HT—high-temperature thermodynamic model* [13]*; EN—electronegativity model* [14, 15].

Metal M	M-M bond	M-O bond	M-Si bond
Ag (1.9)	⊗ TS, HT, EN	-	-
Au (2.5)	⊗ TS, HT, EN	-	-
Co (1.9)	⊗ TS, HT	TS, EN	TS
Cr (1.7)	HT	⊗ TS, EN	⊗ TS
Cu (1.9)	⊗ TS, HT, EN	⊗ TS	-
Er (1.2)	-	⊗ TS, EN	-
Fe (1.8)	⊗ TS, HT	⊗ TS, EN	TS
In (1.8)	⊗ TS, HT	EN	-
Mn (1.5)	TS, HT	⊗ TS, EN	⊗ TS
Ni (1.9)	⊗ TS, HT	⊗ TS, EN	TS
Pd (2.2)	⊗ TS, HT	TS, EN	⊗ TS
Ti (1.5)	-	⊗ TS, EN	⊗ TS
Zn (1.6)	⊗ TS, HT	⊗ TS, EN	-

ion implantation, both the incoming ion energy (several keV) and the recoil energy of the atoms are very large compared to the chemical energies coming into play. Kelly introduced a new term in the ion-beam mixing diffusion equations, describing the effects of chemically guided steps along preferential trajectories. Some sort of chemical driving force, taking place at the end of the collisional cascades, could therefore significantly affect the ion-mixing process despite the energy disparity, with no need for a thermal spike picture.

After the first few tenths of a ps in the cascade (during which the temperature concept is meaningless), the effective local temperature is of the order of a few thousands K for a time interval of 10–20 ps, and at this level the self-diffusion coefficient is typical of a liquid state. On the other hand, after few tenths of a ns the local temperature becomes that of the substrate. Indeed, molecular dynamics simulations suggest that the described chemical (thermodynamical) processes should take place at the substrate temperature. So, the proposed model distinguishes two different steps in the ion implantation process. First, a high-energy ballistic regime takes place, giving rise to the substrate damage (defects, knock-on events, etc.). Second, low-energy, chemically-guided processes induce the formation of compounds that can be determined on the basis of thermodynamical considerations, by calculating the Gibbs energy variation for a chemical reaction between the implanted element (assumed in the gaseous form) and the silica molecule at the matrix temperature. The more negative this value results, the more likely is the formation of the particular compound. A comparison among the three models presented and some experimental results can be found in table I: the label HT, EN, and TS stands for the first high-temperature model [13], the subsequent model on electronegativity [14, 15] and the two-step model [16], respectively. The two-step model predicts correctly the formation of various compounds and the formation of metallic clusters at room temperature, yet failing in the prediction of silicide formation in the case of Fe, Co and Ni implants, that have significant magnetic behavior [16]. Generally speaking, exact calculations are anyhow possible only for stoichiometric silica, even if qualitative considerations can be

put forward as well. Indeed, thermodynamical concepts are limited by the uncertainty on the evaluation of the local temperature, as well as on the assumption that chemical interactions take place between the implanted atoms and the substrate compounds (not the separate atomic species). The possibility of such modelization for the cluster formation upon ion implantation is further complicated when dealing with sequential double implantation of two different elements.

The ion beam applications involving material analysis require that the ions lose their energy predominantly by colliding with the electrons of the solid so that the lattice is not disturbed (low mass ions and high energy). On the other hand, the applications involving engineering of materials require either displacements of atoms (nuclear energy loss) from the lattice sites or a large amount of energy deposited in the electronic system which later is coupled to the lattice via phonon generation. The advent of microstructured and nanostructured materials has extended the potential applications of ion implantation that are attractive because of the comparable dimensions length scales of component dimensions and the penetration distances associated with implantation.

3. – A survey on nanocluster-based glassy composited materials

Metal nanoclusters (NCs) embedded in insulating matrices have received in the last decade an increasing interest due to their peculiar optical, magnetic and catalytic properties when the size becomes comparable to or less than the electronic mean free path [3, 18, 2, 19, 20, 16, 21-25].

In nanophotonics, nanometer-sized metal clusters embedded in glass matrices exhibit striking nonlinear optical effects, particularly interesting for application in the field of nonlinear integrated optics, as part of all-optical devices. Recently, also sensitizing effects for rare-earth ions luminescence have been reported as due to energy transfer between metallic nanoclusters and Er or Eu ions in silica glass [26]. Moreover, nanoclusters dispersed in dielectric matrices may exhibit superparamagnetic properties, enhanced coercivity, shift of the hysteresis loop and large magnetotransport properties [27]. Nanostructured materials are also used in catalysis, where high surface-to-volume ratios are required [28].

Glass-based composites are in general expected to play an important role as materials for various nanotechnology applications, due to the low cost, ease of processing, high durability, resistance and high transparency, with the possibility of tailoring the behavior of the glass-based structures. M. Faraday made the first attempt to explain the nature of the color induced in glasses by small metal precipitates [29]. Further attempts to describe the optical behaviour of clusters embedded in a matrix as a homogeneous medium with an effective dielectric function were made by Maxwell-Garnett [30, 31]. A complete analytical solution to the scattering of an electromagnetic wave by a spherical isolated cluster embedded in a non-absorbing medium was given in the same years by G. Mie [32]. After that, many studies have been dedicated to the properties of Metal Nanocluster Composite Glass (MNCG). In general, the physical properties of these systems change dramatically in the transition from atom to molecule to cluster to solid, where the cluster regime is characterized by the confinement effects that make MNCGs peculiarly interesting. For example, experiments which showed the transition from atomic over molecular to bulk plasmon absorption features have been performed with Ag clusters in photosensitive glasses during the last four decades. Updated review articles dealing with MNGCs are currently published, each one covering one or more particular aspects, ranging from preparation techniques to properties and characterization. A general treatment of quantum dot materials including MNCGs is presented in ref. [33], while glasses for

optoelectronic devices, particularly MNCGs, are treated in refs. [3, 34, 35]. The theoretical aspects of MNCG properties are approached in the literature under a great variety of viewpoints, for example, by treating the electronic properties of metal clusters [36], or focusing on the quantum size effect [37]. Nonlinear optical properties of small metal particles are treated in details in refs. [38,39], while refs. [40,41] present extended reviews on theoretical and experimental aspects of the optical response of metal clusters. Recent aspects concerning the interface properties of MNCGs are in ref. [42], and ref. [43] presents a review of all-optical switching via nonlinear optical materials. The present work deals with metal nanocluster composites formed by clusters of binary transition metals alloy embedded in silicate glasses, in which cluster concentration is below the percolation limit (dispersed clusters). The scale regime has characteristic lengths, such as correlation lengths among clusters or electron mean free paths of the bulk, that are larger than the cluster size. On the other hand, the clusters are considered to be large enough to exhibit however electronic behavior features of the metal (usually, larger than 1 nm diameter), even being small enough to exhibit strong confinement effects (up to tens of nm diameter).

Ion implantation of metal or semiconductor ions into glass has been explored since the last decade as a useful technique to produce nanocomposite materials in which nanometer sized metal or semiconductor particles are embedded in dielectric matrices [16,3,25,20,44-47]. Furthermore, ion implantation has been used as the first step of combined methodologies that involve other treatments such as thermal annealing in controlled atmosphere, laser or ion irradiation [48,24,49]. In general, ion implantation is well established as a suitable technique for improve mechanical, optical and structural near-surface properties of glasses. It has several advantages, such as low-temperature processing, control of distribution and concentration of dopants, availability of chemical states which cannot be realized via conventional techniques, overcoming of solubility limits. Moreover, ion implantation can be exploited for designing waveguiding structures along prescribed patterns. The implantation of ions (of typical energies in the range from keV to MeV) into materials results in various modifications which depend on the glass composition, the ion species, the fluence, the implantation energy, and, in some cases, the interaction with the external atmosphere, when implanted glasses are removed from the implantation chamber. These modifications are here treated in the case of dielectric matrices, mostly fused silica and soda-lime glass, both of which are used for the synthesis of quantum dot materials, with interesting technological applications. Energetic ions loose their energy in implanted dielectrics by either interaction with the electronic system or by direct hard-sphere collisions with the nuclei. The partition of the ion energy into electronic and collisional processes, as well as the projected ion range and the straggling, are usually obtained by the SRIM code [5]. Both nuclear and electronic stopping give rise to structural changes in materials, and in several cases the process of ion implantation gives rise to the clusterization of implanted metal ions (for comprehensive reviews, see refs. [1, 16, 3, 20]).

The preparation of "mixed" colloidal structures, containing clusters of either different metals or formed by metal alloys, has recently attracted a great attention. With respect to the monoelemental case, binary metal nanoclusters offer further degrees of freedom for the control of the material features, namely, cluster composition and crystal structure. On the other hand, the suitability of MNCGs containing binary nanoclusters for actual devices requires a more detailed knowledge of the conditions for clusterization occurring, in order to control the parameters that may induce separation instead of alloying of the implanted species.

Sequential ion implantation of two different metal species may give rise to various different nanocluster structures, with the presence of separated families of pure metal

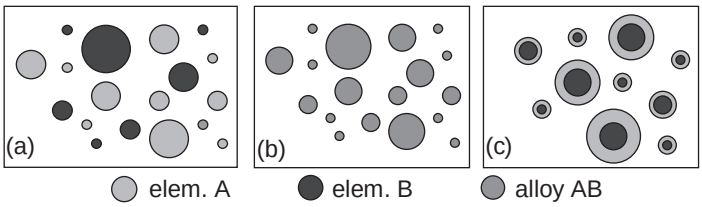

Fig. 6. – Sketch of possible families of clusters formed by sequential ion implantation of two different species A and B: separate A and B clusters (a), A-B alloy (b), and core-shell clusters (c).

clusters, crystalline alloy clusters, or core-shell structures (see fig. 6). Composition of the clusters can be varied by implanting sequentially in the matrix the two different elements at energies and doses such as to maximize the overlap between the implanted species, to control their local relative concentration. The formation of clusters of a certain nature depends critically on the implantation parameters such as ion fluence and energy, implants sequence and the temperature at which the process is realized. Moreover, post-implantation treatments such as annealing in controlled atmosphere and/or ion or laser irradiation have demonstrated to be effective in driving the system towards different stable clusters structures [49, 24]. An effective phenomenological model describing the formation of binary clusters is anyhow still lacking. Miscibility of the implanted elements comes into play together with the chemical reactivity with the matrix and the presence of radiation-induced defects in the definition of the resulting structure, and sistematic experimental data are presently available only for few cases, as discussed in the following. Multicomponent nanoclusters of Ag+Cu, In+Cu, In+Ag, Ag+Sb and Cd+Ag were first claimed to form (although in some cases not so unambiguously) by sequential implantation in silica [22, 50-52]. More recently, Cu+Ni, Ag+Ni, Au+Cu, Au+Ag, Cu+Ag systems have been studied for their optical properties, and the formation of alloy nanoclusters was unambiguously observed for the Cu+Ni, Au+Cu and Au+Ag systems [53,54,24]. In these cases, the interest is focused on both the third-order optical nonlinearity of the composites [55, 56] and the optical absorption response in terms of tunability of the plasma resonance [24]. Furthermore, Cu+Co, Co+Ni, Co+Fe, Pt+Fe, Fe+Al implanted glass nanocomposites were studied for their peculiar magnetic features [57-59]. The possibility to synthesize alloy based composites permits to tailor the magnetic properties of these nanostructured materials. For example, preliminary results have been recently obtained [60] for sequential ion implantation of Cu^+ and Co^+ in silica at different dose values. Indeed, this pair of elements is particularly interesting for the possibility to obtain CoCu alloy nanoclusters, despite their immiscibility in the bulk phase. Pd+Ag and Pd+Cu have been also studied for their properties in the field of catalysis [61]. It is worth remarking that sequential ion implantation is currently studied also for the formation of semiconductor binary systems in dielectrics. For example, the bandgap tunability of semiconductor nanoclusters draws the study of Ga+N, As+Ga, In+P, Cd-S, Cd-Se, Cd-Te, Ga-P In-As, Pb-S, Zn-Te, Zn+Se, Ag+S, Zn+S couples [62-64, 47].

In the following, we will focus the discussion on how to use ion implantation to produce nanoclusters (either mono- or bi-elemental) inside a silica glass host. Within the very general category of ion-beam–induced modification of materials or ion beam processing, three main approaches will be presented: i) ion beam direct synthesis; ii) ion beam

indirect synthesis; iii) ion beam modification. This nomenclature is somehow arbitrary because strictly speaking the three categories can all be defined "ion beam processing". To be more precise, therefore, we will adopt the following definitions:

– *ion beam direct synthesis*: the direct synthesis of mono- or bi-elemental nanoclusters by single or sequential ion implantation of the ions constituting the clusters inside the host matrix. This is the most intuitive approach and generally it can be coupled to suitable post-implantation thermal annealing of the samples in controlled atmosphere. In this approach ion beam is used to create a supersaturated solid solution of the implanted ions inside the matrix. The solution, either during implantation itself or after thermal treatments, starts to nucleate and well-defined nanoclusters can be obtained.

– *Ion beam indirect synthesis*: the ion beam in this case is used to tailor the energy deposited in the target (nuclear *vs.* electronic, in-depth distribution, etc.) so as to promote nucleation of clusters made of atoms already present in the host matrix. This synthesis route is somehow hybrid in the sense that it is normally coupled to a previous step involving doping of the matrix host by auxiliary techniques like for instance ion-exchange.

– *Ion beam modification*: the energy released by the implanted ions is used to modify already formed clusters by changing their size, shape, composition and topology. In particular we will see that this last mode can be conveniently applied to modify the electromagnetic environment around a nanocluster by the formation of peculiar cluster-satellite topology or to promote a selective de-alloying in bimetallic nanoclusters.

4. – Ion beam direct synthesis: monoatomic clusters

The most obvious way to synthesize nanoclusters inside a matrix is to implant ions M at a concentration which is above the solubility limit of M in the host to promote precipitation of a new phase from a supersaturated solid solution. We refer to this process as to "ion beam direct synthesis". To this respect, ion implantation is a very efficient technique as it can introduce any desired amount of the foreign phase in the host, without thermodynamic limitations typical of other synthesis techniques: we stress that this is due to the fact the ion implantation is a non-equilibrium technique.

The control of cluster size with dimensions in the nanometer range either during the synthesis process or after subsequent thermal annealing is one of the challenging issues of nanocluster technology, as the electronic properties of the nanoparticles depend strongly on their dimensions. In fact, ion implantation is usually coupled to post-implantation thermal treatments which have a twofold meaning: i) annealing of the implantation-induced defects; ii) growth of the nucleated embryos by means of suitable combination of annealing atmosphere, temperature and time. In silica, for instance, annealing of the implantation damage requires temperature near or above 600 °C: at these temperatures the thermal diffusion of the implanted species can be quite effective in modifying the post-implantation dopant distribution promoting either redistribution of implanted species or clustering around nucleated embryos. Therefore a precise understanding of the microscopic mechanisms influencing the evolution of cluster size during thermal annealing is of paramount importance [9, 65, 66].

We investigate this crucial problem by presenting a systematic study of the kinetics of gold atom clustering during annealing of gold implanted silica. The use of gold is due to its reduced chemical interaction with the elements constituting the matrix, therefore allowing to focus just on the clustering and growth phenomena, without possible interferences due to formation of bonds with Si or O atoms of the matrix. Moreover, gold has a low diffusivity [67] in comparison to other noble metals like silver for example: this minimizes the role of diffusion controlled processes, which occur in post implantation thermal annealings and, consequently, one has the possibility to vary the size and density nanoparticle distribution by means of the atmosphere in which post implantation annealings take place.

4˙1. *Basic equations of clustering.* – The precipitation processes that occur during either implantation or annealing of ion-implanted materials may be schematically divided in three steps not necessarily strictly separated: i) nucleation, ii) non-competitive or diffusion-limited growth, iii) competitive growth (*i.e.* coarsening or Ostwald ripening) regime.

Impurity implantation at fluences exceeding the solubility threshold in the matrix [68, 69] (fluences $\geq 10^{16}$ Au^+/cm^2 in the case of gold in silica, in our experimental conditions) results, in the first stage of the precipitation process, in a system of new phase precipitates, *i.e.* gold particles with radius exceeding the critical one, R_c. It is natural to assume that the radiation-induced defects, both point and extended defects, may act as nucleating centers in implanted materials and that heterogeneous nucleation takes place [68].

4˙1.1. Nucleation. Assuming the embryos as spherical particles of radius R the variation of the Gibbs $\Delta G(R)$ free energy can be written as

$$\Delta G(R) = -\frac{4\pi}{3} R^3 \Delta g_V + 4\pi R^2 \sigma \tag{12}$$

with Δg_V and σ are the bulk free energy per unit volume and the surface energy. The maximum of $\Delta G(R)$ with respect to the radius defines the critical radius R_c as

$$R_c = \frac{2\sigma}{\Delta g_V}\,. \tag{13}$$

During the initial stage of annealing, the particles (already formed after implantation) with radius exceeding the critical one, grow directly by solute depletion of the surrounding matrix, without competing with the growth of any others.

4˙1.2. Diffusion-limited growth. To analyze the evolution of cluster growth in our experimental conditions, we briefly recall here the basic equations governing the clustering process in supersaturated solid solutions. The problem of diffusive decomposition of supersaturated solid solutions was addressed by a number of authors [70-72]. They generally agree on the point that analytical solutions of a given diffusion-controlled phase transformation problem are not easily obtainable. However, approximate analytical solutions are reported in literature for the relevant quantities of the precipitation process that is mainly characterized by the growth of spherical or planar precipitates. In the case of spherical precipitates, the analytical expression for $R(t)$, the radius of the precipitates

at time t is

$$R^2(t) = R_0^2 + 2\frac{C_s - C_e}{C_p - C_e} Dt\,, \tag{14}$$

where R_0 is the value of R at $t = 0$ (which accounts for the radius of the already formed precipitates by implantation). The volume diffusion coefficient D of the dopant in the matrix is assumed independent of composition. C_p is the concentration of the solute in the precipitates and C_s and C_e are the concentration in the matrix just before the growth, and the equilibrium concentration in the matrix, respectively. The difference $C_s - C_e$ defines the degree of supersaturation that decreases during the precipitation stage.

Equation (14) stems from the solute flux balance at cluster-matrix interface:

$$C_p \frac{\mathrm{d}R}{\mathrm{d}t} = D \left.\frac{\partial C}{\partial r}\right|_{r=R} + C_e \frac{\mathrm{d}R}{\mathrm{d}t}\,. \tag{15}$$

Here, $C = C(r,t)$ is the concentration field in the matrix surrounding the precipitate, where the concentration gradient is linearized. Indeed, to obtain eq. (14) starting from eq. (15), a linearized gradient approximation must be adopted and "interaction" between growing grains must be disregarded as far as the grain size is small in comparison with the intergranular spacing [70]. In the following, we will apply eq. (14) to describe the experimental results obtained in the early stage of cluster growth. Moreover in eq. (14) we will assume that the C_e value is a vanishing quantity in comparison with C_s. In fact, the former corresponds to the equilibrium Au concentration in the SiO_2 matrix (*i.e.* the threshold for spontaneous precipitation), that is one order of magnitude less than C_s, as observed in our experiments.

4˙1.3. Coarsening. In the later stage, when the cluster size is fairly large and the supersaturation degree becomes extremely small, coarsening, *i.e.* Ostwald ripening, takes place. In this process, the particle transfer from the matrix to the cluster is controlled by the Gibbs-Thomson effect. For a spherical isotropic cluster of radius R the Gibbs-Thomson relation is

$$C(R) = C_\infty \exp\left[\frac{2\sigma V_a}{RkT}\right] \simeq C_\infty\Big(1 + \frac{\alpha}{R}\Big)\,, \tag{16}$$

where C_∞ is the equilibrium solute concentration at planar interface, α is the capillarity length associated to the surface tension σ and V_a the atomic volume [73]. We identify the concentration $C(R)$ with the equilibrium concentration in the immediate vicinity of the cluster of radius R in the matrix. The cluster size distribution determines an equilibrium concentration $C(\bar{R})$, where $\bar{R}$ is the mean value of the cluster radius distribution. Since smaller clusters have a higher solute concentration than larger ones, the diffusional balance promotes matter transfer from smaller to larger precipitates, *i.e.* Ostwald ripening. Consequently the $\bar{R}$ value increases and the diffusional process maintains the matter transfer. The equation governing the cluster growth is

$$\frac{\mathrm{d}}{\mathrm{d}t}\left(\frac{4}{3}\pi R^3\right) = 4\pi R^2 V_a(-D) \left.\frac{\partial C}{\partial r}\right|_{r=R} \tag{17}$$

whose integration, performed by Lifshitz and Slezof in the linearized gradient approximation [70], leads to

$$R^3(t) - R_0^3 = \frac{8}{9}\frac{\sigma V_a^2 C_\infty}{kT} Dt\,. \tag{18}$$

Therefore the solution (18) holds in the later stage of the precipitation process when size effects become relevant in connection to the $C(R)$ values [73].

In conclusion, we distinguish two different kinetic regimes of cluster growth: i) a diffusional one (occurring at the earlier stage of growth) which is characterized by a time dependence of cluster radius scaling as $(Dt)^{1/2}$, where D is the diffusion coefficient and t the diffusion time; ii) a coarsening regime (occurring at longer annealing times) with a radius scaling as $(Dt)^{1/3}$.

Before concluding this subsection, it is worth mentioning that in ion implantation-induced nucleation the diffusion coefficient D in the previous equations is not simply the purely thermal one: indeed, other effects contribute to D, *i.e.* the radiation enhanced diffusion (RED) and a correlated diffusion triggered by the correlation of dopant with the diffusing atoms coming from the annealing atmosphere, as envisaged in ref. [68].

However, disregarding the complicate form of the flux equations which include correlation processes or the microscopic mechanism of RED, one can account for all these effects by empirically introducing an *effective* diffusion coefficient, in the equations for precipitation and coarsening. Note that, when we will evaluate the surface tension σ, the diffusion parameter D does not enter in the calculation and so, the result is not affected by the choice of D.

4˙2. *Linear absorption of embedded metal clusters: the Mie theory.* – One of the fingerprints of noble-metal cluster formation is the development of a well-defined absorption band in the visible or near UV spectrum which is called the surface plasma resonance (SPR) absorption. It is typical of s-type metals like noble and alkali metals and it is due to a collective excitation of the delocalized conduction electrons confined within the cluster volume [40]. To better understand the meaning of the SPR absorption for spherical clusters we recall that, according to the theory developed by G. Mie in 1908 [32], the extinction cross-section $\sigma(\omega, R)$ due to non-interacting nanoparticles of radius R embedded in a non-absorbing medium with dielectric constant ε_m (*i.e.* with a refractive index $n = \sqrt{\varepsilon_m}$) can be written in the dipolar approximation as

$$\sigma(\omega, R) = 9\frac{\omega}{c}\varepsilon_m^{3/2} V_0 \frac{\varepsilon_2(\omega, R)}{(\varepsilon_1(\omega, R) + 2\varepsilon_m)^2 + \varepsilon_2^2(\omega, R)}\,, \tag{19}$$

where V_0 is the cluster volume, c is the speed of light in vacuum and $\varepsilon(\omega, R) \equiv \varepsilon_1(\omega, R) + i\varepsilon_2(\omega, R)$ is the size-dependent complex dielectric function of the cluster. The SPR absorption resonance holds when the denominator in eq. (19) is vanishingly small. This approximation is valid for isolated clusters when the radius is much less than the wavelength $\lambda = c(2\pi/\omega)$: when this is not the case retardation effects inside the cluster make the electrons oscillate not all with the same phase of the local field and high-order multipolar expansion should be taken into account in the general Mie formula [40]. One relevant point concerns the size dependence of the cluster dielectric function. Following ref. [40], the size correction is obtained by modifying the Drude-like part due to

delocalized free s-electrons introducing a size-dependent damping frequency $\Gamma(R)$ which accounts for the increased scattering at the cluster surface as follows:

$$\Gamma(R) = \Gamma_\infty + A\frac{v_F}{R}\,, \tag{20}$$

where Γ_∞ is the bulk damping frequency, v_F is the bulk Fermi velocity and A a geometrical adimensional constant usually assumed to be 1.

Considering a matrix with N clusters in the volume V, the absorption coefficient α of the composite is defined through the Lambert-Beer absorption law: $I = I_0 e^{-\alpha x}$, where I_0, I are the intensity before and after the sample of thickness x. Let $f(R)$ be the normalized cluster size distribution function with

$$\int_0^\infty \mathrm{d}R\, f(R) = 1\,; \tag{21}$$

the absorption coefficient $\alpha(\omega)$ can be written as

$$\alpha(\omega) = \frac{N}{V}\int_0^\infty \mathrm{d}R\, f(R)\,\sigma(\omega, R)\,. \tag{22}$$

In the case of monodisperse distribution (*i.e.* $f(R) = \delta(R - R_0)$) all the clusters have the same radius R_0, then

$$\alpha(\omega) = \frac{N}{V}\sigma(\omega, R_0) = \frac{NV_0}{V}\frac{\sigma(\omega, R_0)}{V_0} = p\frac{\sigma(\omega, R_0)}{V_0}\,. \tag{23}$$

With p the nanocluster filling factor. Therefore, if we measure the optical density $OD(\omega)$ defined as

$$OD(\omega) = \log_{10}\left(\frac{I_0}{I}\right) = \log_{10}(e)\,\alpha(\omega)\,x\,, \tag{24}$$

we have

$$OD(\omega) = \log_{10}(e)\,x\,\frac{N}{V}\int_0^\infty \mathrm{d}R\, f(R)\,\sigma(\omega, R)\,. \tag{25}$$

The above formalism has been applied to the calculation of the size distribution of Au clusters upon thermal annealing to complement the transmission electron microscopy analysis, as will be shown later.

To better illustrate the main factors influencing the position and the shape of the SPR absorption band, in fig. 7a) the effect of the cluster radius is shown for Ag nanoclusters in silica: when the size is no longer negligible with respect to the wavelength there is a red-shift of the SPR position with the appearance of multipolar peaks in the UV-blue region. The effect of the matrix for a fixed cluster size is described for $R = 2.5$ nm Au clusters in fig. 7b): the higher the matrix dielectric constant the more red-shifted is the SPR. Finally, the effect of the composition is shown in fig. 7c) for $R = 5$ nm clusters of Ag, Au and Cu in silica.

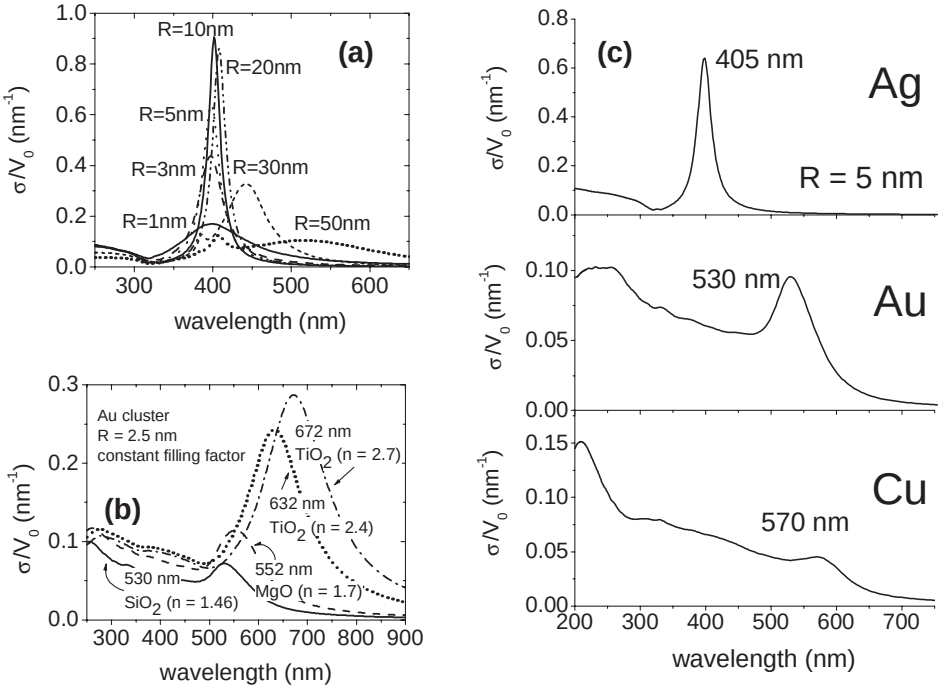

Fig. 7. – Absorption spectra of spherical non-interacting nanoclusters embedded in non-absorbing matrices: (a) effect of the size for Ag nanoclusters in silica; (b) effect of the matrix for $R = 2.5$ nm Au clusters (the refractive index $n = \sqrt{\varepsilon_m}$ and the position of the plasma resonance are reported for each considered matrix); (c) effect of the cluster composition for $R = 5$ nm noble-metal clusters (Ag, Au, Cu) in silica.

4˙3. *Experimental*. – The samples used for this study are fused silica slides (Herasil 1, by Heraeus) implanted with Au^+ ions with a 200 keV high-current Danfysik 1090 implanter at the INFN-INFM Ion Implantation Laboratory of INFN-Legnaro National Laboratories (Padova, Italy). Implantations were performed at room temperature and the current densities were maintained lower than $2\,\mu A/cm^2$ to reduce sample heating. The implantation conditions, 190 keV energy and $3–4 \times 10^{16}$ Au^+/cm^2 ion fluence, were chosen to have, after annealing, a subsurface buried layer of Au nanoparticle precipitation of about 100 nm thick (the ion projected range is about 70 nm with a calculated straggling of 11 nm, see fig. 3b). The used fluence produces a peak concentration of dopant of about 10–15 at.%, which is above the threshold for spontaneous colloid precipitation (about 1 at.%). Two sets of thermal treatments were performed: i) isochronal, at constant time (1 h) and at different temperatures in air, in a H_2-Ar gas mixture, or in pure Ar; ii) isothermal, at constant temperature (900 °C) for different annealing times in oxidizing (air) atmosphere. To follow the cluster growth, we used two experimental techniques: optical absorption and transmission electron microscopy. Optical absorption spectra for all the samples were collected with a CARY 5E UV-VIS-NIR dual-beam spectrophotometer in the 200–800 nm wavelength range. Microstructural and microanalytical characterization was performed by TEM with a Philips CM30T operating at 300 kV, equipped with an EDAX Energy Dispersive Spectrometer (EDS) at CNR-IMM Institute in Bologna.

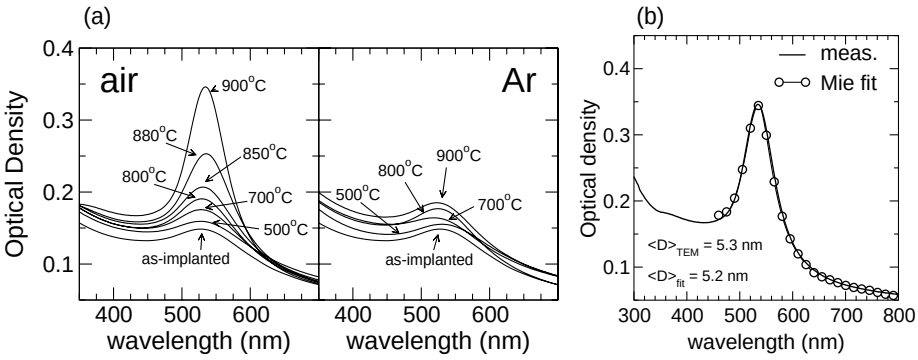

Fig. 8. – Optical absorption spectra of Au-implanted silica samples at 3×10^{16} Au^+/cm^2, 190 keV, annealed in air (left panel) or Ar (central panel) for 1 h at different temperatures. (Right panel) Empty circles represent the nonlinear fit to the sample annealed at 900 °C in air, from which the average cluster diameter $\langle D\rangle_{\rm fit}$ is obtained and compared to the TEM measured one, $\langle D\rangle_{\rm TEM}$.

4˙4. *Au cluster growth during isochronal annealing.* – The as-implanted samples were isochronally annealed in different atmospheres: air, Ar, H_2-Ar.

Figure 8 shows the optical absorption spectra of Au-implanted sample for different annealing temperatures, T_A, in air, in comparison with those measured in the samples annealed in Ar atmosphere. In the case of air annealing a clear enhancement of the surface plasmon resonance (SPR) near 530 nm due to Au clusters in the matrix [69] is evidenced above 700–800 °C, indicating the onset of faster nanoparticles growth. On the contrary, a modest increase in the SPR intensity is exhibited by the samples annealed in Ar, even at high temperature, with a growth rate as small as the one observed in the low temperature regime (< 700 °C) during air-annealing. Results very similar to the Ar case have been obtained during H_2-Ar annealings.

For the calculation of the extinction cross-section $\sigma(\omega, R)$ we have used Mie theory including multipolarity up to $l = 3$ in order to account for possible retardation effects in the largest particles [40]. The experimental bulk dielectric function used in the present study was taken from ref. [74] and corrected for finite size [40]. We have extracted through a nonlinear curve fit to the optical density the relevant parameters (average radius and standard deviation) of the $f(R)$ ($f(R)$ has been assumed to be a log-normal probability function which we verified to reproduce the TEM experimentally observed size-distribution). We have assessed the reliability of this procedure from the agreement of its results with those obtained by TEM, as can be seen in the right panel of fig. 8, which shows the optical spectra of the air-annealed samples at 900 °C for 1 hour along with the corresponding nonlinear fit obtained from eq. (25).

The evolution of cluster size with the temperature during air annealing can be seen in the TEM cross-sectional views of fig. 9, where for comparison also the TEM micrograph of the Ar-annealed sample at 900 °C is shown. Almost spherical Au clusters of different size are present in all the samples up to a depth of $\sim$ 130 nm from the sample surface. Due to low gold diffusivity, the centroid of gold concentration does not move appreciably during the annealing and remains approximatively near the implantation projected range ($\sim$ 70 nm), where, as the temperature increases, the largest clusters are formed.

The cluster size distributions for the TEM analysed samples are also reported in fig. 9. The progressive shift of the average cluster size towards higher values and the

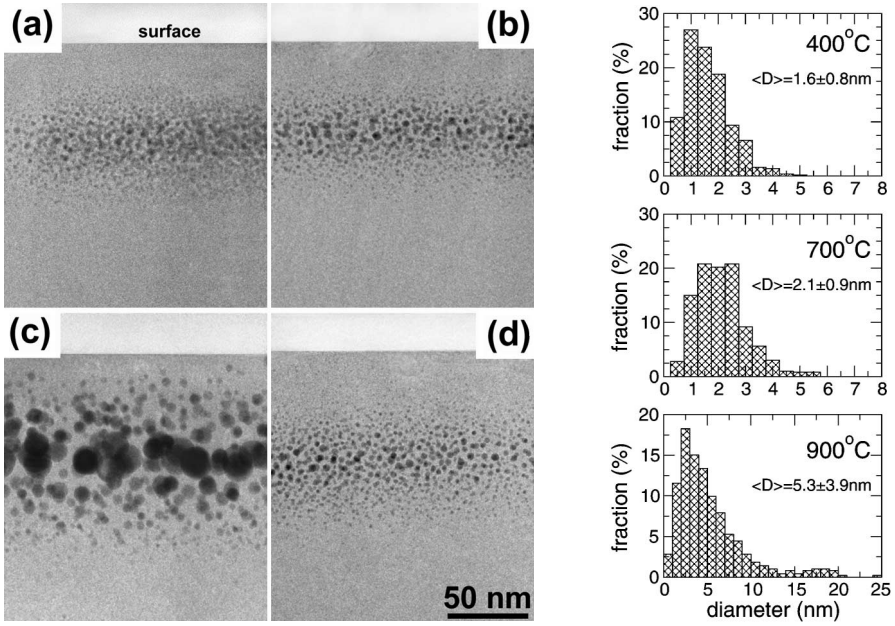

Fig. 9. – Cross-sectional bright-field TEM views of Au-implanted silica samples at 3×10^{16} Au^+/cm^2, 190 keV, annealed for one hour at: (a) 400 °C in air, (b) 700 °C in air, (c) 900 °C in air, and (d) 900 °C in Ar, respectively. On the right, the histograms of the size distribution of the samples annealed 1h in air at different temperatures.

corresponding broadening of the distribution is evident. The results of TEM analysis give for the average cluster diameter $\langle D \rangle_{400°C} = 1.6 \pm 0.8$ nm, $\langle D \rangle_{700\,°C} = 2.1 \pm 0.9$ nm, $\langle D \rangle_{900°C} = 5.3 \pm 3.9$ nm for the samples annealed in air at 400 °C, 700 °C and 900°C, respectively.

The remarkable differences in the size distribution after annealing in the atmospheres presently investigated at 900°C for 1 hour are sketched in table II: whereas Ar and H_2-Ar annealing give comparable results ($\langle D \rangle = 2.1 \pm 0.9$ nm and $\langle D \rangle = 2.5 \pm 1.2$ nm, respectively), the sample annealed in air exhibits much larger and size-distributed clusters with $\langle D \rangle = 5.3 \pm 3.9$ nm. To better understand these results, we have analysed them as a function of the temperature.

Figure 10 reports the Arrhenius plot of the squared average cluster radius after annealing in air or Ar, at fixed time, 1 hour. The corresponding data for the H_2-Ar atmosphere are not reported, being very similar to the Ar case. The abrupt increase of cluster size, evidenced by fig. 10 at about 800°C and also observed in the optical spectra intensity of

TABLE II. – *TEM measured histograms of size distribution in the samples annealed* 1 *h at* 900 °*C in different atmospheres: Ar, H_2-Ar, and air.*

	Ar	H_2-Ar	Air
$D \pm \sigma$ (nm)	2.1 ± 0.9	2.5 ± 1.2	5.3 ± 3.9

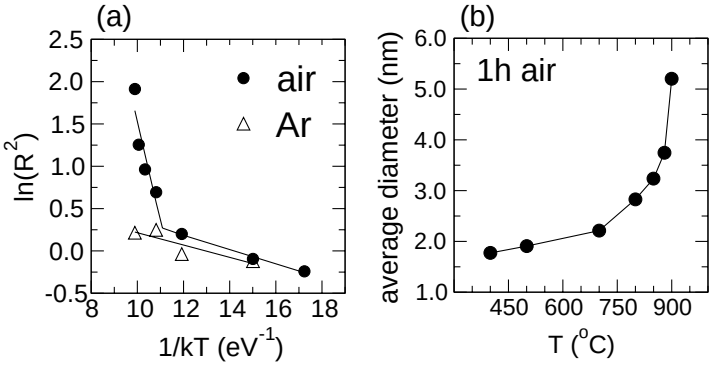

Fig. 10. – (a) Arrhenius plot of the squared average cluster radius R2 after 1 h annealing in air (filled circles) or argon (empty triangles). Solid lines are linear fit to the experimental data. (b) Average cluster diameter of Au-implanted silica samples at 3×10^{16} Au^+/cm^2, 190 keV, annealed in air for 1 h at different temperatures.

fig. 8 (left panel) at the same temperature for air annealings, suggests that two different regimes for cluster growth occur during thermal treatments in air up to 900 °C. To better appreciate in linear scale the actual temperature dependence of the cluster radius, the measured values obtained by TEM and optical fit are reported as a function of the air annealing temperature.

To understand these two different regimes, observed during annealing in air but neither in Ar nor in H_2-Ar atmospheres, it is necessary to look at the basic processes involved in gold diffusion in a silica matrix where Si-O bonds have been broken by ion implantation and where different diffusing species, oxygen or hydrogen or argon, may, or may not, interact both with the matrix and/or with the precipitating element. To do this, in the following section we will try to establish a general thermodynamic framework where the gold clustering process may be analysed in terms of correlated diffusion parameters.

4˙5. *Clustering of Au atoms under correlated diffusion.* – From fig. 10, we observe that below 700–800 °C the cluster radius increases very slowly with the annealing temperature, at constant time, independently from the atmosphere composition, due to low gold diffusivity. This very modest temperature dependence suggests a diffusion mechanism controlled by radiation damage [75,76]. The measured activation energy of 1.17 eV/atom for gold diffusion in silica during annealing in air, in the temperature range from 750 to 900 °C, is very different from the literature value of 2.14 eV/atom [67]. Note however that the activation energy for the molecular oxygen diffusion mechanism through an interstitial mechanism is in the range from 1.1 to 1.3 eV/atom [77, 78]. Considering that the clustering process is associated with gold diffusion, we have to understand why oxygen may favour the precipitation of the metallic element. As a first guess, we may suppose that heating in air may favour, through oxygen migration, the annealing of radiation-induced defects in silica mainly connected to the Si-O bond breaking with oxygen atoms displaced from their equilibrium lattice position. From this point of view we expect that gold diffusion could be enhanced in a recovered matrix. However this seems not the case because during implantation there is not preferential loss of oxygen from the silica matrix as proved by TRIM calculation [79, 5] and so the oxygen atoms necessary to recover the silica matrix damage are already present in the gold implanted silica.

Nevertheless, the low Au diffusivity is evidenced in Ar and H_2-Ar annealing atmospheres also in temperature regime higher than 800 °C, where the matrix recovery has been certainly completed [80]: moreover, Rutherford Backscattering Spectrometry (RBS) did not evidence an appreciable modification in the gold concentration profiles. Therefore, to explain the role of oxygen in promoting gold diffusivity we may suggest that there is a thermodynamic interaction between oxygen and gold. In the framework of the thermodynamics of irreversible process one may say that the chemical potential of oxygen in the silica matrix depends on both the matrix as well as gold concentration.

The continuity equations for the excess O_2 and Au atomic concentration n_i and n_j are

$$\frac{\partial n_i}{\partial t} = D_{ii}\frac{\partial^2 n_i}{\partial x^2} + D_{ij}\frac{\partial^2 n_j}{\partial x^2}\,, \qquad (26)$$
$$\frac{\partial n_j}{\partial t} = D_{jj}\frac{\partial^2 n_j}{\partial x^2} + D_{ji}\frac{\partial^2 n_i}{\partial x^2}\,,$$

where subscripts i and j stand for O_2 and Au, respectively, D's are the "diffusion coefficients" which are considered independent of concentration (dilute impurity limit), related to the Kelvin-Onsager phenomenological coefficients [68].

Considering now the continuity equation governing the Au^0 transport we see that, even if the D_{jj} coefficient is small in low-medium temperature regime (700–900 °C), the D_{ji} coefficient may have significant values in the same interval temperature: this implies that just the motion of the permeating oxygen drives the Au^0 diffusion. In other words, the precipitation of the metallic element is induced by the oxygen flux through the correlation coefficient D_{ji}. It is not possible to compare the activation energy of the thermodynamic correlation coefficient D_{ji} with literature data because of the general lack of information in the field of correlation coefficients. However, since the diffusion of the permeating oxygen drives the gold movement, it is not surprising to obtain a D_{ji} coefficient governed by an activation energy quite similar to the one of the interstitially diffusing O_2 molecule.

In conclusion, the main results of the investigation of the temperature dependence of the cluster radius under isochronal annealing (1 h) may be summarized as follows: i) annealing in air is more effective in promoting cluster aggregation with respect to reducing or neutral atmosphere; ii) the squared average cluster radius in an Arrhenius plot shows two different regimes upon air annealing, which can be explained by a general model for gold atom diffusion interacting with excess oxygen coming from the external ambient. The clustering regime characterized by an activation energy of 1.17 eV/atom, very different from that appropriate to gold diffusion in silica (2.14 eV/atom), is then attributed to the thermodynamic correlation coefficient, D_{ji}.

We have thus extended the analysis of the gold clustering problem for annealing in air considering annealing time intervals exceeding 1 hour, when coarsening becomes most probably the relevant cluster growth mechanism.

4˙6. *Au nucleation as a function of the annealing time.* – In this section we analyze the kinetics of gold cluster growth in silica matrix under isothermal annealing, to try to evidence the two growth regimes (*i.e.* diffusional and coarsening) as a function of the annealing time. For this purpose, fused silica slides were implanted with gold ions at a fluence of 4×10^{16} Au^+/cm^2 ion dose, *i.e.* above the threshold for spontaneous colloid precipitation and at 190 keV energy to obtain a subsurface buried layer of precipitates.

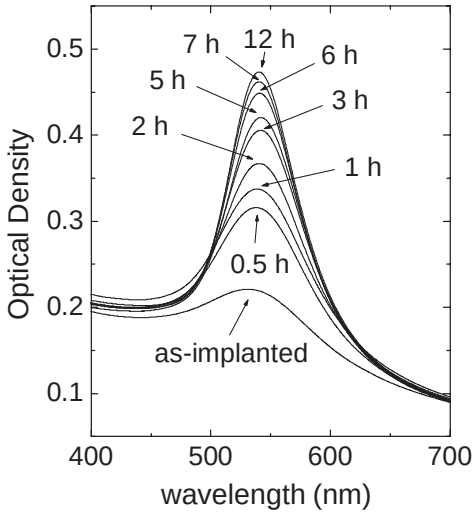

Fig. 11. – Optical absorption spectra of Au-implanted silica samples at 4×10^{16} Au^+/cm^2, 190 keV, annealed in air at 900 °C for different time intervals.

Thus, the implanted samples were annealed in air atmosphere at 900 °C for different time intervals, ranging from 0.5 up to 12 hours. We performed sample annealing in oxidizing atmosphere (air) at 900 °C, because these are the most efficient conditions for promoting cluster growth, as demonstrated in the previous subsection. Moreover at 900 °C we can disregard the influence of implantation-induced defects in the matrix which could interact both with permeating O_2 molecules and with precipitating species, *i.e.* gold atoms [67, 81, 82].

Figure 11 shows the optical absorption spectra of Au-implanted sample for increasing annealing time intervals t in air atmosphere. The surface plasmon resonance (SPR) near 530 nm, due to Au clusters in the matrix, is evident and its intensity increases from the as-implanted to the 12 hours annealed sample as expected when increasing the particles size [69]. The evolution of the cluster size as a function of the air annealing time can be followed in the TEM cross-sectional views of fig. 12 where, for comparison, also the TEM micrograph of the as-implanted sample is shown. Almost spherical Au clusters of different size are present in all the samples up to a depth of $\sim$ 120 nm below the sample surface. Due to low gold diffusivity [67], the centroid of gold concentration does not move appreciably during the annealing and remains almost near R_P ($\sim$ 70 nm), where, as the annealing time interval increases, the largest clusters are formed. The cluster size distributions, as measured in the TEM analyzed samples, are also reported in fig. 12. The progressive shift of the average cluster size towards higher values and the corresponding broadening of the distribution are evident when annealing time increases. The results of TEM analysis give the following average cluster diameters (reported as average value $\pm$ standard deviation of the experimental distribution): $\bar{D}_{\text{as-impl.}} = 2.0 \pm 1.0$ nm, $\bar{D}_{900\,^\circ\text{C,1h}} = 3.6 \pm 1.9$ nm, $\bar{D}_{900\,^\circ\text{C,3h}} = 5.6 \pm 3.5$ nm and $\bar{D}_{900\,^\circ\text{C,12h}} = 12.6 \pm 7.2$ nm, respectively.

In fig. 13 the average cluster radii are reported as a function of t. These values have been obtained either by TEM analysis (on as-implanted and 1, 3, 12 hours annealed samples) or by fitting the optical absorption spectra, according to eq. (25). A simple

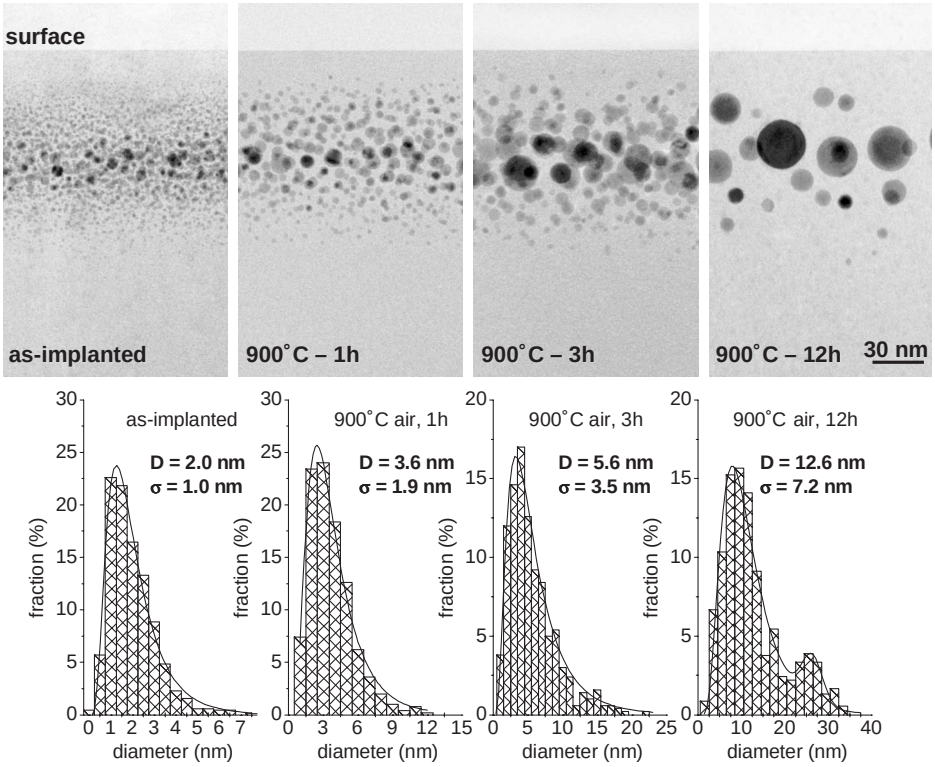

Fig. 12. – TEM results on Au-implanted silica samples annealed in air at 900 °C for different time intervals: cross-sectional bright-field micrographs with the corresponding histogram of size distribution for the as-implanted and annealed for 1 h, 3 h, 12 h samples.

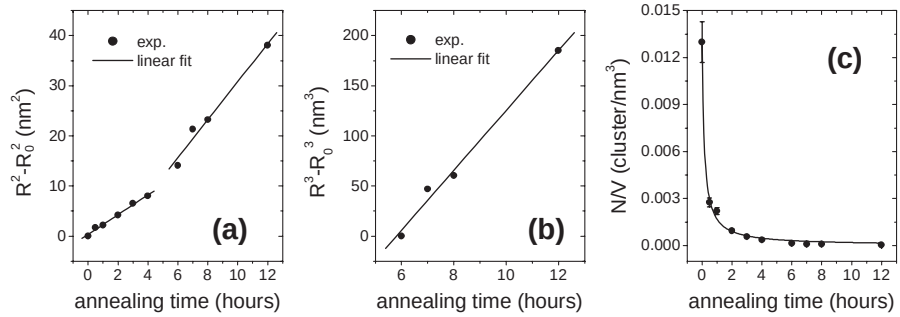

Fig. 13. – (a) $R^2(t) - R_0^2$ and (b) $R^3(t) - R_0^3$ evolution in Au-implanted silica samples annealed in air at 900 °C for different time intervals. Solid lines are the linear fits to the experimental data (filled circles) from TEM and optical fit results. (c) Cluster density in Au-implanted silica samples annealed in air at 900 °C for different times obtained by the nonlinear fit to the optical absorption spectra.

inspection of the experimental data reported in fig. 13 suggests that the kinetics of cluster growth changes with annealing times. To better evidence this point, in fig. 13(a) we report as a function of t the square of the average radius of the growing particles: there is a linear relation between the two quantities with a change of the slope in the range between 4 and 5 hours. A linear relation between R^2 and t is expected when the cluster growth is only due to the precipitation process of a supersaturated solution. More in details, the general equation for cluster growth is $R^2 = R_0^2 + KDt$, where $R(t = 0) = R_0$, K is the initial degree of supersaturation of the implanted precipitating species, and D the corresponding diffusion coefficient [83]. The change of the slope in the plot $(R^2 - R_0^2)$ *vs.* t suggests that the kinetics of cluster growth is modified. Without considering a possible change of the D parameter, not easily understandable in long time annealing experiments, the discontinuity may be explained by considering that the coarsening regime occurs, after the precipitation stage due to supersaturation, when clustering is permitted over long times. In fact, the experimental and calculated (by means of optical absorption spectrum fitting procedure) radius values, corresponding to annealing time intervals of 6, 7, 8, 12 hours, well agree with a $t^{1/3}$ law of growth, as expected in the Ostwald ripening regime: see fig. 13(b). Figure 13(c) shows the cluster density (the number N of Au clusters in the volume V) as a function of the annealing times calculated by fitting the optical density (OD) spectra. We observe a strong reduction of the cluster density in the first stage of the annealing process, which we attribute to the thermal instability of clusters of smaller size [84]. Such an instability maintains the initial supersaturation condition in the cluster growth regime, where $R \propto t^{1/2}$. At longer annealing time intervals (coarsening regime), the cluster density decreases slowly.

These experimental results prove the occurrence of the transition from a diffusion-limited regime to Ostwald ripening in the kinetics of gold cluster growth. In our experimental conditions, the transition occurs for annealing time intervals in the range between 4 to 5 hours. The theoretical approach described in subsect. **4**˙1, in particular eqs. (14) and (18), allows to calculate the diffusion coefficient D and the surface tension σ for gold nanoclusters in SiO_2 matrix. At this point it must be recalled that no reliable diffusion coefficient and surface tension data exist in the current literature for Au in SiO_2 and that the former is strongly influenced by the post-implantation annealing atmosphere. Anyway from fig. 13(a), where the quantity $R^2(t) - R_0^2$ is plotted as a function of the annealing time interval t, we evaluate, by using eq. (14), $D = 2{\times}10^{-17}$ cm^2/s, at 900 °C. We assumed for C_s the average concentration value of Au in the as-implanted sample, as determined by Rutherford backscattering, *i.e.* $C_s = 8 \times 10^{21}$ atoms/cm^3. The C_e value is neglected while $C_p = 5.9 \times 10^{22}$ atoms/cm^3, *i.e.* the atomic density of Au nanoclusters is assumed equal to that of Au bulk. To evaluate σ, the last parameter required is C_∞, the equilibrium solute concentration at a plane interface, *i.e.* the gold concentration at the interface between a gold flat surface and a flat silica surface. We suggest that in such a boundary interphase, where the gold atoms may interact with the gold surface, the C_∞ value should not be too much different from C_p. Here we assume $C_\infty = C_p$, being aware that this is obviously an upper limit for C_∞.

The slopes of the linear fit in figs. 13(a,b) (numerical values of 2×10^{-14} cm^2/h and $28{\times}10^{-21}$ cm^3/h, respectively), together with eqs. (14) and (18), allow us to estimate the gold cluster surface tension σ. The obtained value, 4×10^{-4} J/cm^2, is slightly larger than the literature data for gold surface tension [84].

Before concluding this section, we have to critically examine the numerical values attributed to the C_s parameter. Here we must underline that not all the implanted atoms take part to the clustering process at the same time for at least two reasons: first of all,

the initial gold distribution is not uniform and, as a second point, a fraction of atoms are already trapped in small clusters, that dissolve at higher temperatures. In other words, the previous evaluation of σ was based on a C_s value that is certainly overestimated by the average value of Au implanted concentration. In order to have a better estimate of C_s we may consider the density of clustered atoms, in the early stage of the process, that may be evaluated on the basis of the mean radius value and cluster density as reported in fig. 13. It is worth stressing that the variation of two orders of magnitude of the cluster density in the first stage of the process indicates that the supersaturation degree is sustained by the gold atoms released by the smallest clusters, which at 900 °C can be thermodynamically unstable or even melted well below the bulk melting temperature (1064 °C) due to the thermodynamic size effect [84]. This fact determines an almost constant supersaturation degree, which can be estimated as $C_s/C_p = 0.05$, to be compared with a value of 0.13 if C_s takes the average value of the Au implanted concentration. This more "realistic" evaluation of the supersaturation concentration degree, that is the crucial parameter of the whole process, leads to the values of 5×10^{-17} cm^2/s and 1.5×10^{-4} J/cm^2 of D and σ, respectively. We note that this value of σ is consistent with the measured gold surface tension value of a "free surface" [84]. Moreover the resulting $3{\times}10^{-7}$ cm value of the capillarity length α justifies the use of eq. (16) and the integration of eq. (18) in the linearized gradient approximation for $\bar{R} > 3$ nm: this is consistent with the data reported in fig. 13, where the transition from a diffusional to a coarsening stage, as described by eq. (17), takes place for annealing times $t > 4$ h when $\bar{R} > 3$ nm. A final remark is worth making about the approximation of considering the time evolution of the "average" cluster radius and not of the whole size distribution in the analysis of the clustering process. Indeed, such an approach does not allow to follow the effective, locally developing, growth stage of the clusters and to make a clear distinction between the two regimes in the kinetics of growth. To clarify this point, one may say that when the annealing time interval is shorter than 4 h, a fraction of the already formed clusters may grow following the Ostwald ripening mechanism while, for times exceeding 5 h some of the clusters may grow following the diffusion-limited mechanism.

In conclusion, we have investigated the clustering process of gold atoms, implanted in silica, during annealing at 900 °C in air (oxidizing) atmosphere in a time domain between 0.5 and 12 hours. By analyzing the growth of the average cluster radius as a function of time, we observed two distinct growth regimes, namely $R \sim t^{1/2}$ and $R \sim t^{1/3}$, which correspond to growth due to precipitation of supersatured solution and coarsening, respectively. By looking at the coefficients of the appropriate time scaling laws (eqs. (14) and (18)), we obtained a value of the surface tension of gold nanoparticles in silica which agrees with literature data for unsupported gold clusters, giving a check of internal consistency of the analysis and approximations made.

4˙7. *Au implantation in polymers.* – Nanocomposite materials formed of metal nanoparticles dispersed in polymers are a topic of materials science with increasing interest since these materials show excellent mechanical, gas sensing, optical, magnetic and transport properties [85,86]. As ion implantation is a well-assessed technique for the synthesis of dielectric-based nanocomposites, recently it has been applied to obtain polymer-based nanocomposites [87, 88]. The main drawback of the technique is that ion irradiation induces remarkable damage in the polymeric structure with the consequent changes in its physical properties [88-91]. This prompted for the use of radiation-resistant polymers, like polyimides [92]. Nevertheless, the issue of nanocluster nucleation in polyimides is not yet completely understood. Indeed, Kobayashi *et al.* [93] showed the growth of metal-

lic nanoparticles in Ag-, Cu- and Pd-implanted polyimides, whereas in Fe-, W- and K-implanted samples, the nucleation was not attained even at high implantation doses.

With the aim of giving a further contribution to the understanding of this field we have investigated the gold precipitation process induced by ion implantation in a polyimide matrix. We focused on gold for two main reasons: i) its chemical inertness, which allows to decouple cluster nucleation from the chemical interaction of the implanted species with the matrix components; ii) the large optical absorption cross-section of gold nanoclusters (surface plasmon resonance) in the VIS region at wavelengths larger than the optical absorption edge of the chosen polyimide. We have investigated the nanostructural, compositional and optical properties of Au- pyromellitic dianhydride-4,4′ oxydianiline (PMDA-ODA) polyimide thin films prepared by implanting different doses of Au^+ ions at the same energy. About 100 nm thick films of PMDA-ODA polyimide were deposited by glow discharge vapour deposition polymerization (GDVDP) on pure silica matrix (Herasil 1 by Haereaus). This is a very recently developed method [94] for the deposition of very thin polyimide coatings, alternative to the other better known deposition methods such as spinning, vapour deposition polymerization and ionized cluster beam deposition. The film thickness measured by Atomic Force Microscopy after curing was 100 ± 2 nm. These films were then implanted at different doses (5, 10 and 50×10^{15} Au^+/cm^2) at a beam energy of 100 keV, which corresponds to a projected range of about 60 nm and a straggling of 9 nm as simulated by SRIM. In order to reduce the heating of the polymer films during the implantation, the sample holder was water-cooled and the ion current density was kept at about 0.3 $\mu A/cm^2$. The nucleation and growth of gold nanoparticles in the sample implanted with 5×10^{16} Au^+/cm^2 has been investigated by cross-sectional transmission electron microscopy (TEM). The bright-field TEM micrograph of the sample, in fig. 14(a), shows spherical Au nanoparticles dispersed in a 40 nm thick layer, embedded between two nanoparticle-free layers: a 10 nm thick surface layer and a bottom layer of about 30 nm. The particle size distribution (fig. 14(b)) has an average value of 2.3 nm and a standard deviation of 1.3 nm. A depth profile composition by energy dispersive X-ray microanalysis (EDS) evidenced that the C content of the surface layer is higher with respect to the rest of the film, according to literature data [95,96]. This result allows to obtain a more realistic representation of the polymer composition around the clusters: indeed, the actual C:H ratio in this region could be more similar to the nominal 2:1 value considering that the C-rich surface layer partially compensates the measured C-excess, which refers to the whole structure. The TEM data have been used to simulate in the frame of the Mie theory and Maxwell-Garnett effective medium approximation [40], the optical absorption spectra of the sample implanted with 5×10^{16} Au^+/cm^2. The results are reported in fig. 14(c). In the first model used to describe the nanocomposite absorption properties spherical Au clusters with size 2.3 nm are surrounded by a matrix with refractive index of about 1.6, typical of the aromatic polyimides (this assumption can be justified by the above analysis on the local polymer composition near the Au clusters). The simulation, in which the experimental bulk dielectric function of gold has been size-corrected according to ref. [40], gives a narrow resonance centered at 550 nm instead of a large band centered at 560 nm. Even considering that the matrix could have a larger refraction index due to implantation damage [97], the simulation does not reproduce the measured spectrum because the SPR simply shifts to larger wavelengths without any FWHM broadening. We consider a second model in which the Au cluster is surrounded by a very thin carbon layer, forming a core-shell particle dispersed in a polyimide matrix. Similar approach was applied by Stepanov [88] in the study of the optical properties of Ag/polymethylmethacrylate nanocomposite obtained also by ion

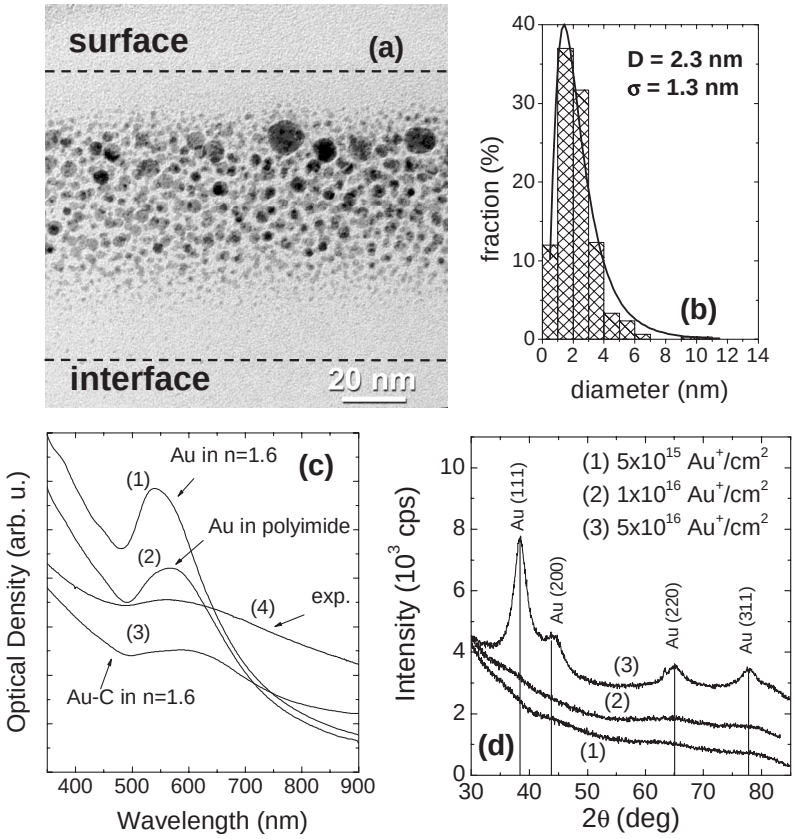

Fig. 14. – TEM and optical absorption of the sample implanted with 5×10^{16} Au^+/cm^2: (a) TEM cross-sectional micrograph (dashed lines represent the free surface and film-substrate interface); (b) nanoparticles size distribution; (c) simulated optical spectra: (1) Au cluster in a nonabsorbing medium with $n = 1.6$; (2) Au cluster in polyimide (absorbing); (3) Au(core)-C(shell) cluster in a nonabsorbing medium with $n = 1.6$; (4) the experimental spectrum of Au-implanted polyimide sample. (d) X-ray diffraction patterns as a function of the implantation dose.

implantation. Including this shell, the resonance band red-shifts but now the SPR is strongly damped by the Au-C interaction. The best agreement between experimental and simulations is obtained for a C shell thickness of about 0.8 nm, indicating that locally the composition of the matrix can be carbon-enriched. In order to account for possible effects of the matrix absorption (previously neglected by using a purely real refractive index), a calculation has been also made in the frame of effective medium theory by using for the polyimide a complex dielectric function obtained from transmittance-reflectance measurements performed on the as-deposited film [98]. A cluster filling factor of about 15% has been calculated from RBS analysis and used to combine the (size-corrected) gold dielectric function with the measured polymer one. The calculated absorption shows a better agreement with the experimental spectrum with respect to the non-absorptive case, but the local correction with a C-rich shell around the gold core seems to be qualitatively more effective in reproducing the experimental data and it is more consistent with the graphitization process usually observed in polymers after ion-irradiation. Ac-

tually, this carbon shell should be hardly perceptible in the TEM image due to the very low contrast with the polymer matrix.

In summary, gold-PMDA-ODA nanocomposites have being obtained by ion implantation. The threshold implantation dose for nanoparticle growth is around 5×10^{16} Au^+/cm^2 for 100 keV Au implantation. The nanostructure of this film consists of a gold-nanoparticle-containing layer sandwiched between two cluster-free layers, the 15 nm top layer being carbon-richer. Optical absorption spectra simulations suggest that nanoparticles are covered by a thin carbon layer forming a core-shell system of particles dispersed in a polyimide-like matrix. The combination of glow discharge vapour deposition polymerization technique, that allows depositing nanometric thin films, with ion implantation, suitable for doping materials with a large number of elements, could be a promising method to obtain new polymer-based nanostructured films with magnetic, optical, rheological, sensoring and electronic properties. Indeed, the optical gas sensing features of virgin polyimide thin film deposited by glow discharge vapor deposition polymerisation and of gold-implanted films have been recently studied by using optical absorption and surface plasmon resonance transduction techniques [99].

Optical absorption measurements were carried out in the presence of mixtures containing vapors of methanol, ethanol and gases as NH_3 in dry air onto virgin and gold-implanted films. Experimental results have shown that the virgin polyimide film does not present any variation in the absorption curves in the presence of alcohol vapors but we found a good response in case of the film implanted with a dose 5×10^{16} ions/cm^2 in which nanoparticles are present. In this case, the interaction mechanism could be related to the modification of the optical properties of the polymer and by change of the optical absorption spectrum of the composite by the modification of the surface plasmon resonance of the nanoparticles. This hypothesis is strengthened by the shift in the SPR angle reflectivity of the film, obtained in the presence of alcohol vapors that can be related to the changes of real part of n and/or in the film thickness. But we cannot exclude that gold nanoparticles contribute strongly to the sensing activity thanks to their catalytic properties. Further investigations are in progress in order to increase the performance of the sensing layer in terms of sensitivity, selectivity and stability.

5. – Ion beam direct synthesis: bimetallic clusters

As a general rule, the criterion valid for bulk systems of miscibility of the two elements as a constraint for alloy formation is not so stringent in the case of nanoclusters. This is due to the incomplete onset of the bulk properties triggered by the large number of atoms at the surface, that makes a cluster more similar to a molecular than to a massive system [100]. This leads to new possible alloy phases, which may be thermodynamically unfavoured in the bulk. In the case of noble-metal–based systems (Au-Cu, Au-Ag, Pd-Ag and Pd-Cu) perfect miscibility is expected from the bulk phase diagrams and in fact sequentially as-implanted samples exhibit direct alloying [24,101,49]. For a more detailed description of the nanostructure obtained by noble-metal sequential ion implantation in silica see ref. [25]. On the contrary, systems like Co-Cu or Au-Fe which are not miscible in the bulk showed nano-alloy formation after sequentially implantation in silica. We now briefly review some of the most relevant results obtained by the Padova group on these systems as summarized in table III.

As shown in the previous sections, in the case of noble-metal clusters the surface plasmon resonance (SPR) in the visible range is a clear fingerprint of nanoparticles formation [40]. Similarly, for noble-metals alloy the SPR resonance is located in between

TABLE III. – *Nanostructure of some investigated systems obtained by sequential ion implantation without subsequent annealing. The labeling A-B indicates the implantation order: first ion A and then ion B.*

System	Nanostructure
Au-Cu	alloy [24]
Au-Ag	alloy [101]
Au-Fe	alloy [102]
Fe-Al	alloy [103]
Pd-Ag	alloy [104]
Pd-Fe	alloy [105]
Pd-Cu	alloy [106]
Cu-Ni	alloy [107]
Ni-Co	alloy [108]
Co-Cu	alloy(*) [108]
Ag-S	core-shell [109]
Ga-N	separated [62]
In-N	separated

(*) h.c.p. and f.c.c. phase coexistence.

those of the pure elements, and is triggered by the complex interplay between the modified free electrons and interband absorptions. This can be seen in fig. 15, which shows a comparison between OD spectra either simulated with the Mie theory [32, 40] for 3 nm clusters of pure Au, Ag and $Au_{0.4}Ag_{0.6}$ alloy in silica (fig. 15a), or measured for analogous systems [49] in ion implanted silica (fig. 15b). Linear absorption measurements can therefore give the first indication of possible alloy formation. Nevertheless, in systems containing transition metals (Pd-Ag, Co-Ni,...) such a simple technique is no longer effective as interband transitions completely mask the SPR peak, resulting in a structurless absorption, which hinders any unambiguous identification of the alloy. In such cases, one has to rely on structural techniques like TEM (SAED and EDS) or EXAFS to establish alloy formation.

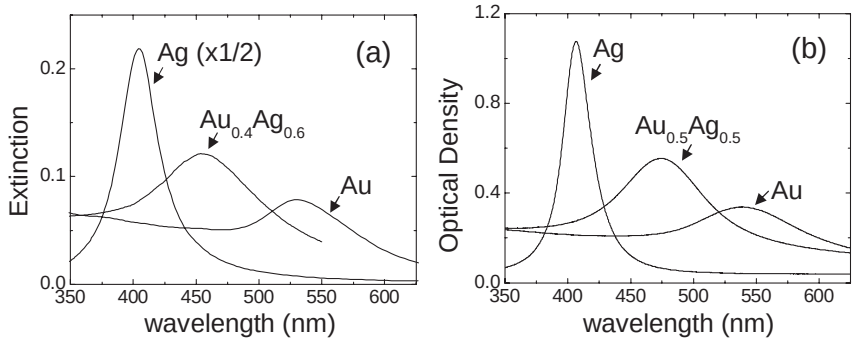

Fig. 15. – Comparison between a simulation based on the Mie theory of the optical absorption in the UV-Vis range for 3 nm clusters of pure Au, Ag and $Au_{0.4}Ag_{0.6}$ alloy in silica (a), with the experimental OD of the same systems in ion implanted silica (b).

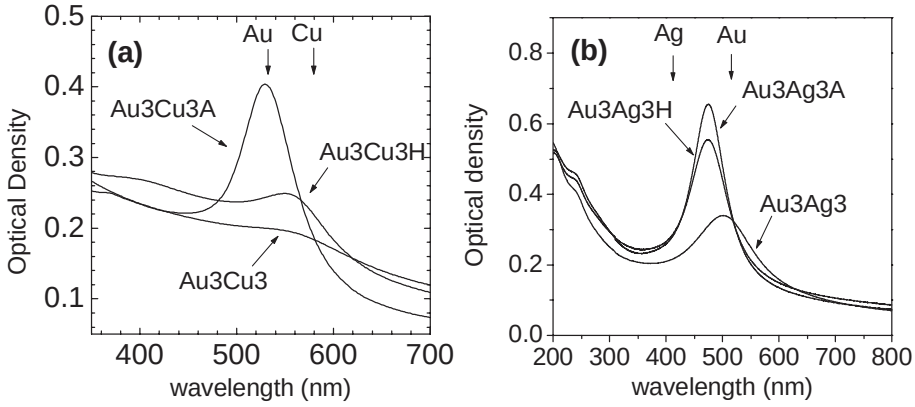

Fig. 16. – Effect of the annealing atmosphere on Au-Cu and Au-Ag alloys. (a) Optical absorption of sequentially ion implanted silica with Au (190 keV) and Cu (90 keV) at the same dose 3×10^{16} ions/cm^2 (Au3Cu3) and annealed at 900 °C for 1 hour in air (Au3Cu3A) or in reducing (Au3Cu3h) atmosphere. (b) Optical absorption of sequentially ion implanted silica with Au (190 keV) and Ag (130 keV) at the same dose 3×10^{16} ions/cm^2 (Au3Ag3) and annealed at 800 °C for 1 hour in air (Au3Ag3A) or in reducing (Au3Ag3H) atmosphere. The vertical arrows indicate the position of the SPR resonances for monoelemental clusters.

5˙1. *Au-Cu alloy.* – Fused silica slides were sequentially implanted at room temperature with Au (190 keV) and Cu (90 keV) or with Au (190 keV) and Ag (130 keV) ions at the same dose of 3×10^{16} ions/cm^2 to obtain the same projected range of about 70 nm [24, 49]. The samples are labeled according to the following scheme: the first (second) element symbol in the name designates the first (second) implanted ion species; the number after each element symbol the implantation dose in 10^{16} ions/cm^2 units; the last letter specifies the annealing atmosphere (A = air, H = H_2(4%)-Ar). For example Au3Cu3H indicates the sequential implantation of $3{\times}10^{16}$ Au^+/cm^2 + $3{\times}10^{16}$ Cu^+/cm^2, followed by an annealing in H_2(4%)-Ar atmosphere. Figure 16(a) shows the optical absorption spectra of the sample Au3Cu3 before (as-implanted) and after annealing in air or in H_2-Ar at 900 °C for 1 hour. In comparison with the as-implanted case (which shows a faint absorption band at about 560 nm), the Au3Cu3A sample exhibits a well-defined absorption peak at 530 nm which is consistent with the SPR of gold metal clusters with size in the nanometer range [40]. The optical absorption of the sample Au3Cu3H annealed in H_2-Ar is similar to the as-implanted one, even if the absorption band at 560 nm is now sharper and more intense, suggesting that the average cluster size is increased. It is worth noting that the SPR peak position of Au3Cu3 and Au3Cu3H is located in-between that of pure Au and Cu nanoclusters (which are at about 530 nm and 570 nm [2], respectively). Therefore, the absorption band observed in fig. 16(a) on the Au3Cu3 and Au3Cu3H samples suggests that a possible intermetallic Au-Cu alloy could have been formed instead of two separated metallic systems, which on the contrary would give rise to double peaked spectra.

This is confirmed by the structural analysis. Indeed, cross-sectional TEM analysis pointed out that the as-implanted sample exhibits spherical clusters with average diameter $\bar{D} = 3.8 \pm 1.6$ nm (mean value ± standard deviation of the distribution). Selected area electron diffraction (SAED) analysis indicated a single f.c.c. phase with lattice constant $a = 0.3958(15)$ nm. This value is not consistent with the experimental values

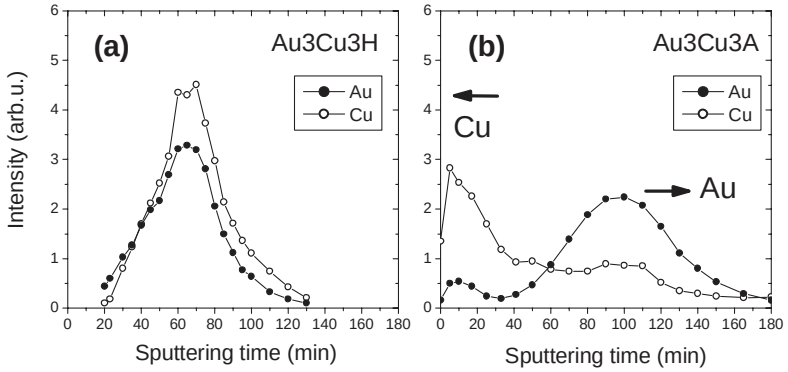

Fig. 17. – XPS concentration profiles of Au and Cu in the sample Au3Cu3 after 1 h thermal annealing at 900 °C in (a) reducing atmosphere (Au3Cu3H) or (b) air (Au3Cu3A).

of the pure bulk phases of either gold ($a_{\mathrm{Au}} = 0.40786$ nm) or copper ($a_{\mathrm{Cu}} = 0.36150$ nm), thus showing that an $\mathrm{Au}_x\mathrm{Cu}_{1-x}$ intermetallic alloy has been formed. Indeed, it is known [110] that the lattice parameter of the continuous Au-Cu solid solution phase exhibits a positive deviation from an assumed Vegard's law, as follows:

$$a_{\mathrm{alloy}} = x\, a_{\mathrm{Au}} + (1-x)\, a_{\mathrm{Cu}} + 0.01198\, x\, (1-x)\,. \tag{27}$$

Inserting our measured lattice parameter in eq. (27), a value of $x = 0.67(3)$ was obtained, which corresponds to an atomic ratio $\alpha = [\mathrm{Au}]/[\mathrm{Cu}] = 2.1$. It is worth noting that EDS compositional analysis obtained at the AuM and CuK peaks in the spectra gives an average value $\alpha_{\mathrm{EDS}} = 1.5$, which is slightly lower than the SAED results. This demonstrates that part of the copper atoms do not form the alloy but remain, after implantation, in a different (atomic or oxidized) state in the matrix. Further characterization by XPS and EXAFS measurements confirmed that part of the Cu atoms remained in the matrix, and only with an annealing in reducing atmosphere these atoms were driven in the alloy clusters promoting a compositional change ($x = 0.50(3)$). The clusters in the sample Au3Cu3H are spherical and their average diameter, $\bar{D} = 8.7 \pm 2.5$ nm, is increased with respect to the as-implanted sample. In this case the SAED analysis indicates the formation of an ordered Au-Cu phase which is consistent with the tetra-auricupride phase (tetragonal, $a = 0.3960$ nm, $c = 0.3670$ nm) with equal Au-Cu atomic concentration. On the contrary annealing in air induced alloy dissolution: clusters of Au were found together with very large aggregates of crystalline CuO at the sample surface. The sample Au3Cu3A shows near the surface very large (with size even in the μm range) and irregularly shaped crystallites, which give at EDS analysis a strong Cu signal with no Au present. SAED patterns show that these structures are composed of crystalline domains of CuO in the tenorite phase, with very small amount of crystalline $\mathrm{Cu}_2\mathrm{O}$. This indicates that during annealing in air, Cu migrates toward the surface where it is oxidized. Such picture has been confirmed by RBS and XPS measurements which evidenced in the Au3Cu3A sample a significant rearrangement of copper ions, which pile-up at the surface, whereas gold ions diffuse deeper in the samples, as shown in fig. 17. A loss of about 25% of copper has been detected for this sample, while no loss occurs for the Au3Cu3H one. Therefore, in comparison with Au3Cu3 and Au3Cu3H samples, which exhibit almost

TABLE IV. – *Summary of the structural and optical characterization on the Au_xCu_{1-x} alloy systems.*

Sample	Annealing conditions	Size([a]) (nm)	Structure (SAED)	x alloy	Lattice const. (nm)	SPR (nm)
Au3Cu3	-	3.8 ± 1.6	f.c.c.	0.67(3)	$a = 0.3958(15)$	550
Au3Cu3H	H_2, 900 °C, 1 h	8.7 ± 2.5	tetrag.	0.50(3)	$a = 0.3960(12)$, c = 0.3670(12)	550
Au3Cu3A	air, 900 °C, 1 h	33 ± 20	f.c.c. + CuO	0.97(3)	$a = 0.4060(12)$	532

([a]) Average diameter ± standard deviation of the TEM experimental size distribution.

coincident Gaussian in-depth distribution of the implanted species, Au3Cu3A samples show a splitting of the two distributions with inward and outward migration of gold and copper, respectively. Moreover, XPS measurements clearly indicate the presence of oxidized copper (CuO) at the surface. Below these copper oxide crystallites, the TEM analysis showed spherical clusters with mean diameter $\bar{D} = 33 \pm 20$ nm. The SAED pattern in this region shows the presence of Debye-Scherrer rings of an f.c.c. phase, together with some spots coming from the copper oxide at the surface. From the SAED results, an estimation of the lattice constant $a = 0.4060(12)$ nm for the f.c.c. phase was obtained, which is consistent with that of bulk gold. It has to be pointed out that along with these strong rings some weaker spots can be detected in the SAED pattern, which correspond to an f.c.c. phase with a smaller a, indicating that very few alloy clusters are still present even after annealing, as confirmed by EDS measurements on single clusters. The results of the above analysis are summarized in table IV.

We followed the alloy decomposition performing a short (15 min) annealing in air to the already H_2-annealed sample [111]: TEM analysis showed that most of the clusters were composed of two interpenetrated parts, one made of an Au-rich Au_xCu_{1-x} alloy ($x = 0.93(3)$) and the other made of Cu_2O (see fig. 18d). Such phase exhibited an optical absorption band at about 620 nm, related to the observed Au-Cu_2O core-shell–like structure. Therefore, alloy decomposition takes place with the progressive oxidation of Cu, which is extracted by oxygen from the alloy clusters: it is interesting to note that from SAED analysis it turned out that these two phases (Au_xCu_{1-x} alloy and Cu_2O) share the same crystallographic structure (cubic) and same axes orientations, as if the f.c.c. alloy cluster was a sort of structural template for the out-coming oxide. From these results it is clear that sequential Au/Cu ion implantation is able to give directly alloyed Au-Cu colloids. A possible mechanism for the alloy formation is an enhanced diffusion of copper in small gold clusters [100,112] during the implantation. Subsequent annealing in hydrogen can be used to increase the average size of the clusters with a change in the structural ordering of the alloy by driving copper atoms (dispersed in the matrix) toward the already formed clusters, increasing their size and shifting the Au/Cu concentration toward the nominal 1:1 ratio, therefore inducing a structural disorder-order phase change. On the contrary, annealing in oxidizing atmosphere promotes a separation of the two species, assisted by a chemical interaction between copper and oxygen. Another point that is worth noting is that, with respect to single Au ion implantation, the second implant of Cu introduces a correlated diffusion between Au and Cu atoms during thermal

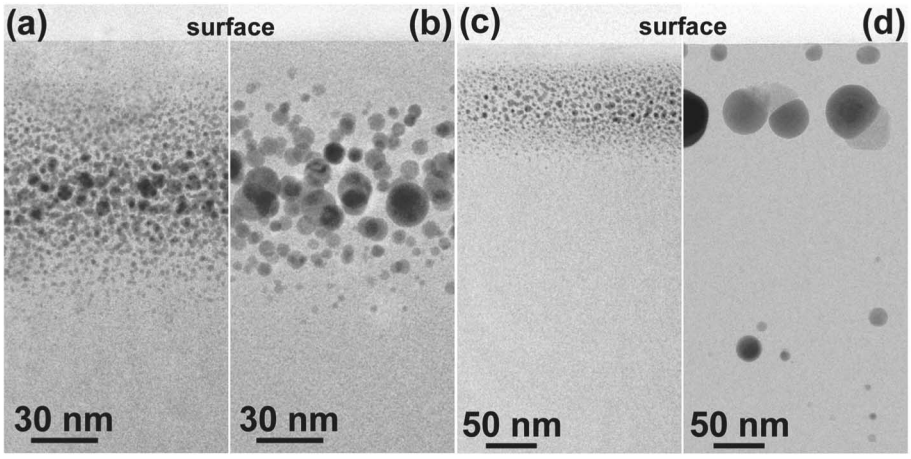

Fig. 18. – Cross-sectional bright-field TEM images of ion implanted silica substrates: (a) single implant Au (190 keV, 3×10^{16} ions/cm^2); (b) sample in (a) after annealing in air 900 °C 3h; (c) sequential Au (190 keV) and Cu (90 keV) at the same dose 3×10^{16} ions/cm^2; (d) sample in (c) after annealing at 900 °C first in H_2-N_2, 1h and then in air, 15 min. Note the different scale marker in (a) and (b) with respect to (c) and (d).

annealings. This can be seen in fig. 18, which shows a comparison between single Au implant (fig. 18a,b) and sequential Au/Cu implant (fig. 18c,d same dose and energy) before and after annealing. Not only the clusters size increases but a remarkable in-depth diffusion of both Cu and Au is present, as some alloy nanoclusters are visible well beyond the implantation range. This is in agreement with the model of correlated diffusion of Au in presence of oxygen [68], quoted above.

The picture that emerges from TEM and optical results (summarized in table IV) is that sequential ion implantation is able to give directly alloyed Au-Cu colloids. Subsequent annealing in hydrogen can be used to increase the average size of the clusters with a change in the structural ordering of the alloy. On the contrary, if the as-implanted sample is annealed in an oxidizing environment, a separation of the two species takes place, assisted by a chemical interaction between copper and oxygen, as will be described in more detail in the next subsection. It is interesting to note that this can be done in a reversible way: SAED results on Au3Cu6 systems annealed first in air and then in hydrogen evidence again the formation of Au-Cu alloy clusters. The question is whether this transition follows a solid-solid path or it is assisted by an intermediate solid-liquid transition of the alloyed clusters. Indeed, from the phase diagrams of the Au-Cu system, the melting point of the 1:1 Au:Cu alloy is just at 900 °C: moreover, due to the nanometric size of the clusters, a depression of this melting temperature could take place according to the thermodynamic size effect [84]. The fact that annealing in air at the same temperature is able to separate the two species may indicate the latter mechanism could play a significant role.

5˙2. *Au-Ag alloy.* – Silver nanoclusters embedded in glasses are among the first nanocomposites realized by ion implantation [69, 113, 114]. Nanoclusters of silver-gold alloy in silica matrix are, in many respects, a good system for investigating the physical processes involved in the alloy formation. In fact, because of the complete mixing of the

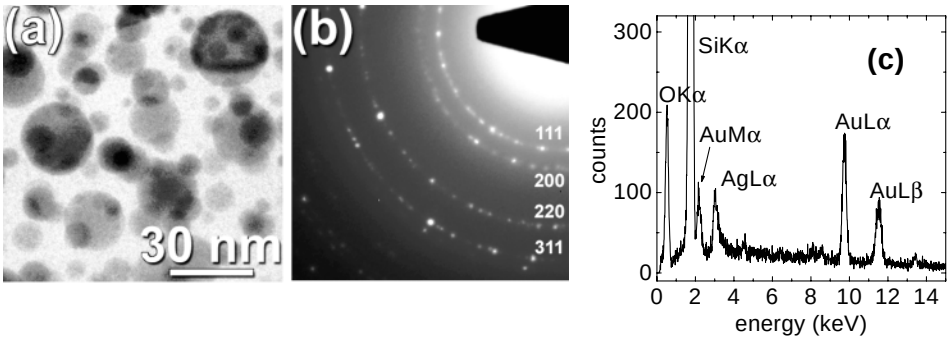

Fig. 19. – (a) Cross-sectional bright-field TEM images of sequentially ion implanted silica with Au (190 keV) and Ag (130 keV) at the same dose 3×10^{16} ions/cm^2 and annealed in air at 800 °C for 1 hour (Au3Ag3A); (b) SAED pattern showing a single f.c.c. Debye-Scherrer pattern of AuAg alloy; (c) EDS spectrum on a single cluster containing both Au and Ag.

two components and their low reactivity with other atomic species, the alloy formation and clustering process is expected to depend mainly on the diffusivity of the two metals in silica: this should have in principle a relevant role especially during a post-implantation thermal annealing. The drawback of this system regards the difficulty of its structural characterization: the small mismatch in the lattice parameters of the two single metal makes the diffraction techniques not suitable for detecting the alloy formation, especially for nanoclusters, whose reduced size results in a broadening of the diffraction peak width. Therefore one has to use either optical characterization or compositional techniques like EDS or EXAFS spectroscopy. Performing measurements at the absorption edge of both Au and Ag atoms, the alloy formation can be unambiguously detected, since different atom species present in the local environment around the implanted ones are distinguished. The investigated systems were prepared by sequential Au+Ag ion implantation in silica slides: the implantation energy was 190 keV for Au ions and 130 keV for Ag ones. The implantation doses were $3{\times}10^{16}\mathrm{Au}^+/\mathrm{cm}^2$ and 3–$6{\times}10^{16}\mathrm{Ag}^+/\mathrm{cm}^2$.

Similarly to the Au-Cu case, also sequential Au and Ag implantation in silica (at the same dose 3×10^{16} ions/cm^2) resulted in a $\mathrm{Au}_x\mathrm{Ag}_{1-x}$ alloy (fig. 19). Indeed, optical absorption spectra show a single SPR resonance near 500 nm (as expected from the above reported Mie simulations for AuAg alloy), which shifts to 475 nm upon annealing, irrespective from the atmosphere fig. 16b. Alloying in such system has been also demonstrated by TEM EDS measurements on single clusters (indicating that both Au and Ag were present, fig. 19c) and by EXAFS analysis. The reduced interaction between Ag atoms and oxygen, with respect to Cu, makes the annealing less effective in inducing separation of the alloy obtained in the as-implanted samples. Moreover, only minor differences can be evidenced between air and H_2 annealing, as can be seen from the OD data shown in fig. 16b.

The left panel of fig. 20 shows the Fourier transform moduli of EXAFS spectra for the Au L_{III} and Ag K absorption edges of Au+Ag implanted samples. The peak at about 2.5 Å (double in the case of sample Au3Ag3) indicates an intermetallic first shell correlation; no evidence of metal-oxygen correlation is found. Details on the fitting procedure are found in refs. [115, 116], while fit quality is shown in fig. 20. It was found that for both the as-implanted samples, on the average, either silver and gold atoms are surrounded in the first shell by silver and gold atoms. This indicates that gold-silver

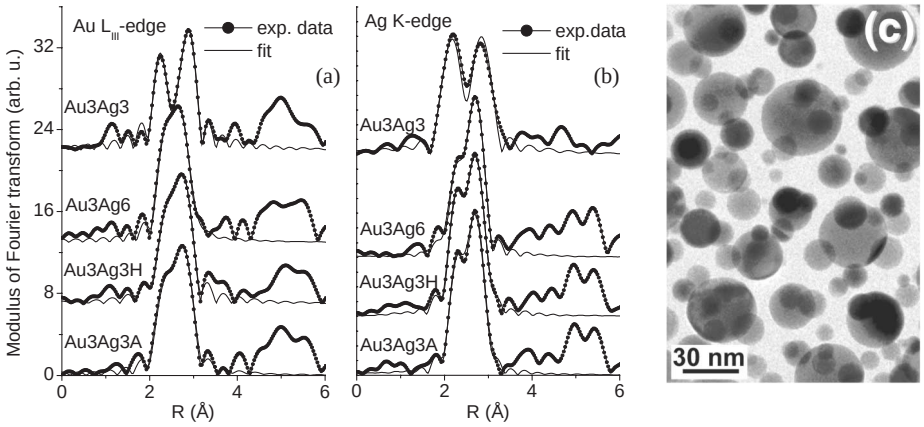

Fig. 20. – k^3-weighted Fourier transform moduli and relative first shell fits of EXAFS spectra of the Au+Ag-doped samples measured at (a) Au L_{III}-edge (in the range $k = 3.9$–12.8 Å^{-1}), and (b) Ag K-edge (in the range $k = 2.7$–12.6 Å^{-1}, except for Au+Ag sample whose spectrum was truncated at $k = 9.8$ Å^{-1}): all the spectra were measured cooling the sample at 77 K. (c) Planar-view bright-field TEM micrograph of the Au3Ag6A sample.

binary alloy nanoclusters are formed after sequential Au+Ag implantation, independently of the dose of Ag ions. Moreover, with respect to the situation before silver implantation, the total number of atoms in the first shell slightly increases, suggesting a growth of gold-containing nanoclusters, probably supported by silver atoms that fed preexisting gold clusters. For the local environment around silver atoms, as already noticed, two coordinations (Ag-Ag and Ag-Au) were found: the corresponding interatomic distances are compatible with those of the metallic silver and gold bulk phases in the case of Au3Ag6 sample (high Ag dose), whereas they result contracted (especially the Ag-Ag one) for Au3Ag3 sample (equal dose for Au and Ag implants). This could indicate that in Au3Ag3 sample the cluster size is low (around 1–2 nm), and lower than in Au3Ag6 sample. It is known that the crystallization of the alloy occurs, at least in the bulk phase, as a solid solution [117]: thus, from the relative percentage of the two kinds of atoms in the first shell, the nanocluster alloy composition can be estimated. This can be done starting from some hypotheses. The first is that the alloy takes place in the cluster as a solid solution, at least for the first shell ordering. The second is that alloy clusters are the dominant phase, *i.e.* little percentage of single-metal clusters are present. Based on these assumptions, for the Au3Ag6 sample (high Ag dose), the ratio of silver/gold atoms in the first shell (and so in the alloy) results approximately [Ag]/[Au]$\simeq 2$ (2.0 when calculated from the first shell around silver, 1.7 from the first shell around gold): this value reflects the implantation doses. For the sample with equal Au and Ag doses (sample Au3Ag3), the same considerations lead to a silver/gold ratio [Ag]/[Au]$\simeq 0.5$. Therefore, assuming that most of the clusters are formed by Au-Ag alloy, it is clear that different silver implantation doses determine a different alloy composition. In particular, for equal Au and Ag doses, the alloy is rich in gold, probably because a part of silver atoms feeds the pre-existing gold clusters so leading to Au-Ag clusters, and part of silver atoms remain dispersed in the alloy. In fact, from EXAFS results, the total number of atoms in the first shell around silver atoms is slightly lower than the total number of atoms around gold atoms: this indicates that the percentage of silver atoms dispersed in the matrix

is higher than that of gold atoms, so that the alloy clusters result rich in gold, even if the implant occurred with equal doses for the two components. Concerning the Au3Ag6 sample (high Ag dose), the alloy composition respects the implantation doses, indicating that in this case the same relative fraction of Au and Ag atoms remains dispersed in the host. Concluding, double implantation of Au+Ag in silica determines the formation of silver-gold f.c.c. nanoclusters; the mean composition of the alloy clusters depends on the relative implantation doses of the two dopants: the alloy results poor in silver for equal Au and Ag implantation doses, and is in agreement with the total doses of dopants present in the matrix (about 2Ag:1Au), for Ag dose double than Au one. Part of silver and gold atoms remained dispersed in the matrix. No evidence of oxide phase was found.

Considering the effect of the thermal treatments performed for 1 h at $T = 800\,^{\circ}\mathrm{C}$ on Au+Ag implanted system, the RBS spectrometry analysis did not detect significant changes in the dopant concentrations. This is found no matter what kind of atmosphere (reducing or oxidizing) is used for the thermal treatments. The TEM analysis on the Au3Ag6A sample annealed at 800 °C in air evidenced clusters with size 14.3 ±7.9 nm, as shown in fig. 20. The SAED analysis found randomly oriented f.c.c. nanocrystals. The compositional analysis, performed with a field emission STEM microscope by focusing a nanometric electron probe on single clusters [101], indicated the presence of both Au and Ag atoms in the same nanocluster, therefore assessing the alloy formation (see fig. 20). EXAFS analysis was performed for both Au and Ag absorption edges on two samples with equal Au and Ag concentrations (corresponding to an effective implantation dose of $3{\times}10^{16}$ ions/cm^2 for each species), annealed in either reducing or oxidizing atmosphere. Results of the fitting procedure evidenced in both cases the presence of Au-Ag alloy nanoclusters. The main difference with respect to the as-implanted case is in the alloy composition: in the case of annealed samples the alloy composition is balanced (about 1:1). Therefore, the effect of annealing, starting from gold-rich alloy clusters, is mainly to promote the aggregation of silver atoms that in the as-implanted sample were dispersed in the matrix, in the alloy nanocluster, so shifting the alloy composition towards the retained doses, as evidenced for the Au-Cu system.

Silver out-diffusion upon thermal annealing in air was clearly observed in silica samples, containing silver nanoclusters, prepared by sol-gel method [118]. At the annealing temperature used here ($T = 800\,^{\circ}\mathrm{C}$), the bulk phase is still solid (the melting temperature for $Au_{0.5}Ag_{0.5}$ is about 1030 °C). On the other hand, it is known that a decrease of the melting temperature (as large as 15% for 5 nm gold particles) could take place in small clusters, because of the presence of cluster surface tension that comes into play in the expression for the chemical potential [84]; actually, even if this should be experimentally checked, the heating temperature is probably low enough to preserve nanoclusters in the solid solution; anyway, in this case the silver out-diffusion did not take place.

Thus, the effect of thermal treatment at 800 °C for 1h of Au+Ag-implanted silica is to promote further aggregation of dopant atoms in clusters that are mainly formed by silver-gold alloy; their composition, starting from Au-rich alloy (in the Au3Ag3 sample before annealing) respects the implantation doses. This indicates that the effect of annealing is to promote silver diffusion into the clusters. The selective influence on the cluster stability of the annealing atmosphere, observed for the Au/Cu system (see previous subsection), is less effective for the Au/Ag one, considering the lower chemical interaction between gold or silver and oxygen.

5˙3. *Nonlinear optical properties of Au-based alloys.* – Metal quantum-dot composites, in particular metal nanocluster composite glasses (MNCGs), exhibit an enhanced optical

Kerr susceptibility, $\chi^{(3)}$, whose real part is related to the n_2 coefficient of the intensity-dependent refractive index, usually defined as $n(I) = n_0 + n_2 I$, where n_0 and I are the linear refractive index and the intensity of the light, respectively. Correspondingly, also a nonlinear absorption takes place which can be described macroscopically by the intensity-dependent absorption coefficient $\alpha(I) = \alpha_0 + \beta I$, where α_0 and β are the linear and nonlinear absorption coefficients, respectively. This nonlinearity can be described for centro-symmetric systems (like randomly dispersed nanoclusters in an amorphous matrix, which do not exhibit even order contributions) as a third-order correction in the external field $\vec{E}$ to the linear polarization $\vec{P}$, whose component i reads

$$P_i = \varepsilon_0 \left(\sum_j \chi_{ij}^{(1)} E_j + \sum_j \chi_{ijkl}^{(3)} E_j E_k^* E_l \right) . \tag{28}$$

MNCGs exhibit high nonlinearity in the picosecond regime [22, 45, 119]. They could offer the possibility to realize all-optical switching devices, *i.e.* operating in a time range faster than the electronic ones and without converting optical signals to electronic form. Among the techniques for the measurement of the nonlinear refractive index of a material, Z-scan allows to determine both sign and magnitude of n_2. The technique, originally proposed by Sheik-Bahae *et al.* [120], was since then implemented and applied to the study of several nonlinear composite glasses [121,122]. Z-scan technique is very sensitive to detect small nonlinear refractions, however it is difficult to discriminate between electronic and thermal effects. In particular, the use of high repetition-rate lasers for the Z-scan experiments [22, 2, 55] may trigger important heating of the composite glasses, giving rise to thermo-optical nonlinearities (due to cumulative heating of the sample) that can obscure all fast relaxation processes. The aim of our work [123] was to evidence and evaluate the importance of the heating effects among the physical origins of the nonlinear optical properties exhibited by MNCGs.

To avoid sample heating, Z-scan measurements were performed using a ring-cavity, mode-locked Nd:glass laser as a source. This laser supplies single shots at a very low repetition rate (about 1 Hz), each one being a train of about 100 pulses of nearly equal intensity. The single pulse duration is about 6 ps, and the time separation between two pulses is about 5 ns. The laser was operated in the TEM_{00} mode at fixed power output; peak power was about 140 MW. The beam waist w_0 at the focal point of the apparatus was about 25 μm. Using filters of different optical density, the peak intensity at the focal point could be varied in the range between 50 MW/cm^2 and 15 GW/cm^2. Each point in the Z-scan curve is the average of 20 shots. We used both the fundamental ($\lambda = 1064$ nm) and the second harmonic ($\lambda = 532$ nm) of the laser.

Very interesting fast nonlinear optical properties are shown by the Au3Ag6A and Au3Cu6H samples, as shown in fig. 21. By means of the Z-scan technique, a nonlinear refractive index n_2 of $(-1.6\pm0.3)\times10^{-10}$ cm^2/W (fig. 21a) and $(+6.3\pm1.2)\times10^{-11}$ cm^2/W (fig. 21c) was measured at 527 nm of wavelength [123], respectively. Just to have an idea of the increase in the nonlinear optical properties due to the nanoclusters, the pure silica matrix has a $n_2(SiO_2) = 5 \times 10^{-16}$ cm^2/W. It is important to stress that these measurements were realized in experimental conditions to avoid cumulative heating effects, *i.e.* by using a single 6 ps long laser pulse at 1 Hz repetition rate. The peculiarities of this experimental finding are the very large modulus value of n_2 and the sign change according to the cluster composition. Such high value of the fast n_2 coefficient has never been detected in MNCGs up to now [56]. An explanation of this evidence can be given

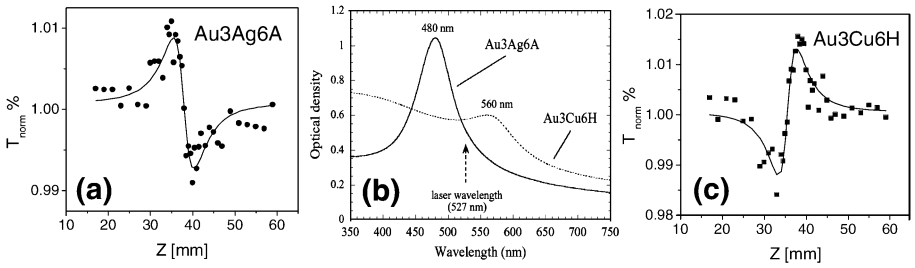

Fig. 21. – Z-scan curves of the Au3Ag6A sample (a) and Au3Cu6H sample (c). The optical absorption of the two samples and the position of the laser wavelength is shown in (b).

by considering that for metal volume fractions (*i.e.* filling factors) p around 0.1 and near the SPR wavelength, the mutual electromagnetic interactions among nanoparticles begin to induce deviations from the low-p approximation of the third-order optical Kerr susceptibility, $\chi^{(3)}_{\text{eff}}$, [123] which reads

$$\chi^{(3)}_{\text{eff}} = p\,\chi^{(3)}_{\text{clu}}|f_c|^2 f_c^2\,, \tag{29}$$

$$f_c = \frac{3\varepsilon_m}{\varepsilon + 2\varepsilon_m}\,, \tag{30}$$

where $\chi^{(3)}_{\text{clu}}$ is the nonlinear contribution of the cluster, ε and ε_m are the dielectric function of the cluster and the matrix, respectively and f_c is the local field enhancement factor.

The effect of this mutual influence has been estimated for a linear chain of gold nanoparticles embedded in silica [124]: the modulus of the local-field enhancement factor results larger than that predicted by the low-concentration approximation, and the difference is much more marked at the SPR wavelength. Mutual interaction among nanoparticles could then explain the large values of the n_2 coefficient found in Au3Ag6A and Au3Cu6H MNCG samples. As far as the sign reversal of the nonlinear refractive index as a function of the cluster composition is concerned, this evidence in a MNCG is related to the relative position in wavelength of the nanoparticle surface plasmon band with respect to the used laser (527 nm), as shown in fig. 21b. The local-field enhancement factor for alloy nanoclusters embedded in silica glass has been computed in the frame of Mie theory, starting from experimental bulk dielectric functions of a metallic Au-Ag alloy and correcting them for the finite size of the particles [123]. Indeed, the negative sign of n_2 is well explained by considering the wavelength dependence of the nanoparticles local-field factor.

The peculiar optical properties of composite materials formed by transition metal clusters embedded in glass matrices, have made them famous since literally millennia. The first glasses containing metal clusters were indeed fabricated by Roman glassmakers in the fourth Century AD. Figure 22 shows the marvelous Lykurgos goblet. Such goblet depicts the death of the King Lykurgos and is made of a soda-lime glass containing silver and gold, in the form of Au_xAg_{1-x} nanoclusters, at a percentage concentration of 3×10^{-4} and 3×10^{-5}, respectively. The vessel changes its colour from opaque green when illuminated in reflection (fig. 22a) to strong red when the light source is put inside (fig. 22b). This means that the "nanotechnologies" started in Roman age!! Medieval cathedral windows through several European countries witness the attention

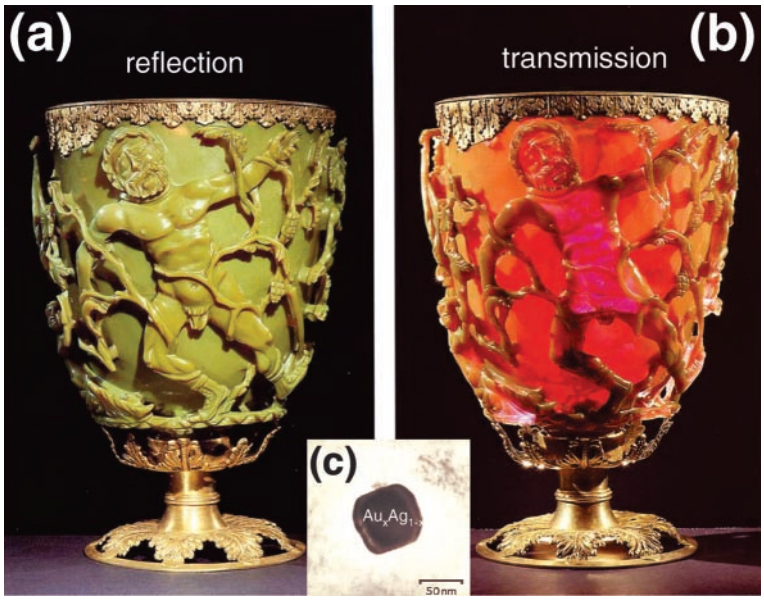

Fig. 22. – The Lykurgos Goblet (British Museum, Roman Glassmakers, 4th Century A.D.) illuminated under reflection (a) or transmission (b) condition. (c) TEM image of a Au-Ag alloy nanocluster inside the glass.

drawn by stained glasses containing metal aggregates as artistic work. They exhibit great varieties of beautiful colours owing to the nanosized metal particles embedded in the glass matrix. Luster decorations, typical of Medieval and Renaissance pottery of Mediterranean basin, substantially consist of a thin film composed of a heterogeneous distribution of silver and copper nanoparticles of sizes ranging from 5 to 100 nm (*i.e.* of a metal-glass nanocomposite thin layer [125-128]).

These decorations show peculiar optical properties, producing brilliant reflections of different colours, cangiant effects and iridescence, as shown in fig. 23. Hystorically, luster was developed in Mesopotamia during the IX century, and subsequently diffused throughout the Mediterranean basin together with the spread of the Islamic culture. It arrived in Spain during the XII century and was particularly developed in Paterna and Manises, near Valencia, during the XIV and XV centuries. From Spain it arrived in the center of Italy, where it was exploited to produce the well-known polychrome luster Renaissance pottery of Deruta and Gubbio. This nanotechnology has been transferred in Italy from Mesopotamia in 700 years!! Luster preparation is described by Cipriano Piccolpasso in the second book of "I Tre libri dell'arte del vasaio", 1557. The copper/silver deposition was obtained by putting a mixture of copper and silver salts and oxides, together with vinegar, ochre, and clay, on the surface of a previously glazed pottery. Then the whole system was heated to about 600°C in a reducing atmosphere produced by the introduction of smoking substances in the kiln. In these conditions, metal ions were reduced to metal, that aggregated and remained trapped within the first layer of the glaze. The formation of nanoparticles (see the inset of fig. 23) is strongly analogous to that of the modern synthesis of metal-glass nanocomposites, consisting of ion-implantation [3], ion exchange, sol-gel [129] or sputtering deposition of ions in glass matrix, followed by annealing in reducing atmosphere.

Fig. 23. – Lustre prepared by Mastro Giorgio in Gubbio (Italy, 1528) (Museo Civico della Ceramica di Gubbio, Italy). The inset is a TEM image of copper nanoclusters in the gold lustre.

5˙4. *Pd-Ag and Pd-Cu alloys*. – After exploring the effect of Cu and Ag in Au-based alloys, we started a new set of experiments aimed at investigating the role played by Au, substituting it with Pd which, as Au, is not so reactive with either the matrix or oxygen [106]. Fused silica slides were sequentially implanted at room temperature with Pd (130 keV) and Ag (130 keV) or with Pd (130 keV) and Cu (90 keV) ions at the same dose of 3×10^{16} ions/cm^2 to obtain the same projected range as in the Au-based alloys. OD spectra for both systems are shown in fig. 24 do not evidence the Ag SPR peak at about 400 nm nor the Cu SPR peak at 560 nm, typical of the separated systems, respectively, suggesting the formation of metal alloy Pd-Ag and Pd-Cu nanoclusters. In this case the partially filled d-band of Pd promotes charge transfer with noble metals, with a subsequent damping of the collective plasma oscillation typical of free electrons like metals. The conclusion of actual alloy formation is supported by TEM analysis. The cross-section micrographs of the as-implanted and annealed Pd-Ag samples are shown in fig. 25. Selected area electron diffraction (SAED) indicates a dominant f.c.c. phase with a lattice constant $a = 0.3987(10)$ nm, consistent with the formation of an intermetallic alloy (experimental values for bulk f.c.c. Pd and Ag are $a_{\mathrm{Pd}} = 0.38898$ nm and $a_{\mathrm{Ag}} = 0.40862$ nm, respectively). After annealing in air at 800 °C

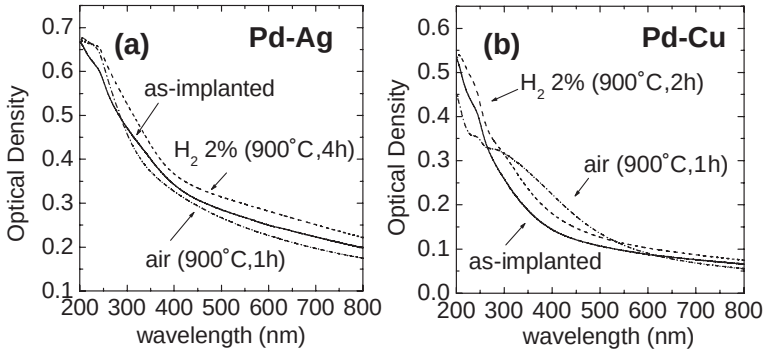

Fig. 24. – Effect of the annealing atmosphere on Pd-Ag and Pd-Cu alloys. (a) Optical absorption of sequentially ion implanted silica with Pd-Ag at the same dose 3×10^{16} ions/cm^2 (Pd3Ag3) and annealed at 900C in air or in reducing atmosphere. (b) Optical absorption of sequentially ion implanted silica with Pd-Cu at the same dose 3×10^{16} ions/cm^2 (Pd3Cu3) and annealed at 900 °C in air or in reducing atmosphere.

for 5 hours (fig. 25), SAED analysis evidenced an f.c.c. phase with a lattice parameter $a = 0.3946(10)$ nm, corresponding to a value of $x = 0.71(3)$, indicating a loss of silver, as already observed in silica samples, containing silver nanoclusters, prepared by sol-gel method [118]. The average PdAg nanocluster diameter after air-annealing increased to a value of 8.4±5.8 nm. The cluster size evolution may be interpreted in terms of size-related thermodynamic instability [68], with a transfer of atoms from smaller to larger clusters

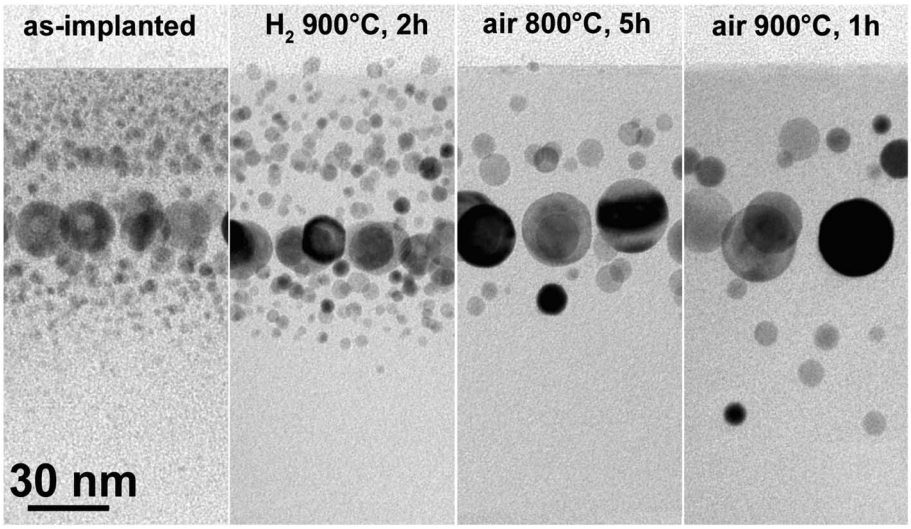

Fig. 25. – Cross-sectional bright-field TEM images of sequentially ion implanted silica with Pd (130 keV) and Ag (130 keV) at the same dose 3×10^{16} ions/cm^2: (a) as implanted; (b) annealed in reducing atmosphere at 900C for 2 hours; (c) annealed in air at 800 °C for 5 hours; (d) annealed in air at 900 °C for 1 hours.

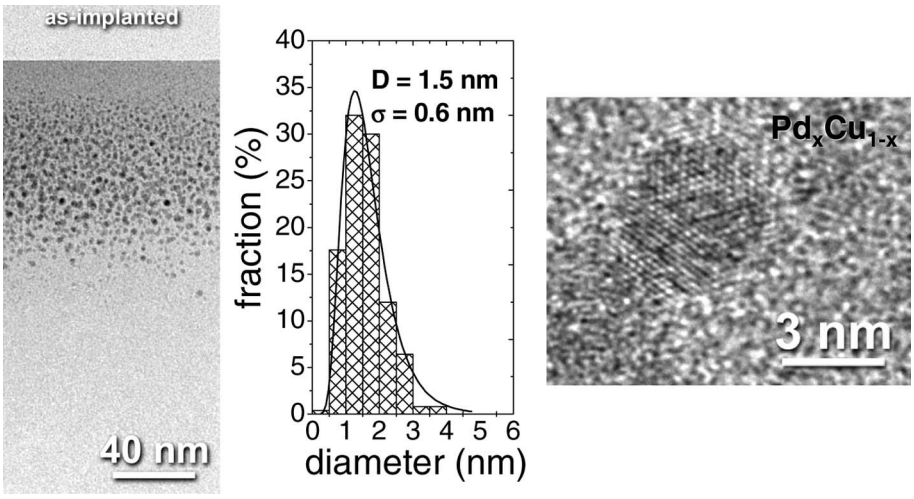

Fig. 26. – (Left panel) cross-sectional bright-field TEM images of sequentially Pd-Cu ion implanted SiO_2 and (central panel) histogram of size distribution; (right panel) high-resolution TEM image of an alloy PdCu cluster.

(coarsening). After annealing in reducing atmosphere (H_2-N_2 mixture), the composite exhibits a morphology similar to the as-implanted sample. Cluster average size is slightly larger (4.4 ± 3.4 nm), with an enrichment of Pd in the alloy cluster composition, as indicated by diffraction analysis.

Similarly to the Pd-Ag case, also in Pd-Cu sequentially implanted samples, alloy nanoclusters are observed either in the as-implanted or in the H_2-N_2 annealed samples, with a remarkably different size distribution. Cross-sectional bright-field TEM analysis on the as-implanted PdCu sample is shown in fig. 26.

The image shows small spherical clusters with average size $D = 1.5$ nm and standard deviation of the experimental distribution $\sigma = 0.6$ nm. The electron diffraction analysis (SAED) shows the presence of an f.c.c. alloy with a lattice parameter $a = 0.3824(14)$ nm. For comparison, the lattice parameters of the bulk f.c.c. metallic phases are $a_{\mathrm{Pd}} = 0.3891$ nm and $a_{\mathrm{Cu}} = 0.3615$ nm, respectively. Therefore, assuming a Vegard-like (linear) evolution of the lattice parameter of the alloy as a function of the Cu concentration, x, as $a_{\mathrm{alloy}} = x a_{\mathrm{Cu}} + (1 - x) a_{\mathrm{Pd}}$, the SAED result can be interpreted as the formation of a PdCu alloy with a Cu fraction of $x = 0.25 \pm 0.05$, which corresponds to a Pd/Cu atomic ratio of $\alpha = 3.0 \pm 0.1$. On the other hand, the EDS compositional quantification, taken on the whole implanted region, gives an overall Pd/Cu atomic ratio of $\alpha = 1.3 \pm 0.1$. Therefore, the comparison between SAED and EDS measurements indicates that there is a fraction of Cu atoms, which do not participate to the PdCu alloy and remain dispersed in the matrix or oxidized. The same behavior was observed in similar samples obtained by sequential ion implantation of Au and Cu in silica [24, 25]. The TEM results have been confirmed by EXAFS analysis.

To reduce the number of dispersed or oxidized Cu atoms, an annealing at $T = 900\,^{\circ}\mathrm{C}$ in reducing atmosphere was performed. The result is twofold: morphological and compositional. Morphologically, the average cluster size is increased to $D = 9.8$ nm (with size dispersion $\sigma = 9.5$ nm) by annealing at $900\,^{\circ}\mathrm{C}$ for 2 h, as shown in fig. 27(a). Moreover,

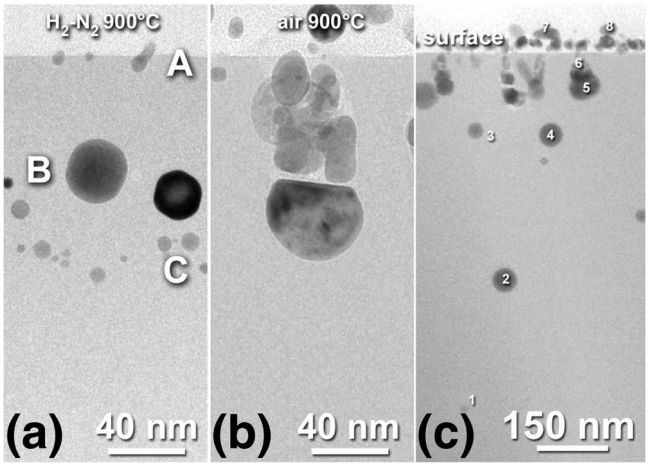

cluster #	depth (nm)	α=Pd/Cu atomic ratio
1	780	8.2 ± 0.6
2	500	10.5 ± 0.7
3	170	11.8 ± 0.8
4	180	10.2 ± 0.7
5	75	14.7 ± 1.0
6	40	1.1 ± 0.1
7	out	0.7 ± 0.1
8	out	0.4 ± 0.1

Fig. 27. – Cross-sectional bright-field TEM images of sequentially Pd-Cu ion implanted SiO_2: (a) after annealing at 900 °C in H_2(2%)-N_2, 2h; (b) after annealing at 900 °C in air, 1 h; (c) same as (b) at lower magnification (the numbers label some of the clusters probed by EDS as reported in the table aside (the cluster numbers and the depths refer to (c). "out" indicates clusters on the sample surface.)

as far as the in-depth distribution of clusters is concerned, a three-layer arrangement is obtained: one layer at the sample surface (labelled A), one at the implantation projected range R_P at about 70 nm (B) and one at 1.5–2 times the R_P (C). Compositional analysis with a focused electron beam of 5 nm FWHM on single clusters by EDS indicates that the average cluster composition gives a Pd/Cu atomic ratio of $\alpha_{\rm sup} = 3.1 \pm 0.5$ in the surface layer (A), $\alpha_{R_P} = 1.4 \pm 0.1$ in the layer at R_P (B), and $\alpha_{\rm deep} = 0.8 \pm 0.2$ in the deepest layer (C). This indicates that upon annealing in reducing atmosphere there is a preferential migration of Pd atoms toward the sample surface, along with an opposite (less pronounced) diffusion toward the sample bulk, which is correlated to a diffusion of Cu atoms, as already found for Au-Cu alloy nanoclusters in silica [48]. As for Pd-Ag system, annealing in oxidizing atmosphere gives rise to an alloy decomposition faster than in the H_2-N_2 annealed samples, as already observed in the case of AuCu alloy nanoclusters [24], and with the migration of Cu atoms towards the surface [106]. The effect of oxidizing atmosphere on the clusters composition has been investigated by annealing the as-implanted sample at 900 °C in air for 1 hour. The cross-sectional TEM images of the resulting sample are shown in fig. 27(b,c). The most evident result is that air annealing promotes the diffusion of the dopant species either toward the surface or the bulk, with two effects: i) a partial out-diffusion of the metallic species (which form clusters just on the sample surface); ii) the formation of alloy nanoclusters well beyond the implantation range (some clusters are found at a depth of about 800 nm from the sample surface, as shown in the low-magnification TEM image of fig. 27(c)). The morphology of the clusters near the projected range (see fig. 27(b)) is quite complex due to a strong rearrangement of the clusters composition. This resulted in the formation of clusters, whose surface is no longer spherical or is strongly faceted. Extensive high-resolution (HRTEM) investigation showed in some clusters the presence of a partial core-shell structure. For instance, it is possible to identify a core of the cluster made by Pd (the measured interplanar spacings are 0.195±0.020 nm and 0.138 ± 0.020 nm as for the {200} and {220}

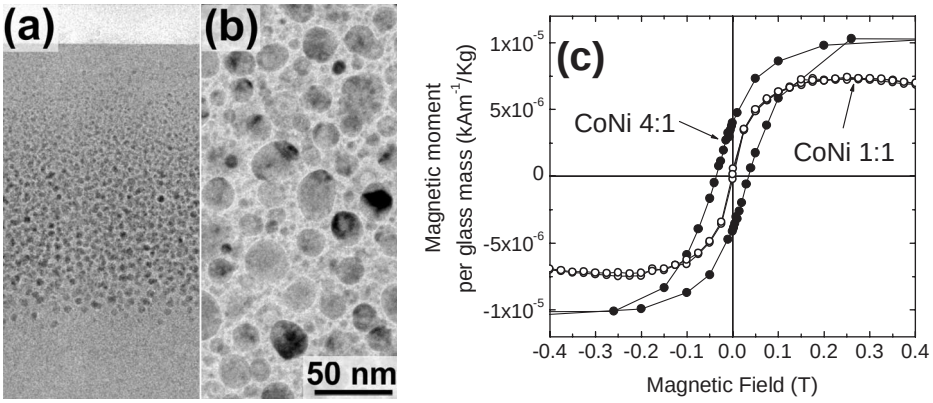

Fig. 28. – (a) Cross-sectional bright-field TEM image of sequentially ion implanted silica with Co and Ni with a concentratio ratio of 4:1 for a total dose 30×10^{16} ions/cm^2; (b) planar bright-field TEM image of sequentially ion implanted silica with Co and Ni with a concentratio ratio of 1:1 for a total dose 40×10^{16} ions/cm^2; (c) comparison between the room temperature hysteresis loop of f.c.c. Co1Ni1 and h.c.p. Co4Ni1 samples.

planes of f.c.c. Pd) surrounded by a thin shell of CuO (with measured interplanar spacings of 0.233 ± 0.020 nm and of 0.160 ± 0.020 nm as for the $\{111\}$ and $\{\bar{2}02\}$ planes, respectively, of monoclinic CuO). It is interesting to note that similar samples made by Au+Cu sequential implantation showed upon air annealing the formation of a similar partial core-shell structure in which an Au-enriched core was partially surrounded by Cu_2O (cubic) with a coherent arrangement of the two lattices [48]. The different oxidation state of copper was explained by the crystallographic-assisted stabilization of the cubic phase coherently with the cubic f.c.c. metallic phase. In the present case this kind of stabilization is no longer possible due to the large lattice mismatch (about 9%) between the cubic Cu_2O and f.c.c. Pd therefore resulting in the formation of CuO. In order to quantify the compositional evolution of the clusters as a function of the depth, an EDS analysis on single and isolated clusters has been done. The results are shown in the table in fig. 27 where the numbers refer to the clusters labelled in fig. 27(c): the Pd/Cu atomic ratio is about 10 for clusters down to 800 nm from the surface and less than one for clusters on the sample surface. This indicates that there is a preferential out-diffusion of Cu atoms from the sample along with an in-depth correlated diffusion with Pd.

In conclusion, we have investigated the dynamics of the compositional and structural evolution of solid solution Pd-Cu metal nanoclusters, obtained by sequential ion implantation in silica, upon heating in selected atmospheres. The most relevant results obtained are: i) the tendency to a correlated diffusion of the dopants triggered by Cu atoms either during reducing or oxidizing annealing; ii) the dynamics of Cu extraction from the alloy nanoclusters by incoming oxygen atoms with the progressive Cu oxidation and the resulting formation of CuO oxide arranged in thin defective and incomplete shells around Pd-rich cores. In particular, a comparison between this last result and that obtained for Au-Cu clusters in silica (whose oxidation lead to the formation of Au-rich cluster partially surrounded by Cu_2O) suggests that the structural constraint given by the lattice mismatch between core and shell is crucial to control the stoichiometry of the oxide shell.

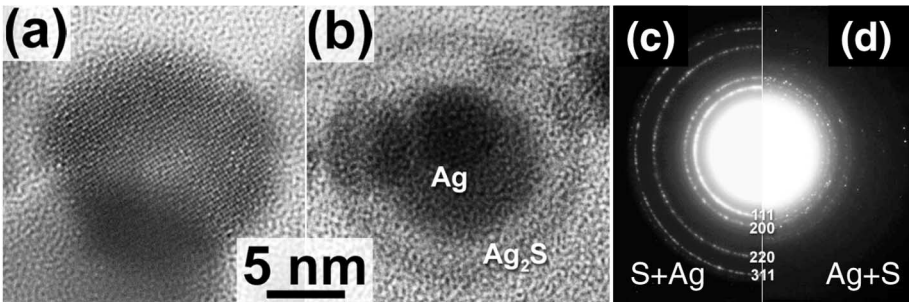

Fig. 29. – Cross-sectional TEM images of a silica sample implanted with Ag and S: (a) high-resolution image showing the lattice planes of the Ag_2S shell; (b) bright-field showing the contrast between the Ag core and the Ag_2S shell; (c) and (d) are the diffraction pattern of the sample sequentially implanted with S+Ag and with Ag+S, respectively.

5˙5. *Co-Ni alloy.* – As an example of binary clusters for magnetic application, we have investigated the Co-Ni phase diagram by performing sequential ion implantation in silica of Co and Ni at the same energy of 180 keV ($R_p \sim 150$ nm) but with different doses in order to have a constant total Co+Ni dose (15×10^{16} ions/cm^2 or 30×10^{16} ions/cm^2). For the 1:1 Co:Ni ratio, we performed also sequential implants at two energies (180 keV and 70 keV) for each element to have a flatter concentration profile for a total dose of 40×10^{16} ions/cm^2 (sample CoNi40) [58]. All the samples investigated exhibit Co_xNi_{1-x} alloy nanoclusters. In this case OD spectra are not useful for alloying detection due to the above-mentioned damping of the SPR due to interband transitions [40]. SAED analysis was able to monitor a phase transition from f.c.c. to h.c.p. as the Co content in the system is greater than 70%, in agreement with bulk CoNi alloy. It is interesting to note that similar CoNi alloy system obtained by our group with the sol-gel route, exhibited at all the CoNi ratios the f.c.c. structure [130]. As the lattice parameters of the f.c.c. phases of Co and Ni differ by a quantity that is at the limit of SAED quantification for nanoclustered systems (mostly due to the size-dependent broadening of the diffraction peaks), we performed also EDS compositional analysis with a sub-nanometer electron probe on single clusters which demonstrated the presence of both Co and Ni on single clusters.

Figure 28a shows a TEM image of the Co4Ni1 sample whereas fig. 28b is a TEM image of the CoNi sample (implanted at a total dose 40×10^{16} ions/cm^2): the SAED pattern for CoNi sample exhibits a single alloy f.c.c. phase with lattice parameter $a = 0.3533(12)$ nm, whereas, when the Co concentration in the alloy is increased above 70%, an h.c.p. diffraction pattern is obtained. The difference in structure as a function of the Co contents in the alloy is of paramount importance for controlling the magnetic properties. In fig. 28c the hysteresis loop of f.c.c. Co1Ni1 and h.c.p. Co4Ni1 samples (at the same total dose) are compared: the average cluster size in both samples is similar (about 5 nm [57]) but the h.c.p. phase (Co4Ni1) exhibits a coercive field which is absent in the f.c.c. phase (Co1Ni1). This is due to the reduction in symmetry of the hexagonal unit cell with respect to the cubic one.

5˙6. *Ag-S core-shell system.* – In some cases, sequential ion implantation gives rise to "mixed" clusters, in the sense that both elements are present on the same cluster but each one maintaining its structure in a core-shell arrangement. Fused silica slides

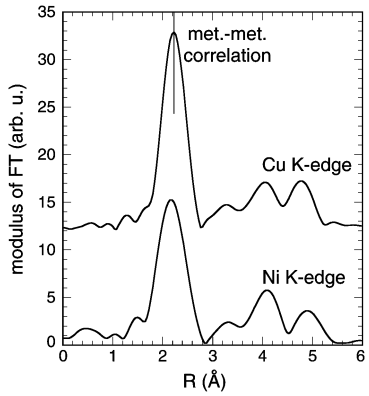

Fig. 30. – Moduli of the Fourier transforms of k^3-weighted spectra of the Cu+Ni implanted sample, measured at Cu and Ni K-edges. The transformation range is $k = 3$–13 Å^{-1}.

were sequentially implanted at room temperature with Ag (65 keV) and S (30 keV) ions at a dose of 5×10^{16} ions/cm^2 and 2×10^{16} ions/cm^2, respectively, to obtain the same projected range of about 40 nm [109]. In fig. 29a a high-resolution TEM image shows the lattice fringes arising from the shell made of Ag_2S in the acanthite form superimposed on the core composed of Ag. In fig. 29b a bright-field view of the sample implanted first with Ag and then with S ions shows a spherical core-shell cluster with a clear contrast between the Ag core and the Ag_2S shell. It is interesting to note that no mixed clusters are obtained upon reversing the implantation order: performing first S and then Ag implantation (S-Ag sample), only Ag clusters are detected while S takes part to the formation of thiosilicate species [109]. This can be seen in fig. 29c,d which compare the SAED electronic diffraction of the two samples: fig. 29c shows an f.c.c. pattern of silver nanoclusters in the S-Ag sample, whereas fig. 29d shows both the f.c.c. reflections of Ag nanoclusters and the monoclinic one of the Ag_2S shell.

5˙7. *Cu-Ni alloy.* – Cu-Ni alloy nanostructure formation was investigated by implanting Cu and Ni ions into silica slides. The dose was 6×10^{16} ions/cm^2 for each element, while the implantation energy was 90 keV for Cu and 100 keV for Ni.

EXAFS spectroscopy was performed to investigate the local order around the implanted atoms. In fig. 30 are represented the k^3-weighted Fourier transform moduli of the EXAFS spectra recorded for the double-implanted sample for both Cu and Ni K-edges; the peaks at about 2.2 Å correspond to the metal-metal correlation, while the signals centered at about 1.5 Å are due to the metal-oxygen coordination. This is explained by assuming the coexistence of a metallic cluster phase and an oxidized phase, consisting of copper (nickel) ions at the cluster/glass interface and/or dispersed in the glass matrix [53]. The calculated metal-metal nearest-neighbor distance was 2.52 Å, for both Cu and Ni K-edge measurements [53, 54]. The distance corresponds in the f.c.c. phase to the lattice parameter of 3.56 Å, in between those of the two metal phases, indicating the formation of a CuNi alloy phase (almost 1:1 Cu/Ni ratio). This finding is supported by GIXRD analysis on this sample [53], that indicates the presence of randomly-oriented f.c.c. nanoclusters, whose measured lattice parameter is 3.565 ± 0.01 nm, confirming the alloy formation.

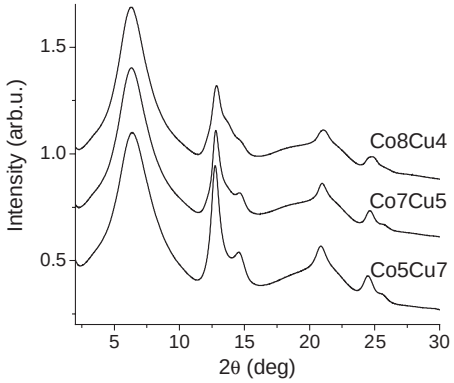

Fig. 31. – Radially integrated diffraction profiles from the Co+Cu-implanted samples as a function of the scattering angle (the X-ray beam energy was 27 keV). Besides the matrix contribution (evident in the peak at $2\theta \simeq 7$ deg), the reflections from the cluster crystalline structure are clearly visible.

5˙8. *Co-Cu alloy*. – The sequential ion implantation of Cu+Co ions is particularly interesting for the possibility of obtaining Co-Cu alloy nanoclusters, despite their immiscibility in the bulk phase in the concentration range used in our study as described below. In fact, the Co-Cu alloy can be only produced by non-equilibrium techniques [131]. For example, Childress and Chien [132] prepared Co-Cu alloys in the whole composition range by dc-sputtering and studied the magnetic diagram phase showing spin-glass, ferromagnetic and paramagnetic phases, while Noetzel *et al.* [133] have obtained Co/Cu solid solution by implanting up to 25% of Co in Cu targets. Indeed, the Co-Cu bulk alloys can present different magnetic behavior depending on the concentration of the ferromagnetic species. The use of ion implantation in particular gives rise to very thin layers in which different local situations can occur due to the non-equilibrium nature of this process. Co^+ and Cu^+ ions were sequentially implanted at room temperature into fused silica, at energies of either 90 or 180 keV, with projected ranges overlapping for each pair of implants; the total dose was 1.2×10^{17} ions/cm^2 for the doubly implanted samples (Cu+Co and Co+Cu).

An EXAFS analysis was first performed to detect the relative presence of metal-metal and metal-oxygen coordination. In particular, a preliminary investigation by 4-shell fits of EXAFS spectra shows that the percentage of dopant atoms that aggregate in clusters is not lower than 60%. The results from fitting procedures of the first shell indicate that the intermetallic distances are the Co bulk ones for Co-metal correlation [60]. On the other hand, the values obtained for Cu-metal correlation suggest a shortening of the distance, possibly induced by the presence of Cu-rich alloy clusters thus having structural characteristics different from pure metal. In the case of the Cu6Co6 sample, the Co-O coordination distance (1.98 ± 0.02 Å) was shorter than the corresponding one in CoO (2.13 ± 0.01 Å, from EXAFS analysis). This behavior was also observed in similar systems obtained by sequential implantation of Cu and Ni ions [53].

Figure 31 reports the radially integrated profiles from GIXRD scattering patterns in the case of CoCu implanted samples: in addition to the first peak, due to the silica substrate [134], a signal from crystalline clusters is clearly visible. Starting from the h.c.p. order of Co nanoclusters, increasing the relative amount of copper in the total

amount of implanted metal (Co+Cu) leads to the progressively increasing peak heights associated with an f.c.c. crystalline structure. Cobalt aggregates in h.c.p. nanocrystals if introduced in the matrix by ion implantation, while Cu does so in f.c.c. structures [53]. On the other hand, following ref. [132], a CoCu alloy has an f.c.c. structure at up to 80% cobalt. The features observed in fig. 31, supported by EXAFS results, suggest that by sequential implantation of Co+Cu two family of nanocrystals are formed: one of Co h.c.p. nanocrystals and the other of Cu-rich crystalline nanoclusters. No oxides are detected.

5˙9. *Conclusions*. – Sequential ion implantation, as a technique for the synthesis of "mixed" (alloyed or core-shell) clusters, has been illustrated with some case studies involving either metallic or semiconducting systems. This technique is able to give in a large variety of systems direct alloying: subsequent thermal annealing can be used to modify either the clusters size distribution or the alloy composition, due to the selective interaction of the annealing atmosphere with the alloy components. In particular, we demonstrated that annealing in oxidising atmosphere is more effective in the alloy decomposition with respect to annealing performed in reducing or inert atmospheres. The rich phenomenology gained in these complex systems will hopefully give a valuable contribution to the comprehension of the mechanisms responsible for alloy formation and stability. As a last remark we would like to stress the fact that the implantation order of the two elements can have a relevant influence in the resulting nanophase mostly when one of the two elements has a higher chemical affinity with the atoms in the matrix.

6. – Ion beam processing

Ion implantation can be used not only to dope a substrate with the implanted ions but also to release energy to the target in a controlled way in order to promote nucleation and growth of elements already present in the implanted substrate. Modification of the substrate structure can be done by ion-beam mixing experiments, in which an energetic heavy-mass ion beam (*i.e.* Au ions in the MeV energy range) promotes modification of a metallic layered structure embedded in glass up to nanocluster formation [135, 136] in a sort of top-down synthesis approach in which ion beam "sculpture" of a bulk-like structure is performed until the formation of the nano-building blocks (the nanoclusters) is obtained. In this approach the nuclear component of the energy loss S_n is the dominant mechanism to control the final nanostructure. An alternative method is based on irradiation with low-mass ions, in which the inelastic energy transferred by electronic interaction is responsible for the precipitation of nanostructures.

6˙1. *Ion-beam–induced cluster precipitation*. – A prototype of this last kind of approach involves a glass containing a metal oxide: irradiating the glass with low-mass ions (He, for instance) or protons, the electronic component of the stopping power S_e (which is the dominant mechanism of energy loss in such irradiations, see fig. 2) triggers metal clusters precipitaton due to the energy inelastically transferred to the system [44, 114, 137, 138, 9]. The metal oxide can be introduced in the glass either during its thermal synthesis (as in ref. [9] in which 0.08 wt% Cu_2O oxide was present inside a soda-lime glass) or it can be obtained by an intermediate step which involves ion-exchange between alkali ions inside the glass with the noble-metal ions (as in refs. [114, 137] in which $Na^+ \rightleftharpoons Ag^+$ ion exchange is performed in a soda-lime glass). As regards this last approach, the technique of ion-exchange is very effective in doping much thicker layers with respect to ion implantation: few microns thick optical waveguides can, for instance, be easily

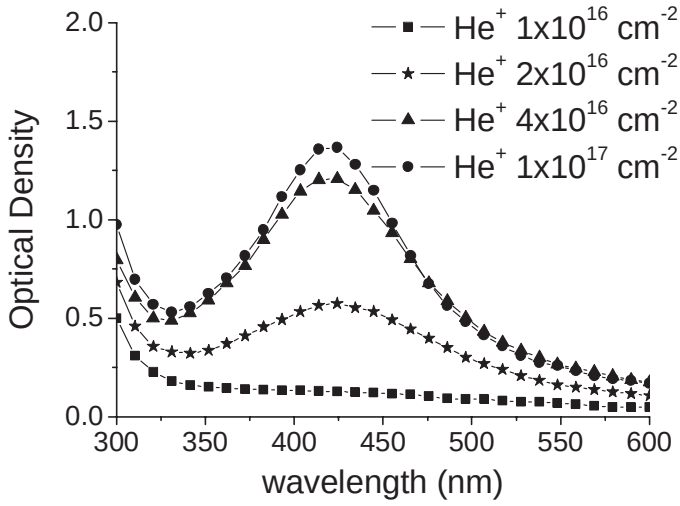

Fig. 32. – Optical absorption of 100 keV He^+ irradiated Ag-exchanged soda-lime glass as a function of the irradiation fluence.

obtained with an increase of the linear refractive index useful to confine the light within the modified layer.

As an example in fig. 32, the evolution of the optical absorption is shown for Ag^+-exchanged soda-lime glass after room temperature irradiation with 100 keV He^+ ions. The samples were obtained as follows: a soda-lime glass of composition (wt%): 71.9 SiO_2, 1.9 Al_2O_3, 6.8 CaO, 1.1 K_2O, 4.4 MgO, 13.5 Na_2O, 0.4 SO_2, with small contaminations of iron (1.5 ppm) and arsenic (300 p.p.m.) was preheated and immersed for 30 min in a molten salt bath of molar concentration 0.1% $AgNO_3$ in $NaNO_3$ at 320 °C. Irradiations of the exchanged samples were performed using He^+, Li^+ and Ne^+ ions at the energy of 100 keV. The current densities were in the 1–8 $\mu A/cm^2$ range. The ion fluence was 2×10^{16} ions/cm^2, except for helium which was implanted at fluences in the range 1×10^{16} ions/cm^2–1×10^{17} ions/cm^2. For comparison, different sets of samples were irradiated at room temperature (RT), 90, 150 and 250°C.

From fig. 32 it is clear that upon increasing the He^+ irradiation fluence the SPR absorption band centered at about 410 nm is more and more evident: this is due to the precipitation of spherical Ag nanoclusters in the irradiated region (the projected range for 100 keV he^+ ions in a soda-lime glass is $R_P = 640$ nm and the straggling $\Delta R_P = 110$ nm). RBS measurements indicated that no remarkable difference can be found in the silver concentration profile before and after the irradiation at room temperature: this indicates that the nanocluster nucleation occurred uniformly in the whole irradiated volume. When the irradiations are performed at higher substrate temperatures more complex diffusive phenomena come into play with also a strong rearrangement of the silver profile inside the samples [137]. The role played by the different ion species is also important: in fact, in the case of lithium irradiation, the absorption band for substrate temperatures of 90 and 150 °C is more intense than for the helium-irradiated specimens. Since only the collisional part of the energy deposited in the sample by the incident beam is appreciably different in the two irradiations, we can infer that the higher radiation damage caused by the lithium ions favours, in this intermediate temperature range, the migration and aggregation of

silver atoms. Finally, in the case of neon irradiation, the intensity of the absorption band is much less for all temperatures, and its full-width at half-maximum (FWHM) is less than that corresponding to the helium- and lithium-irradiated samples. In this case, bigger clusters at lower concentration should have been formed. It is possible that, above a certain value of the energy deposited in elastic collisions (S_n is much higher for neon than for helium and lithium), already formed silver precipitates dissolve in the collision cascade along the ion track, consequently decreasing their equilibrium concentration. Moreover, because of the small mean projected range ($R_P = 190$ nm and the straggling $\Delta R_P = 55$ nm), the neon-irradiation–induced clusters are formed in a thinner surface region.

These results indicate that by combining ion-exchange and ion implantation techniques, it is possible to induce and control the formation of silver clusters, of nanometer size, within light waveguiding structures. By the use of low-mass ion beams, we obtained modified layers deeper than those possible with direct metal-ion, implantation using the most widely available low energy (hundreds of keV) ion implanters. Moreover, low fluences are necessary, with a consequent low damage level of the resulting optical structure. We have also shown that the temperature of the substrate during irradiation plays an important role. It is worth mentioning that these samples exhibit interesting values of the nonlinear refractive index n_2 confirming that the proposed methodology has a potential for the fabrication of non-linear optical devices.

Recently, we have applied this technique to control the precipitation of Ag nanoclusters in sol-gel synthesized Er-doped glass for controlling the energy transfer between metallic sensitizers (Ag nanoclusters) and rare earths [139, 26].

In the past few years, erbium-doped materials gained much attention in the field of optical communications, since the Er^{3+} ion shows a broad optical emission at 1540 nm, within the main wavelengths window in the telecommunication technology. Erbium-doped optical waveguides have therefore received growing interest due to their multiple applications, for example in integrated lasers or amplifiers for telecommunications. One of the major limits to the application of rare-earth–doped glasses as optical amplifiers or solid-state lasers is related to the small absorption cross-sections of rare-earth ions. To increase the Er^{3+} pumping efficiency many solutions have been investigated, such as codoping with other rare earths like Yb [140] or by introducing broad-band sensitizer species like organic complexes, Si nanocrystals [141, 142] and metals [143, 144, 26, 145]. However, the mechanism that controls the enhancement of the Er^{3+} photoluminescence is still under debate. Regarding the silver sensitizing effects, it is not clear if the enhancement is due to the presence of silver clusters or to defects related to a pair of silver ions/atoms. Sol-gel is a very convenient technique for the fabrication of high-quality thin glass films and it is of great interest for industrial fabrication because of its low-cost availability and batch processing. Erbium-doped waveguides based on silica, silica-titania or phosphate glasses have been prepared with this technique. Channel waveguides have been fabricated by ion exchange which represents probably the most simple way to obtain the lateral confinement. The introduction of silver as erbium sensitizer in the film was obtained by ion-exchanging Er-doped SiO_2-Al_2O_3-Na_2O sol-gel films. The films were subsequently annealed under controlled atmosphere to induce the migration and aggregation of the metal ions.

Thermal annealing of the as-exchanged samples (500 °C in N_2 atmosphere) increases the Er photoluminescence by pumping the system with a Ar laser in (at $\lambda = 488$ nm) and out of resonance (at $\lambda = 476.5$ nm) with the absorption lines of Er. This can be assumed as a fingerprint of the energy transfer to rare-earth ions mediated by Ag-related species.

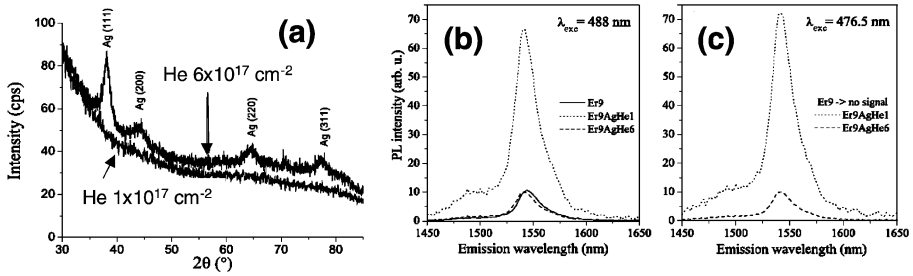

Fig. 33. – (a) GIXRD diffractograms for the Ag-Er codoped sol-gel glass after 190 keV He^+ irradiation at 1×10^{17} ions/cm^2 and 6×10^{17} ions/cm^2. (b) In-resonance and (c) out-of-resonance Er^{3+} photoluminescence at 1.5 μm after He irradiations.

The use of He^+ irradiation in the annealed samples was used to demonstrate that large nanoclusters are not the best sensitizing form of metallic Ag. On the contrary the best performance in terms of the photoluminesce enhancement is obtained when Ag is in the form of multimers with size near or below 1 nm at most. This can be seen in fig. 33a which shows the GIXRD pattern of the Ag-Er codoped sample thermally annealed and irradiated with 190 keV He^+ at 1×10^{17} ions/cm^2 and 6×10^{17} ions/cm^2. Only upon high fluence irradiation the amount of inelastic electronic energy loss is able to promote extensive Ag precipitation, showed by the f.c.c. Ag reflections, whereas in the low dose irradiation no diffraction peaks are detected, indicating that the Ag nanoclusters are so small that the diffraction peaks are extremely broadened by the size effect. Correspondingly in the high dose irradiation there is a dramatic decrease of the energy transfer efficiency in and out of resonance (fig. 33b and fig. 33c, respectively) as compared to the low dose irradiation. This result demonstrates that small Ag nanoclusters behaves as more efficient sensitizers for Er photoluminescence.

Promising results have been obtained in the energy transfer between metal nanostructures to erbium ions, implanting in silica matrix Er and Ag or Au ions. After a thermal annealing at about 600 °C energy transfer efficiency in and out resonance is evidenced. Such result has been correlated to the formation of metal nanostructured systems, as discussed previously for Er-doped sol-gel films. Increasing the annealing temperature a cluster growth and a decrease in the energy transfer process are evident.

6˙2. *Ion-beam–induced cluster modification.* – With respect to the monoelemental case, when dealing with bimetallic nanoclusters one has an additional parameter to play with for controlling NCs properties, *i.e.* the composition. Of course, before the "tunability" of the NCs properties can be used for actual devices, a careful control over alloy clusters synthesis and stability has to be achieved, in order to clarify which are the parameters (*i.e.* implantation conditions, subsequent thermal or laser annealings, ion irradiation, etc.) that can promote separation (via oxidation, for instance) instead of alloying of the implanted species. As we have seen in the previous sections, among different possible synthesis processings, ion-beam–based techniques proved to be very suitable in synthesizing NC-containing glasses [69, 45, 146, 147, 19, 20, 148, 9]. Moreover, the composition of the clusters can be varied easily by sequential ion implantation in the matrix of two different elements, whose energy and dose can be tailored so as to maximize the overlap between the implanted species and to control their local relative concentration.

6˙2.1. Au-Cu alloy clusters. In this subsection we present two possible paths for promoting an elemental-selective de-alloying in bimetallic Au_xCu_{1-x} nanoclusters [48]: the first one is controlled by the post-implantation thermal annealing, the latter is triggered by the nuclear component of the energy released to the cluster by a suitable ion beam. As we will see, both methodologies can be exploited for making an elemental-selective de-alloying.

De-alloying is usually described in terms of corrosion, as a selective dissolution of the most electro-chemically active element of the alloy [149]. This process results in the formation of a nanoporous structure composed almost entirely of the more noble alloy constituent. As a room temperature (RT) process, dealloying is mainly assisted by the formation and migration of divacancies, which are known to diffuse faster than single vacancies at RT [150]. We will show that we can obtain also the inversion of this path (which is followed under chemically-driven de-alloying), therefore extracting preferentially the more noble metal (Au, in our case) from the alloy.

Fused silica (Type II, Heraeus) slides were sequentially implanted with Au^+ and Cu^+ ions at room temperature at a current density of 2 $\mu A/cm^2$, ion energies of 190 keV for Au and 90 keV for Cu and doses of 3×10^{16} ions/cm^2 for both ions. Implanted slides were then heat-treated in a conventional furnace at 900 °C temperature in a $H_2(4\%)$-N_2 atmosphere. This is the reference sample, in the following labeled as Au3Cu3H. Thermal annealing in air at 900 °C in a conventional furnace was performed for increasing time intervals, from 15 min upto 5 h. The reference samples were also ion-irradiated with 190 keV Ne ions at a dose of 1×10^{17} ions/cm^2 and 2 $\mu A/cm^2$ of current density (with these irradiation conditions we measured a temperature increase lower than 50 °C in the sample, therefore ruling out a major effect of the temperature).

In subsect. **5˙1**, we found that upon annealing in reducing atmosphere Au_xCu_{1-x} alloy nanoclusters, formed after sequential ion implantation, change their composition and grow, because of the Cu atoms (initially oxidized and dispersed in the matrix) reduced and incorporated in the clusters upon annealing, resulting in a $Au_{0.5}Cu_{0.5}$ final composition [24]. We used those results to obtain relatively large Au_xCu_{1-x} alloy nanoclusters with negligible amount of oxidized Cu. The size distribution of the clusters in these reference samples exhibits an average diameter $\langle D\rangle = 13.8$ nm and a standard deviation of the experimental bimodal distribution $\sigma = 11.7$ nm. An additional feature of the reference samples is the topological distribution of the clusters. As can be seen in fig. 34(a), three distinct layers of well-separated spherical clusters are present: one at the surface, one at the projected range of the original sequential implantation (about 70 nm), and one at a depth of about 200 nm, *i.e.* the end of implantation damage [151].

A first attempt of obtaining a selective de-alloying was carried out with thermal annealing in oxidising (air) atmosphere. The TEM cross-sectional bright-field micrographs of the sample Au3Cu3H is shown in fig. 34(a) and (b), before and after a thermal annealing in air at 900 °C for 15 min, respectively. The effect of the annealing is to extract Cu as Cu_2O (cuprite, cubic, $a = 0.4267$ nm) as a first step. Cu_2O is stabilized by the crystallographic cubic template of the Au_xCu_{1-x} alloy, as can be seen from the selected area electron diffraction (SAED) pattern obtained from the area indicated by the dashed circle in fig. 34(c). In this image couples of "twin spots" aligned in the radial direction indicate two coherent cubic phases with the crystallographic axes aligned, which can be indexed as an Au-rich Au_xCu_{1-x} alloy ($x \sim 0.9$) and Cu_2O (in fig. 34(d) the powder diffraction spectra of both phases are compared). Further evidence of this interpenetrated structure can be obtained by EDS analysis. Scanning a 8 nm focused electron beam on different areas of the twofold clusters indicated by arrows in fig. 34(b) a com-

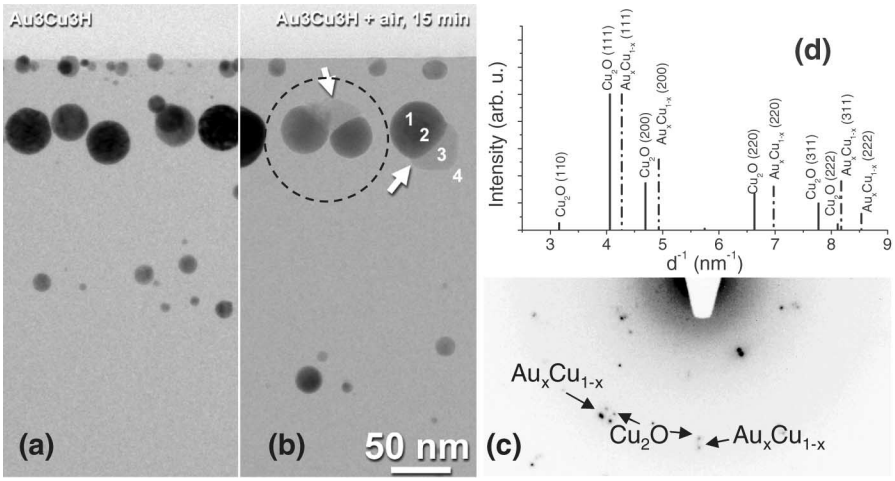

Fig. 34. – Bright-field TEM cross-sectional micrograph of the sample Au3Cu3H (annealing in $H_2(4\%)$-N_2 atmosphere at 900 °C for 1 h) before (a) and after a thermal annealing in air at 900 °C for 15 min (b). The arrows indicate some of the twofold clusters made of a Au-enriched alloy and out-coming Cu_2O; (c) SAED diffraction pattern from the circular region of part (b); (d) simulation of the diffraction pattern from Au_xCu_{1-x} alloy ($a = 0.406$ nm) and cubic Cu_2O in the cuprite phase ($a = 0.4267$ nm).

positional variation across the cluster has been obtained as reported in table V for the four points labeled in fig. 34(b). We underline that the heat of formation of Cu_2O is about 167 ± 20 kJ/mole [152] to be compared to the corresponding value of AuCu alloy, 5.3 ± 0.5 kJ/mole.

It is interesting to note that if the annealing time interval is increased upto 5 h an asymptotic equilibrium is reached in which all the Cu atoms are extracted from the alloy and are driven at the sample surface where they are oxidised in large polycrystalline clusters of CuO [111] (tenorite, monoclinic, the most stable copper oxide), as discussed in subsect. **5**˙1. Therefore, as far as the thermal oxidation is concerned, the de-alloying path follows a pattern similar to the corrosion process [149], in which the less noble (and more reactive element) is extracted from the alloy.

We can reverse this path by performing an irradiation of the alloy clusters with Ne ions at 190 keV [48]. The irradiation conditions were chosen to avoid overlap of the implanted Ne atoms with the already formed clusters: the R_P of the Ne ions is indeed about 410 nm with a straggling of about 100 nm as simulated by SRIM. Therefore irradiating atoms

TABLE V. – *EDS compositional analysis at AuL and CuK edges on the sample annealed in air at* 900 °*C for* 15 *min. The zones are labeled as in fig.* 34.

Zone	Au/Cu	Phase	x
1	10.5 ± 0.3	Au_xCu_{1-x}	0.90 ± 0.06
2	2.0 ± 0.1	Au_xCu_{1-x}	0.66 ± 0.06
3	0 (only Cu)	Cu_2O	-
4	0 (no Au or Cu)	SiO_2	-

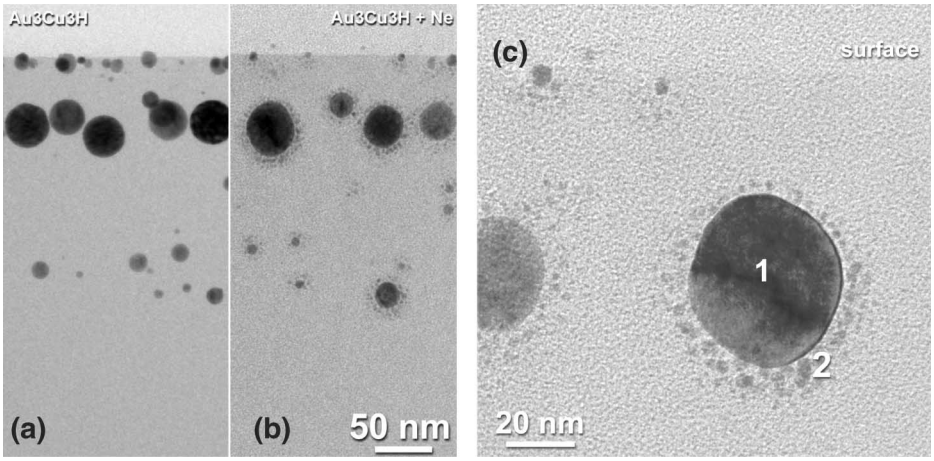

Fig. 35. – Bright-field TEM cross-sectional micrograph of the sample Au3Cu3H (annealing in $H_2(4\%)$-N_2 atmosphere at 900 °C for 1 h) before (a) and after irradiation at room temperature with 190 keV Ne ions, at a dose of 1×10^{17} ions/cm^2 (b). In (c) the satellite-like topology of the clusters is shown at higher magnification.

release part of their energy crossing the region in which the bimetallic nanoclusters are present (centered around a depth of 70 nm).

The effect is shown in fig. 35(b) in comparison with the unirradiated reference, fig. 35(a). The most evident result is the new topology of the clusters: around each original cluster a set of satellite clusters of about 1–2 nm are present with an average distance of about 3 nm from the cluster surface, similarly to what reported in a ion beam mixing experiment of Au islands irradiated by Au MeV-ions [136, 153, 154]. In those works, the NCs halo observed around the larger Au precipitates was explained in terms of the ballistic process, which dissolves NCs into the SiO_2 host by ion mixing, and of the large increase in the solute concentration in the matrix with a subsequent precipitation. SRIM simulations [5] indicate that in those experiments the nuclear components of the energy loss (S_n) is comparable to the electronic one (S_e), whereas in the present work for 190 keV Ne ions the ratio S_e/S_n is about 3. Two points are worth noting in the present experiment i) the asymmetry in the density of the satellites around the clusters: a closer inspection at fig. 35(c) shows that they are more dense and slightly larger in the region opposite to the surface (*i.e.* to the irradiating beam direction) with respect to the cluster; ii) the composition of the satellites: EDS compositional analysis with a focused electron beam of 2 nm FWHM of the FEG-TEM in the central part of the cluster (region 1 of fig. 35(c)) gives an Au/Cu atomic ratio (measured at AuL and CuK) of 1.3 $\pm$0.1, whereas the same ratio measured in region 2 (*i.e.* on the satellite clusters) results to be 3.2 ± 0.3, indicating a preferential extraction of Au from the original clusters. The asymmetry in the satellite cluster density supports the hypothesis of a relevant contribution of the S_n component of the energy loss in the creation of an elemental-selective vacancy formation in the NCs, which could be also responsible for the preferential Au out-coming from the original alloy. Coulter and Parkin [155] derived an integro-differential equation to calculate the number of displacements produced in a polyatomic target by Primary Knock-on Atom (PKA), on the basis of Lindhard *et al.* method [156]. The net displacement damage function presents a similar form to the modified Kinchin-Pease func-

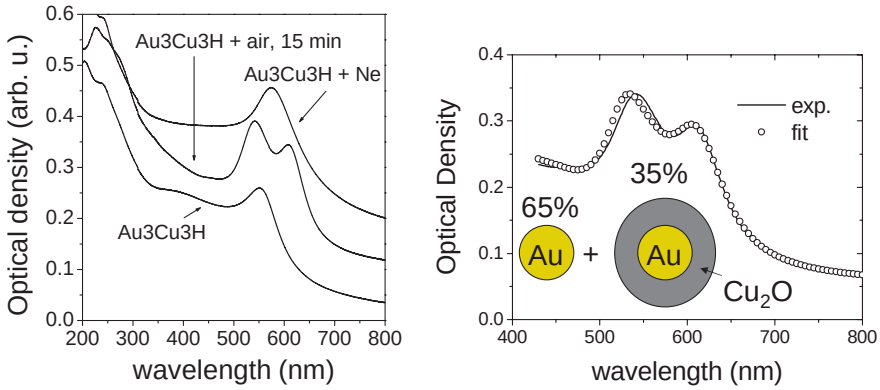

Fig. 36. – Left panel: optical density of the sample Au3Cu3H (annealing in $H_2(4\%)$-N_2 atmosphere at 900°C for 1 h) before and after a thermal annealing in air at 900°C for 15 min (Au3Cu3H + air, 15 min) or after irradiation at room temperature with 190 keV Ne ions, at a dose of 1×10^{17} ions/cm^2 (Au3Cu3 + Ne). The spectra were vertically shifted for clarity. Right panel: fit to the optical density of the sample Au3Cu3H after annealing in air at 900°C for 15 min.

tion [157] introducing a displacement threshold for every type of atoms. The calculated ratio of the displacement efficiencies is increasing with the ratio between the corresponding element mass. Replacement collision sequences may then influence the final state in a complex way. Moreover, preferential elemental ejection is correlated to different transport processes such as radiation enhanced diffusion, recoil implantation or cascade mixing, surface segregation or radiation-induced solute segregation. We observe that, on the basis of Neumann-Kopp's rule [152], in the bulk Au_xCu_{1-x} alloy for $x \sim 0.56$, as in the present case, the Au partial molar entalpy of formation ($\Delta H_{\mathrm{Au}} = -236 \pm 20$ cal/g-atom) is higher than the corresponding Cu one ($\Delta H_{\mathrm{Cu}} = -887 \pm 90$ cal/g-atom) [158], suggesting a possible preferential vacancy formation in the Au sub-lattice. This asymmetric behavior in the two sub-lattices can be also interpreted in terms of a deviation from the virtual crystal approximation recently demonstrated in AuCu alloys [159, 116]. Additional effects of preferential (Au) elemental segregation [160], which may be relevant in medium-large size clusters, can give further driving force to the de-alloying mechanism via Au extraction. The extracted gold atoms tend to precipitate as a consequence of the radiation enhanced diffusion and of the local overcoming of the solubility limit [68].

It is interesting to compare the optical absorption spectrum of the reference sample Au3Cu3H after the two de-alloying processes. This is shown in the left panel of fig. 36: the effect of the 15 min thermal annealing in oxidizing atmosphere is the splitting of the original SPR peak at 550 nm into two peaks, one at 530 nm and one at about 610 nm. According to the TEM analysis, we have simulated the spectrum assuming a partial core-shell geometry on the nanoclusters: indeed the Cu_2O nanostructure does not form a complete shell around the Au-rich cores. Therefore we have calculated the optical density of a mixture of pure Au and Au(core)-Cu_2O(shell) nanoclusters. The results of the fit is in good agreement with the experimental spectrum and it is shown in the right panel of fig. 36 with the computed relative fractions of the two kinds of clusters.

The effect of Ne-irradiation on the optical properties of AuCu samples is a red-shift of the surface plasma resonance (SPR) from 550 nm to 575 nm: this value would correspond

TABLE VI. – *Irradiation conditions used to investigate the effects of the nuclear component of the energy loss in radiation-assisted selective de-alloying in Au_xAg_{1-x} nanoclusters and nuclear fraction of energy loss (S_n) calculated using SRIM simulations.*

Ion	Energy (keV)	Fluence (ions/cm^2)	S_n (%)
He^+	25	3.2×10^{17}	10
Ne^+	100	5.2×10^{16}	43
Ar^+	190	2.5×10^{16}	50
Kr^{2+}	380	1.2×10^{16}	67

to SPR of pure Cu clusters. Therefore, as the actual cluster composition measured by EDS is roughly comparable to the original one, this is an indication that we cannot interpret this shift merely in terms of a compositional change and that we have to consider that the topological arrangement of the satellites clusters, about 2–3 nm from the original cluster surface, can induce a strong coupling, which cannot be accounted for by a simple Mie-type theory [40].

In conclusion, we presented two different experimental approaches for an elemental-selective de-alloying of bimetallic Au_xCu_{1-x} nanoclusters in dielectic matrix. The first de-alloying process (induced by thermal annealing in oxidizing atmosphere) follows a path similar to the corrosion process, in which the less noble element (Cu, in the present case) is extracted by its chemical interaction with the incoming oxygen. On the contrary, in the latter mechanism, vacancy formation sustained by ballistic process during Ne irradiation produces the Au preferential out-coming in a peculiar topological arrangement, in which small satellites nanoparticles surround the original alloy cluster. In both cases a crucial role is played by vacancy formation and diffusion, giving a unified interpretative framework.

6˙2.2. Au-Ag alloy clusters. A more quantitative investigation on the nuclear component effect of this elemental-selective de-alloying has been done by varying the irradiating ions, at constant energy and released power density, and the composition of the irradiated alloy NCs [161]. The results on irradiation with He, Ne or Kr ions of AuAg alloy nanoclusters in SiO_2 completely corroborate in a quantitative way the above described picture for de-alloying, *i.e.* that a similar preferential segregation of Au in the satellite clusters is found. This is a confirmation that the mechanism proposed is of general validity and independent of the particular system investigated. Moreover, a clear direct correlation between size of the satellite clusters and the nuclear component of the energy released by the incoming ions is found.

Fused silica (type II, Heraeus) slides were sequentially implanted with Au^+ and Ag^+ ions at room temperature at a current density of 2 μA/cm^2, ion energies of 190 keV for Au and 130 keV for Ag and doses of 3×10^{16} ions/cm^2 for both ions. Implanted slides were then heat treated in a conventional furnace in air at 800 °C for 1 h. The annealing conditions were chosen to produce large and well-separated clusters as in ref. [25]. This is the reference sample, in the following labeled as AuAg. The reference sample underwent two sets of ion-irradiations: in the first set, the AuAg sample was irradiated with He, Ne, Ar or Kr at different dose and energy (table VI shows the details of irradiation conditions) so as to deposit the same energy and power density on the sample; in the

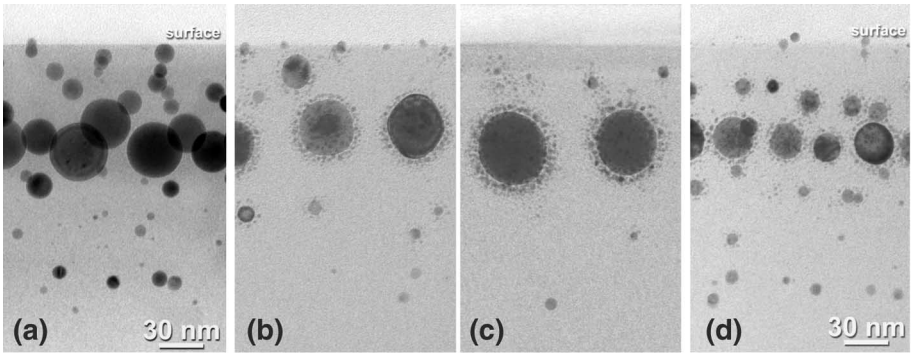

Fig. 37. – TEM cross-sectional images of the sample Au3Ag3A (annealing in air at 900 °C for 1h) before (a), after irradiation at room temperature with He ions (b), with Ne ions (c) and with Kr ions (d).

second set three AuAg samples were irradiated with Ar ions at the same energy (190 keV) and current density (0.84 μA/cm^2) at three different doses (1.0×10^{16} ions/cm^2, 2.5×10^{16} ions/cm^2 and 5.0×10^{16} ions/cm^2). The samples obtained after the second set of ion-irradiation are labeled as AuAgArxF where x are the implantation fluences of Ar ions in 1.0×10^{16} ions/cm^2 units.

In fig. 37a the bright-field TEM cross-sectional image of the reference AuAg sample is shown. The size distribution of the clusters has an average diameter $\langle D \rangle = 11.7$ nm and a standard deviation of the experimental bimodal distribution $\sigma = 6.4$ nm. The effect of irradiating the AuAg sample with Ne ions at 100 keV and with Ar at 190 keV is shown in fig. 37b and 37c, respectively. Ion irradiation promotes the formation of satellite clusters around each original cluster (similar images are obtained after irradiation with 25 keV He ions and with 380 keV Kr ions). Moreover, comparing fig. 37b and fig. 37c we note that the Ar-irradiated AuAg sample has a larger volumetric density of satellite clusters than the Ne-irradiated AuAg sample. Ion energy loss parameters and the number of vacancies created during collisional cascade by ion were calculated using SRIM simulation. In the last column of table VI we report the calculated fraction of nuclear component of energy loss. In fig. 38 the number of atoms ejected by each ion from the original clusters (from TEM analysis) is correlated to the number of vacancies created by irradiating ion calculated by SRIM simulations.

Increasing the nuclear fraction of the energy loss increases the formation of vacancies in the original cluster during the collisional cascade (as obtained by Monte Carlo simulations). We see from fig. 38 that the material emission from the Au_xAg_{1-x} clusters can be correlated to vacancies formation in the original cluster, so the NCs halo observed around each cluster could be explained in terms of ballistic process induced by irradiating ions. Indeed both satellite clusters average diameter and distance from the cluster surface have a linear increase with the nuclear component of the energy released by the irradiating ions.

EDS compositional analysis with a focused 2 nm electron beam of the FEG-TEM in the central part of mother cluster on the Ar-irradiated AuAg sample, gives an Au/Ag ratio (measured at AuL and AgL) of 1.4 ± 0.1, whereas the same ratio measured on the satellite clusters is 2.3 ± 0.8. Similar ratios have been found from EDS analysis on AuAg sample irradiated with He, Ne or Kr ions. EDS analysis reveals therefore a

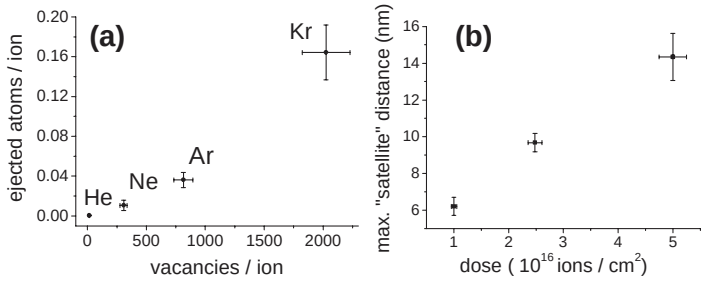

Fig. 38. – (a) Evolution of the number of ejected atoms per ion from alloy nanoclusters (obtained by TEM analysis) *vs.* vacancy formation per ion (calculated by SRIM simulations). (b) Linear increase of maximum satellite clusters distance from the original cluster surface with dose of irradiating-ion (Ar, 190keV).

preferential extraction of Au atoms from the original cluster and this selective de-alloying process is independent of the particular system investigated (we obtained similar results for Ne-irradiated Au_xCu_{1-x} cluster, as reported in the previous section). We explain this preferential Au emission from the original alloy could be explained in terms of an elemental-selective vacancy formation in the NCs, similarly to the Au-Cu case, as in the model of Coulter and Parkin [155]. Moreover, on the basis of Neumann-Kopp's rule, in the bulk Au_xAg_{1-x} alloy for a composition corresponding to $x \sim 0.6$, as in the present case, the modulus of Au partial molar enthalpy of formation ($|\Delta H_{\mathrm{Au}}| = 372 \pm 33$ cal/g-atom) is less than the Ag one ($|\Delta H_{\mathrm{Ag}}| = 675 \pm 61$ cal/g-atom) [158], and we suggest a possible preferential vacancy formation in the Au sub-lattices.

In fig. 37d the bright field TEM cross-sectional image of AuAgAr1 sample is reported in comparison with that of AuAgAr2.5 sample (fig. 37c). We note that the AuAgAr2.5 sample has a greater volumetric density of satellite clusters around each original cluster than the AuAgAr1 sample. Figure 38b shows a linear correlation between the maximum distance of satellite clusters from the cluster surface and the radiation dose. The maximum distance of satellite clusters from the cluster surface, determined by TEM, is a linear function of the radiation dose and this dependence could be explained in terms of radiation enhanced diffusion (RED) [155] promoted by an increased amount of structural defects in SiO_2 as a consequence of the increased electronic component of the energy deposited during irradiation in the sample. In fact, when amorphous SiO_2 is irradiated with energetic ions, various types of structural defects are created as a consequence of ion-solid interaction. Hosono *et al.* [162] have shown that Frenkel defects of oxygen, the dominant defects created in amorphous SiO_2, are correlated to the electronic component (S_e) of the energy loss. The TEM analysis reveals a reduction of satellite clusters volumetric density around each original cluster with an increase of the radiation dose. On the other hand, the satellite clusters averaged diameter initially increases as a function of radiation dose and then reaches a constant of $D \sim 1.8$ nm. This can be understood by assuming that the cluster growth follows an Ostwald ripening process and that prevails over a possible cluster density increase due to a heterogeneous nucleation on structural defects on SiO_2 [68, 163].

The effect of ion irradiation on the optical absorption of the systems is shown in fig. 39. A progressive red-shift of the resonance is found as the mass of the irradiating ions is increased, *i.e.* as the nuclear fraction of the energy loss is increased. This can be

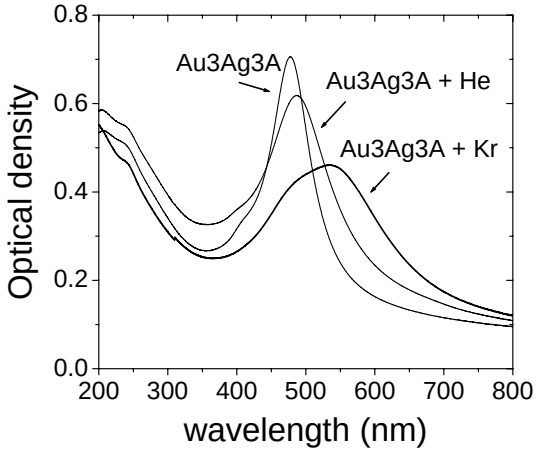

Fig. 39. – Optical density of the sample Au3Ag3A (annealing in air at 900 °C for 1h) before, after irradiation at room temperature with 25 keV He ions, at a dose of 3.2×10^{17} ions/cm^2 and with 380 keV Kr ions, at a dose of 1.2×10^{16} ions/cm^2.

understood as an increased interaction between the original clusters and their satellites, similarly to what happens for core-shell systems. Coupling this result with the experimental observation of the sign reversal in the third-order nonlinearity exhibited by these systems (see subsect. **5**˙3) due to the relative position between the laser frequency and the SPR absorption can be relevant for the formation of nonlinear nanocomposites with tunable optical properties.

7. – General conclusions

The advantages and the perspectives of the ion implantation technique in the formation of metal or metal alloys nanoclusters in dielectric matrix have been presented in detail. The most relevant technological parameters for ion implantation (dose, energy) and for subsequent treatments (thermal annealing, ion irradiation with low-mass ions) were investigated to control cluster composition, size and stability. Nanocluster growth mechanisms have been deeply investigated and correlated to theoretical approaches. The formation of metal alloys nanoclusters has been obtained through sequential ion implantation. The temporal sequence of implants is important in the formation of core-shell structures. Particularly intriguing is the modification induced by ion irradiation on the topology and composition of Au-Ag and Au-Cu nanoclusters: around each original cluster a halo of small satellites develops with a preferential out-coming of Au, indicating an elemental selective de-alloying. During thermal annealing the dealloying process is governed by the annealing atmosphere (oxidizing or reducing), as evidenced in Au-Ag, Pd-Cu, Au-Cu nanoclusters. This behaviour is correlated to a "corrosion" mechanism, due to the selective interaction of the annealing atmosphere with the alloy components. As far as the technological properties of the systems investigated are concerned, very interesting results have been obtained about the nonlinear optical properties with the Z-scan technique. High values of the third-order nonlinear refractive index, n_2, have been measured, evidencing the electron contribution to third-order susceptibility. An interesting change of n_2 algebric sign as a function of the nanocluster composition has been

evidenced. Metal nanoclusters doped glasses represent a new branch of optical materials and are potentially useful for many applications in digital optical processing, optoelectronics, integrated and nano-optics. Much experimental and theoretical effort is focused on the unique physical properties of these materials, which are quite different from those of the bulk matrix materials and depend on the cluster size, shape and packing density. In the huge volume of work in the field of materials science for nano-scale applications, nanocluster-doped glasses have become one of the most promising materials. Interesting perspectives are present for dielectric materials containing magnetic nanoclusters. Ion implantation technique presents, in this field, peculiar characteristic related to a control of the composition of nanostructured materials, cluster size and a technological approach, derived by the long activity in microelectronics.

* * *

We would like to gratefully acknowledge the work and the collaboration of the people at the Department of Physics of the University of Padova (V. Bello, C. de Julian Fernandez, G. De Marchi, C. Maurizio, C. Sada, C. Scian, E. Trave), Venezia (G. Battaglin, E. Cattaruzza, F. Gonella) and Trento (A. Miotello, A. Quaranta).

REFERENCES

[1] Mazzoldi P., Mattei G., Maurizio C., Cattaruzza E. and Gonella F., *Metal Alloy Nanoclusters by Ion Implantation in Silica, in Engineering Thin Films and Nanostructures with Ion Beams*, Chapt. 7, edited by Emile Knystautas (CRC Press) 2005, pp. 81-158.
[2] Mazzoldi P., Arnold G. W., Battaglin G., Gonella F. and Haglund R. Jr., *J. Nonlin. Opt. Phys. Mat.*, **5** (1996) 285.
[3] Gonella F. and Mazzoldi P., *Metal Nanocluster Composite Glasses, in Handbook of Nanostructured Materials and Nanotechnology*, edited by Nalwa H. S., Vol. **4** (Academic Press, S. Diego) 2000, pp. 81-158.
[4] Mazzoldi P. and Arnold G. W., *Ion Beam Modification of Insulators* (Elsevier Science Publisher B. V.) 1987.
[5] Ziegler J. F., Biersack J. P. and Littmark U. (Pergamon, New York) 1985.
[6] Möller W. and Eckstein W., *Nucl. Instrum. Methods in Phys. Res. B*, **2** (1984) 814.
[7] Konoplev V., *Radiat. Eff. Lett.*, **87** (1986) 207.
[8] Stepanov A., Zhikharev V., Hole D., Townsend P. and Khaibullin I., *Nucl. Instrum. Methods B*, **166-167** (2000) 26.
[9] Valentin E., Bernas H., Ricolleau C. and Creuzet F., *Phys. Rev. Lett.*, **86** (2001) 99.
[10] Perez A., Marest G., Sawicka B., Sawicki J. and Tyliszczac T., *Phys. Rev. B*, **28** (1983) 1227.
[11] Perez A., *Nucl. Instrum. Methods B*, **1** (1984) 621.
[12] Futagami T., Aoki Y., Yoda O. and Nagai S., *Nucl. Instrum. Methods B*, **88** (1994) 261.
[13] Hosono H., *Jpn. J. Appl. Phys.*, **32** (1993) 3892.
[14] Hosono H. and Matsunami N., *Phys. Rev. B*, **48** (1993) 13469.
[15] Hosono H. and Imagawa H., *Nucl. Instrum. Methods in Phys. Res. B*, **91** (1994) 510.
[16] Cattaruzza E., *Nucl. Instrum. Methods B*, **169** (2000) 141.
[17] Kelly R., *Mater. Sci. Eng. A*, **115** (1989) 11.
[18] Hosono H., *Phys. Rev. Lett.*, **74** (1995) 110.
[19] Battaglin G., *Nucl. Instrum. Methods B*, **116** (1996) 102.

[20] Gonella F., *Nucl. Instrum. Methods B*, **166-167** (2000) 831.
[21] Magruder III R. H., Wittig J. E. and Zuhr R. A., *J. Non-Cryst. Solids*, **163** (1993) 162.
[22] Magruder III R. H., Osborne Jr. D. H. and Zuhr R. A., *J. Non-Cryst. Solids*, **176** (1994) 299.
[23] Cattaruzza E., Battaglin G., Polloni R., Cesca T., Gonella F., Mattei G., Maurizio C., Mazzoldi P., D'Acapito F., Zontone F. and Bertoncello R., *Nucl. Instrum. Methods B*, **148** (1999) 1007.
[24] Gonella F., Mattei G., Mazzoldi P., Sada C., Battaglin G. and Cattaruzza E., *Appl. Phys. Lett.*, **75** (1999) 55.
[25] Mattei G., *Nucl. Instrum. Methods B*, **191** (2002) 323.
[26] Martucci A., de Nuntis M., Ribaudo A., Guglielmi M., Padovani S., Enrichi F., Mattei G., Mazzoldi P., Sada C., Trave E., Battaglin G., Gonella F., Borsella E., Falconieri M., Patrini M. and Fick J., *Appl. Phys. A*, **80** (2005) 557.
[27] Respaud M., Broto J. M., Rakoto H., Fert A., Thomas L., Barbara B., Verelst M., Snoeck E., Lecante P., Mosset A., Osuna J., Ely T. O., Amiens C. and Chaudret B., *Phys. Rev. B*, **57** (1998) 2925.
[28] Tihay F., Pourroy G. M., Roger A. C. and Kienneman A., *Appl. Catalysis A*, **206** (2000) 24.
[29] Faraday M., *Philos. Trans. R. Soc.*, **147** (1857) 145.
[30] Maxwell-Garnett J. C., *Philos. Trans. R. Soc. A*, **203** (1904) 385.
[31] Maxwell-Garnett J. C., *Philos. Trans. R. Soc. A*, **205** (1904) 237.
[32] Mie G., *Ann. Phys. (Leipzig)*, **25** (1908) 377.
[33] Flytzanis C., Hache F., Klein M., Ricard D. and Roussignol P., *Progr. Opt.*, **29** (1991) 321.
[34] Mazzoldi P. and Righini G., *Glasses for optoelectronic devices*, in *Insulating Materials for Optoelectronics*, edited by Agulló-López F. (World Scientific, Singapore) 1995, pp. 367-392.
[35] Haglund Jr. R. F., *Quantum-dot composites for nonlinear optical applications*, in *Handbook of Optical Properties II: Optics of Small Particles, Interfaces, and Surfaces*, edited by Hummel R. E. and Wissmann P., Vol. **2**, p. 191 (CRC Press, New York) 1997.
[36] Perenboom J. and Wyder P., *Phys. Rep.*, **78** (1981) 173.
[37] Halperin W., *Rev. Mod. Phys.*, **58** (1986) 533.
[38] Hache F., Ricard D. and Girard C., *Phys. Rev. B*, **38** (1988) 7990.
[39] Haus J., Kalyaniwalla N., Inguva R., Bloemer M. and Bowden C., *J. Opt. Soc. Am. B*, **6** (1988) 797.
[40] Kreibig U. and Vollmer M., *Optical Properties of Metal Clusters* (Springer-Verlag, Berlin Heidelberg) 1995.
[41] Doremus R. H., *Glass Science* (John Wiley, New York, USA) 1973.
[42] Yang L., Osborne D. J., R. F. Haglund Jr., Magruder III R. H., White C. W., Zuhr R. A. and Hosono H., *Appl. Phys. A*, **62** (1996) 403.
[43] Ironside C. N., *Contemp. Phys.*, **34** (1993) 1.
[44] Haglund Jr. R. F., Yang L., Magruder III R. H., White C. W., Zuhr R. A., Yang L., Dorsinville R. and Alfano R. R., *Nucl. Instrum. Methods B*, **91** (1994) 493.
[45] Skelland N. and Townsend P., *Nucl. Instrum. Methods B*, **93** (1994) 433.
[46] Stepanov A. L. and Hole D. E., *Recent Res. Devel. Appl. Phys.*, **5** (2002) 1.
[47] Meldrum A., Haglund Jr. R. F., Boatner L. A. and White C. W., *Adv. Mater.*, **13** (2001) 1431.
[48] Mattei G., De Marchi G., Mazzoldi P., Sada C., Bello V. and Battaglin G., *Phys. Rev. Lett.*, **90** (2003) 085502/1.
[49] Battaglin G., Cattaruzza E., Gonella F., Mattei G., Mazzoldi P., Sada C. and Zhang X., *Nucl. Instrum. Methods B*, **166-167** (2000) 857.
[50] Magruder III R. H. and Zuhr R. A., *J. Appl. Phys.*, **77** (1995) 3546.

[51] Magruder III R. H., Anderson T. S., Zuhr R. A. and Thomas D. K., *Nucl. Instrum. Methods B*, **108** (1996) 305.
[52] Anderson T. S., Magruder III R. H., D. L. Kinser, Zuhr R. A. and Thomas D. K., *Nucl. Instrum. Methods. B*, **124** (1997) 40.
[53] D'Acapito F., Mobilio S., Gonella F., Maurizio C., Mazzoldi P., Battaglin G., Cattaruzza E. and Zontone F., *Euro. Phys. J. D*, **10** (2000) 123.
[54] Gonella F., Cattaruzza E., Battaglin G., D'Acapito F., Sada C., Mazzoldi P., Maurizio C., Mattei G., Martorana A., Longo A. and Zontone F., *J. Non-Cryst. Solids*, **280** (2001) 241.
[55] Falconieri M., Salvetti G., Cattaruzza E., Gonella F., Mattei G., Mazzoldi P., Piovesan M., Battaglin G. and Polloni R., *Appl. Phys. Lett.*, **73** (1998) 288.
[56] Cattaruzza E., Battaglin G., Gonella F., Polloni R., Mattei G., Maurizio C., Mazzoldi P., Sada C., Tosello C., Montagna M. and Ferrari M., *Philos. Mag. B*, **82** (2002) 735.
[57] de Julián Fernández C., Sangregorio C., Mattei G., De G., Saber A., Russo S. L., Battaglin G., Catalano M., Cattaruzza E., Gonella F., Gatteschi D. and Mazzoldi P., *Mater. Sci. Eng. C*, **15** (2001) 59.
[58] de Julián Fernández C., Sangregorio C., Mattei G., Battaglin G., Cattaruzza E., Gonella F., Russo S. L., D'Orazio F., Lucari F., De G., Gatteschi D. and Mazzoldi P., *J. Mag. Mag. Mater.*, **226-230** (2001) 1912.
[59] White C., Withrow S., Budai J., Boatner L., Sorge K., Thompson J., Beaty K. and Meldrum A., *Nucl. Instrum. Methods B*, **191** (2002) 437.
[60] Cattaruzza E., D'Acapito F., de Julián Fernandez C., Lorenzi A. D., Gonella F., Mattei G., Maurizio C., Mazzoldi P., Padovani S., Scremin B. and Zontone F., *Nucl. Instrum. Methods B*, **191** (2002) 406.
[61] Battaglin G., Cattaruzza E., De Marchi G., Gonella F., Mattei G., Maurizio C., Mazzoldi P., Parolin A., Sada C. and Calliari I., *Nucl. Instrum. Methods B*, **191** (2002) 392.
[62] Borsella E., Dal Toé S., Mattei G., Maurizio C., Mazzoldi P., Saber A., Battaglin G., Cattaruzza E., Gonella F., Quaranta A. and D'Acapito F., *Mater. Sci. Eng. B*, **82** (2001) 148.
[63] Borsella E., Garcia M., Mattei G., Maurizio C., Mazzoldi P., Cattaruzza E., Gonella F., Battaglin G., Quaranta A. and D'Acapito F., *J. Appl. Phys.*, **90** (2001) 4467.
[64] Borsella E., de Julián Fernández C., M. Garcìa, Mattei G., Maurizio C., Mazzoldi P., Padovani S., Sada C., Battaglin G., Cattaruzza E., Gonella F., Quaranta A., D'Acapito F., Tagliente M. and Tapfer L., *Nucl. Instrum. Methods B*, **191** (2002) 447.
[65] Heinig K. H., Schmidt B., Markwitz A., R. Grötzschel, Strobel M. and Oswald S., *Nucl. Instrum. Methods B*, **148** (1999) 969.
[66] Ila D., Williams E. K., Sarkisov S., Smith C. C., Poker D. B. and Hensley D. K., *Nucl. Instrum. Methods B*, **141** (1998) 289.
[67] Collins D. R., Schroder D. K. and Sah C. T., *Appl. Phys. Lett.*, **8** (1966) 323.
[68] Miotello A., De Marchi G., Mattei G., Mazzoldi P. and Sada C., *Phys. Rev. B*, **63** (2001) 075409.
[69] Arnold G. W. and Borders J. A., *J. Appl. Phys.*, **48** (1977) 1488.
[70] Lifshitz I. M. and Slezof V. V., *Zh. Eksp. Teor. Fiz.*, **35** (1958) 479.
[71] Yukselici H., Persans P. D. and Hayes T. M., *Phys. Rev. B*, **52** (1995) 11763.
[72] Gurevich S. A., Ekimov A. I., Kudrayavtsev I. A., Lyublinskaya O. G., Osinnskii A. V., Usikov A. S. and Faleev N. N., *Semicond.*, **28** (1994) 486.
[73] Wagner C., *Z. Elektrochem.*, **65** (1961) 581.
[74] Johnson P. B. and Christy R. W., *Phys. Rev. B*, **6** (1972) 4370.
[75] Battaglin G., Della Mea G., De Marchi G., Mazzoldi P. and Miotello A., *Nucl. Instrum. Methods B*, **7/8** (1985) 517.

[76] Arnold G., Battaglin G., Della Mea G., De Marchi G., Mazzoldi P. and Miotello A., *Nucl. Instrum. Methods B*, **32** (1988) 315.
[77] Lamkin M. A., Riley F. L. and Fordham R. J., *J. Eur. Ceram. Soc.*, **10** (1992) 347.
[78] Norton F., *Nature*, **191** (1961) 701.
[79] Biersack J. P. and Haggmark L. G., *Nucl. Instrum. Methods B*, **174** (1980) 257.
[80] Devine R. A. B., *Nucl. Instrum. Methods B*, **91** (1994) 378.
[81] Dienes G. J. and Damask A. C., *J. Appl. Phys.*, **29** (1958) 1713.
[82] Griscom D. L., *Nucl. Instrum. Methods B*, **1** (1984) 481.
[83] Aaron H. B., Fainstein D. and Kotler G. R., *J. Appl. Phys.*, **41** (1970) 4404.
[84] Buffat P. and Borel J.-P., *Phys. Rev. A*, **13** (1976) 2287.
[85] Heilmann A., *Polymer Films with Embedded Metal Nanoparticles* (Springer Ed., Berlin) 2003.
[86] Cioffi N., Farella L., Torsi I., Valentini A. and Tafuri A., *Sensors and Actuators B*, **84** (2002) 49.
[87] Stepanov A. L., *Metal-Polymer Nanocomposites*, edited by Nicolais L. and Carotenuto G. (Willey J. Sons, Chichester) 2004, pp. 241-263.
[88] Stepanov A. L., *Techn. Phys.*, **49** (2004) 143.
[89] Rük D. M., Schulz J. and Deusch N., *Nucl. Instrum. Methods B*, **131** (1997) 149.
[90] Lee E. A., *Nucl. Instrum. Methods B*, **151** (1999) 29.
[91] Umeda N., Bandourko V. V., Vasilets V. N. and Kishimoto N., *Nucl. Instrum. Methods B*, **206** (2003) 657.
[92] Hegazy E.-S. A., Sasuga T., Nishii M. and Seguchi T., *Polymer*, **33** (1992) 2094.
[93] Kobayashi T., Iwata T., Doi Y. and Iwaki M., *Nucl. Instrum. Methods B*, **175-177** (2001) 584.
[94] Maggioni G., Carturan S., Rigato V. and Della Mea G., *Surf. Coat. Technol.*, **142-144** (2001) 156.
[95] Kobayashi T., Nakao A. and Iwaki M., *Surf. Coat. Technol.*, **158-159** (2002) 108.
[96] Popok V. N., Khaibullin R. I., Toth A., Beshliu V., Hnatowicz V. and Mackova A., *Surf. Sci.*, **532-535** (2003) 1034.
[97] Guenther M., Gerlach G., Suchaneck G., Sahre K., Eichhorn K. J., Wolf B., Deineka A. and Jastrabik L., *Surf. Coat. Technol*, **158-159** (2002) 108.
[98] Hernández J., Lucía M., Mártil I., González-Díaz G., Santamaria J. and Sánchez-Quesada F., *Appl. Opt.*, **31** (1992) 1606.
[99] de Julián Fernández C., Manera M. G., Spadavecchia J., Maggioni G., Quaranta A., Mattei G., Bazzan M., Cattaruzza E., Bonafini M., Negro E., Vomiero A., Carturan S., Scian C., Mea G. D., Rella R., Vasanelli L. and Mazzoldi P., *Sensors and Actuators B*, **111** (2005) 225.
[100] Yasuda H. and Mori H., *Z. Phys. D*, **31** (1994) 131.
[101] Battaglin G., Catalano M., Cattaruzza E., D'Acapito F., De Julián Fernández C., De Marchi G., Gonella F., Mattei G., Maurizio C., Mazzoldi P., Miotello A. and Sada C., *Nucl. Instrum. Methods B*, **178** (2001) 176.
[102] de Julián Fernández C., Mattei G., Battaglin G., Maurizio C., Mazzoldi P. and Scian C., *Nucl. Instrum. Methods B*, in press.
[103] de Julián Fernández C., Tagliente M., Mattei G., Sada C., Bello V., Maurizio C., Battaglin G., Sangregorio C., Gatteschi D., Tapfer L. and Mazzoldi P., *Nucl. Instrum. Methods B*, **216** (2004) 245.
[104] Mattei G., Battaglin G., Bello V., Cattaruzza E., Fernández C. D. J., De Marchi G., Maurizio C., Mazzoldi P., Parolin M. and Sada C., *Nucl. Instrum. Methods B*, **218** (2004) 433.
[105] de Julián Fernández C., Mattei G., Sangregorio C., Tagliente M., Bello V., Battaglin G., Sada C., Tapfer L., Gatteschi D. and Mazzoldi P., *J. Non-Cryst. Solids*, **345-346** (2004) 681.
[106] Mattei G., Maurizio C., Mazzoldi P., D'Acapito F., Battaglin G., Cattaruzza E., de Julián Fernández C. and Sada C., *Phys. Rev. B*, **71** (2005) 195418.

[107] Cattaruzza E., D'Acapito F., Gonella F., Longo A., Martorana A., Mattei G., Maurizio C. and Thiaudiere D., *J. Appl. Cryst.*, **33** (2000) 740.
[108] de Julián Fernández C., Sangregorio C., Mattei G., Maurizio C., Battaglin G., Gonella F., Lascialfari A., Lo Russo S., Gatteschi D., Mazzoldi P., González J. and D'Acapito F., *Nucl. Instrum. Methods B*, **175-177** (2001) 479.
[109] Bertoncello R., Gross S., Trivillin F., Caccavale F., Cattaruzza E., Mazzoldi P., Mattei G., Battaglin G. and Daolio S., *J. Mater. Res.*, **14** (1999) 2449.
[110] Okamoto H., Chakrabarti D. J., Laughlin D. E. and Massalski T. B., *Phase Diagrams of Binary Gold Alloys.* Monograph Series on Alloy Phase Diagrams (ASM International T.M. Metals Park, Ohio 44073) 1987.
[111] Battaglin G., Cattaruzza E., De Julian Fernandez C., De Marchi G., Gonella F., Mattei G., Maurizio C., Mazzoldi P., Miotello A., Sada C. and D'Acapito F., *Nucl. Instrum. Methods B*, **175-177** (2001) 410.
[112] Yasuda H., Mitsuishi K. and Mori H., *Phys. Rev. B*, **64** (2001) 094101.
[113] Mazzoldi P., Tramontin L., Boscolo-Boscoletto A., Battaglin G. and Arnold G. W., *Nucl. Instrum. Methods B*, **80/81** (1993) 1192.
[114] Caccavale F., De Marchi G., Gonella F., Mazzoldi P., Meneghini C., Quaranta A., Arnold G., Battaglin G. and Mattei G., *Nucl. Instrum. Methods B*, **96** (1995) 382.
[115] Maurizio C., Gonella F., Cattaruzza E., Mazzoldi P. and D'Acapito F., *Nucl. Instrum. Methods B*, **200** (2003) 126.
[116] Maurizio C., Mattei G., Mazzoldi P., Padovani S., Cattaruzza E., Gonella F., D'Acapito F. and Zontone F., *Nucl. Instrum. Methods B*, **200** (2003) 178.
[117] Massalski B., *Binary Alloy Phase Diagrams* (American Society for Metals, Metals Park, Ohio 44073) 1987.
[118] De G., Gusso M., Tapfer L., Catalano M., Gonella F., Mattei G., Mazzoldi P. and Battaglin G., *J. Appl. Phys.*, **80** (1996) 6734.
[119] Uchida K., Kaneko S., Omi S., Hata C., Tanji H., Asahara Y., Ikushima A., Tokizaki T. and Nakamura A., *J. Opt. Soc. Am. B*, **11** (1994) 1236.
[120] Sheik-Bahae M., Said A. A., Wei T. H., Hagen D. and Van Stryland E. W., *IEEE J. Quantum Electron.*, **26** (1990) 760.
[121] Wang J., Sheik-Bahae M., Said A. A., Hagen D. J. and Van Stryland E. W., *J. Opt. Soc. Am. B*, **11** (1994) 1009.
[122] Van Stryland E. W. and Sheik-Bahae M., *Materials Characterization and Optical Probe Techniques*, edited by R. A. Lessard and Franke H., Vol. CR96 (SPIE, Bellingham 1997) 1997.
[123] Cattaruzza E., Battaglin G., Gonella F., Mattei G., Mazzoldi P., Polloni R. and Scremin B., *Appl. Surf. Sci.*, **247** (2005) 390.
[124] Pinçon-Roetzinger N., Prot D., Palpant B., Charron E. and Debrus S., *Mater. Sci. Eng. C*, **19** (2002) 51.
[125] Prez-Arantegui J., Molera J., Larrea A., Pradell T., Vendrell-Saz M., Borgia I., Brunetti B., Cariati F., Fermo P., Mellini M., Sgamellotti A. and Viti C., *J. Am. Ceram. Soc.*, **84** (2001) 442.
[126] Borgia L., Brunetti B., Sgamellotti A., Mariani I., Cariati F., Fermo P., Mellini M. and Viti C., *Appl. Surf. Sci.*, **185** (2002) 206.
[127] Padovani S., Sada C., Mazzoldi P., Brunetti B., Borgia L., Sgamellotti A., Giulivi A., D'Acapito F. and Battaglin G., *J. Appl. Phys.*, **93** (2003) 10058.
[128] Padovani S., Borgia L., Brunetti B., Sada C., Sgamellotti A., Giulivi A., D'Acapito F., Mazzoldi P., Sada C. and Battaglin G., *Appl. Phys. A*, **79** (2004) 229.
[129] De G., Mattei G., Mazzoldi P., Sada C. and Battaglin G., *Chem. Mater.*, **75** (1999) 55.
[130] Mattei G., de Julin Fernndez C., Mazzoldi P., Sada C., De G., Battaglin G., Sangregorio C. and Gatteschi D., *Chem. Mater.*, **14** (2002) 3440.
[131] Nishizawa T. and Ishida K., *Bull. Phase Diagrams*, **5** (1984) 1.

[132] Childress J. R. and Chien C. L., *Phys. Rev. B*, **43** (1991) 8089.
[133] Noetzel J., Handstein A., Mucklich A., Prockert F., Reuther H., Thomas J., Wieser E. and Moller W., *J. Mag. Mag. Mater.*, **205** (1999) 183.
[134] Zontone F., D'Acapito F. and Gonella F., *Nucl. Instrum. Methods B*, **147** (1999) 421.
[135] Garrido F., Dran J.-C., Thorné L., Meneghini C., Gonella F. and Quaranta A., *Nucl. Instrum. Methods B*, **115** (1996) 561.
[136] Pivin J. C. and Rizza G., *Thin Solid Films*, **366** (2000) 284.
[137] De Marchi G., Gonella F., Mazzoldi P., Battaglin G., Knystautas E. J. and Meneghini C., *J. Non-Cryst. Solids*, **196** (1996) 79.
[138] Gonella F., Knystautas E., Mattei G., Mazzoldi P., Meneghini C., Cattaruzza E., Garrido F. and Osborne D. Jr., *Nucl. Instrum. Methods B*, **127** (1997) 562.
[139] Mazzoldi P., Padovani S., Enrichi F., Mattei G., Sada C., Trave E., Guglielmi M., Martucci A., Battaglin G., Cattaruzza E., Gonella F. and Maurizio C., *Proc. SPIE*, **5451** (2004) 311.
[140] Strohhofer C. and Polman A., *J. Appl. Phys.*, **90** (2001) 4314.
[141] Kik P., Brongersma M. and Polman A., *Appl. Phys. Lett.*, **76** (2000) 2325.
[142] Franzò G., Iacona F., Vinciguerra V. and Priolo F., *Mater. Sci. Eng. B*, **69-70** (2000) 335.
[143] Borsella E., Gonella F., Mazzoldi P., Quaranta A., Battaglin G. and Polloni R., *Chem. Phys. Lett.*, **284** (1998) 429.
[144] Strohhofer C. and Polman A., *Appl. Phys. Lett.*, **81** (2002) 1414.
[145] Managaki M. F. N., Fujii M., Yanagi H. and Hayashi S., *J. Appl. Phys.*, **98** (2005) 024316.
[146] Skelland N. and Townsend P., *J. Non-Cryst. Solids*, **188** (1995) 243.
[147] White C., Budai J., Zhu J., Withrow S., Hembree D., Henderson D., Ueda A., Tung Y. and Mu R., *Mater. Res. Soc. Symp. Proc.*, **396** (1996) 377.
[148] Meldrum A., Boatner L. and White C., *Nucl. Instrum. Methods B*, **178** (2001) 7.
[149] Erlebacher J., Aziz J. M., Karma A., Dimitrov N. and Sieradzki K., *Nature*, **410** (2001) 450.
[150] Cahn R. W., *Nature*, **389** (1997) 121.
[151] Arnold G. W., Battaglin G., Boscolo-Boscoletto A., Caccavale F., De Marchi G. and Mazzoldi P., *Mater. Res. Soc. Symp. Proc.*, **235** (1992) 407.
[152] Smithells C. and Brandes E. (Editors), *Metals Reference Book* (Butterworths, London) 1976, 5th ed.
[153] Pivin J. C., *Mater. Sci. Eng. A*, **293** (2000) 30.
[154] Rizza G., Strobel M., Heining K. H. and Bernas H., *Nucl. Instrum. Methods B*, **178** (2001) 78.
[155] Nastasi M., Mayer J. W. and Hirvonen J. K. (Editors), *Ion-solid Interactions: Fundamentals and Applications* (Cambridge University Press) 1996.
[156] Lindhard J., Nielsen V., Scharff M. and Thomsen P., *(Notes on Atomic Collisions III) Mat. Fys. Medd. Dan Vid. Selsk.*, **33** (1963).
[157] Kinchin G. and Pease R., *Rep. Prog. Phys.*, **18** (1955) 1.
[158] Hultgren R., Orr R. L., Anderson P. and Kelley K. K., *Selected Values of Thermodynamic Properties of Metals and Alloys* (John Wiley and Sons, Inc.) 1963.
[159] Frenkel A. I., Machavariani V. S., Rubshtein A., Rosenberg Y., Voronel A. and Stern E. A., *Phys. Rev. B*, **62** (2000) 9364.
[160] Foiles S. M., Baskes M. I. and Daw M. S., *Phys. Rev. B*, **33** (1986) 7983.
[161] Bello V., Marchi G. D., Maurizio C., Mattei G., Mazzoldi P., Parolin M. and Sada C., *J. Non-Cryst. Solids*, **345-346** (2004) 685.
[162] Hosono H. and Matsunami N., *Nucl. Instrum. Methods B*, **141** (1998) 566.
[163] De Marchi G., Mattei G., Mazzoldi P., Sada C. and Miotello A., *J. Appl. Phys.*, **92** (2002) 4249.